R.F. Vorderegger

Optimization of gate design in the Afsluitdijk based on dynamic wave impact

Application of fluid-structure interaction models coupled with FEM

TUDelft

Figure 1. (Title page) Storm at the Stevinsluizen at Den Oever with water level at NAP +2.50 m (Thijsse, 1972).

Optimization of gate design in the Afsluitdijk based on dynamic wave impact

Application of fluid-structure interaction models coupled with FEM

By

R.F. Vorderegger

in partial fulfilment of the requirements for the degree of

Master of Science
in Hydraulic and Structural Engineering

at the Delft University of Technology
1/4/2019

TU DELFT

Prof. dr. ir. Bas Jonkman

Dr. ir. Bas Hofland

Ir. Orson Tieleman

Dr. ir. Apostolos Tsouvalas

WITTEVEEN+BOS

Ir. Huig de Waardt

Ir. Leon de Jongste

An electronic version of this thesis is available at http://repository.tudelft.nl/.

III

Preface

This report contains the research which is a partial fulfillment for the master's degree at the technical university of Delft. The incentive for the research is the start of the final design of the new Afsluitdijk by Levvel. Levvel is a consortium, where Witteveen+Bos is one of the partners. Witteveen+Bos is therefore also a partner for this thesis and helps with knowledge, data and guidance. I was able to work with colleagues at Witteveen+Bos as well as Levvel.

I would like to express my gratitude to all of those who helped and supported me in finalizing my graduation thesis.

First, I would like to thank ir. Huig de Waardt and ir. Leon de Jongste, my supervisors at Witteveen+Bos, for the time and energy they dedicated to my work. Their experience and genuine interest in the topic proved to be a source of inspiration and helped me find my way through the vast amount of information.

My appreciation goes out to my committee members from the university. Prof. dr. ir. Bas Jonkman, dr. ir. Bas Hofland, dr. ir Apostolos Tsouvalas and especially ir. Orson Tieleman, who guided me with their knowledge in varying fields. Their interest, enthusiasm and critical comments on my work contributed to the process in a positive way. I am very lucky to have enjoyed their expertise first hand.

Furthermore, I would like to acknowledge the positive atmosphere by the colleagues at the ground floor or 'basement' of the Witteveen+Bos office in Rotterdam, who helped me mentally in the process.

Special thanks to my family for their support and giving me the possibility to achieve my goals. Finally, but most important I thank Femke who supported me and is by my side from the first day.

Ruben Franjo Vorderegger,
Delft, February 2019

Abstract

The Afsluitdijk will undergo major redevelopment. After more than 80 years, the structure is ready for an upgrade. One of the differences which face the engineers of today compared to the original designers is climate change as well as the strict flood safety standards of the 21st century. Climate change is the lead cause of the sea level rise, which results in several issues at the Afsluitdijk. First, higher water levels result in larger waves causing more damage and secondly the discharge complexes will have difficulty in the natural discharge of the IJsselmeer. These discharge complexes consist of several locks side by side with each two gates; A northern and a southern gate. When the water level is too high in the IJsselmeer the gates will open during low tide and the water naturally drains into the Waddenzee. However, with sea level rise the water level difference is less and the time gap is also shortened creating a shortage in drained volume. The discharge complexes at Den Oever and Kornwerderzand are therefore redesigned with extra locks and pumping stations. The scope of this thesis concerns the new designs of the northern gates at Den Oever in the original discharge sluices. The concrete structure of the sluice will not be altered and is not part of the scope.

The flood safety has become a lot more complex in the last 80 years. According to the safety standard, the Afsluitdijk should be able to withstand a storm with a return period of 10.000 years, which is the highest in the country except for a dike segment close to a nuclear power plant. The result is that the gates have to withstand waves of. However, it was found by Hofland (2015) that these largest waves with the highest water levels were not governing. Waves with water levels lower than an overhanging structure were much more violent. This overhanging structure is now redundant, and it is decided to be removed for the new gates. However, it is still interesting how these impulsive forces can be calculated and predicted.

In order to find an alternative to model tests when encountering such a problem with an overhanging structure, a numerical method has been developed in this thesis. The method is based on the notion from Wood and Peregrine (1996), which directly calculates pressure impulse field. Their method is analytical and with the numerical alternative given in this thesis it has been made easier to adapt the boundaries and include gaps in the structure. The method is compared to the results of the model test executed by Hofland (2015).

A problem arises when these impulsive wave forces impact a relatively thin plated structure such as the gate. The dynamic response of the gate can cause an amplification in the expected displacement and stress. The surrounding fluid creates an extra complexity to the problem. The current engineering practice to analyze the dynamic response in such a situation is based on a simplified quasi-static method by Kolkman (2007). This simplified method is based on a Dynamic Amplification Factor (DAF) of a single degree of freedom system incorporated with an extra hydrodynamic mass.

A semi-analytical method derived by Tieleman (2015), that includes fluid-structure interaction has more potential to find a more realistic solution than the current engineering practice. The semi-analytical method still depends on a homogeneous isotropic thin-plate, but with the coupling of a finite element model (SCIA) the complexity of the design is theoretically limitless. This coupling is developed and numerically compared with the gate at the discharge sluice complex at Den Oever in this thesis.

The semi-analytical method allows for a complete dynamic calculation in a relatively short time. This gives the opportunity to perform multiple calculations back-to-back. This has been exploited in this thesis by the development of a parametric model. This parametric model is based on the gate design in the Afsluitdijk and can find the most optimal designs regarding thickness and placement of the several elements in the structure by utilizing an optimization scheme. The optimization is based on a predefined post-analysis, which in this case concerns equivalent stress and stability. However,

the possibilities are endless with possible addition many more failure mechanisms like fatigue. The model itself can be applied in a preliminary design phase where it gives the engineer more options while still incorporating the dynamic effect. It also helps to locate the more governing parameters, which is often difficult in a dynamic problem.

Table of Contents

1 Introduction

In this chapter information about the Afsluitdijk project (1.1) is given. This project is used as an exemplary case of the problem researched in this document. The problem definition (1.2) can be found further in this chapter together with the methodology (1.4) used to answer the research questions found in section 1.3.

1.1 The New Afsluitdijk Project

The Afsluitdijk, shown in Figure 2, needs a large-scale refurbishment. The structure is more than 80 years old and does not comply with the current safety standards anymore. Appendix A contains more in-depth knowledge of the history of the structure and reasoning of the redevelopment for the future.

Figure 2. Overview of the Afsluitdijk with important locations highlighted (GOOGLE MAPS, 2018).

The Afsluitdijk has four major functions: flood safety, discharging water, road traffic and ship traffic. Both the flood safety and discharge capacity will be increased in the redevelopment of this 32.5 km long structure. The current safety standard requires the structure to withstand storm conditions once in 10.000 years. The reason for such a high level of safety follows from Figure 3. The area shown in red is vital part of the country and is mainly protected by the Afsluitdijk from storms originating in the North Sea. Figure 3 shows that the land behind the structure is relatively low compared to the level of the sea, making it very vulnerable for flooding.
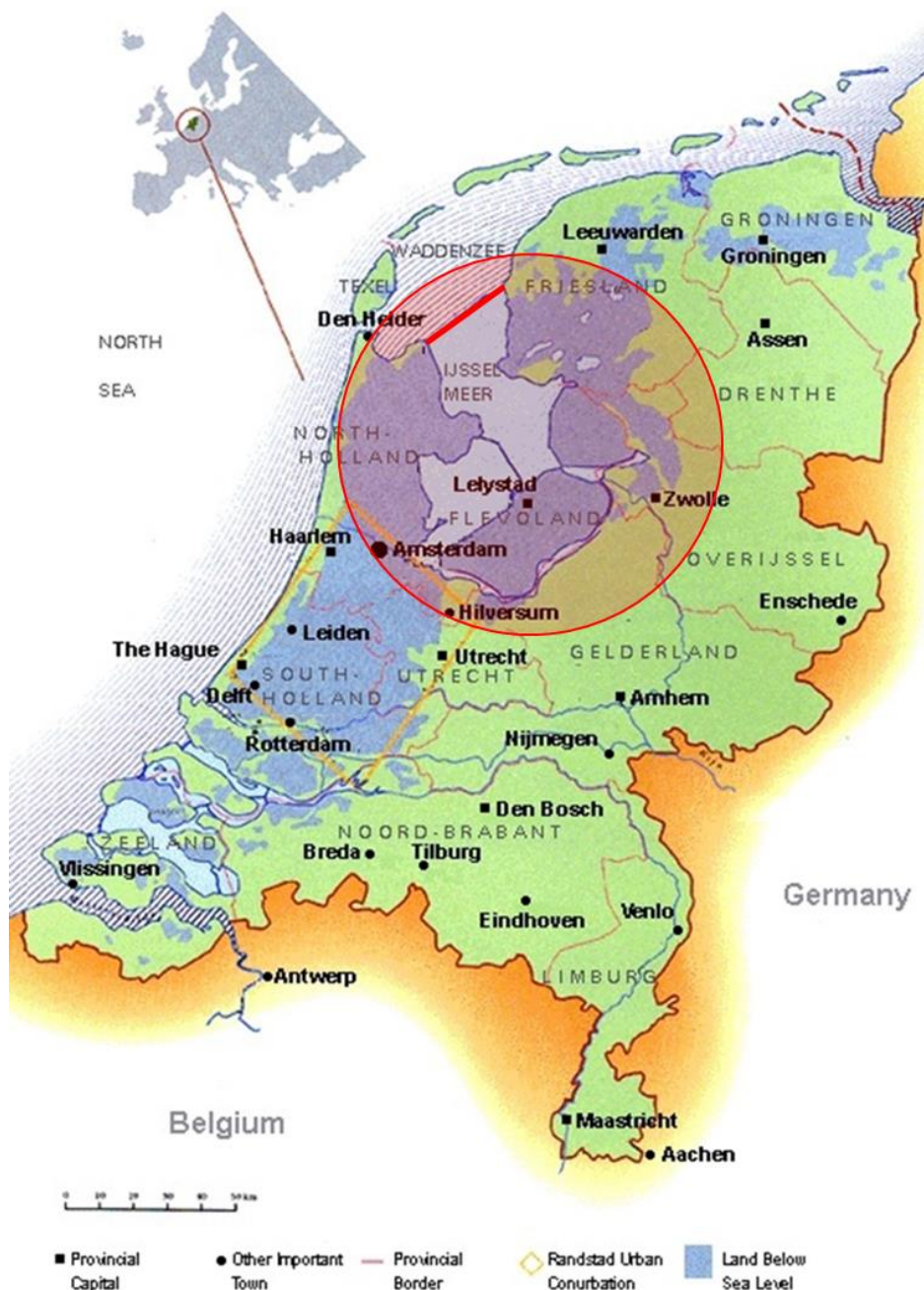
Figure 3. Overview of the Netherlands showing the low parts and highlighted in red the Afsluitdijk and the area it protects. (What-percentage-of-the-Netherlands-population-actually-lives-above-sea-level, 2018).

The Afsluitdijk separates the IJsselmeer from the North Sea. The water that enters the IJsselmeer from precipitation and rivers (mainly the IJssel) is discharged through two discharge sluice complexes, shown in Figure 2. A more detailed description of these structures in the original situation can be found in Appendix A.2. The problem with the discharge capacity is best explained with the use of Figure 4. The sea level is expected to rise further in the coming years, which will not only result in a lowering of the average natural discharge head, but as well as a decrease of time in which natural discharging can take place. Both result in a decline of the discharge capacity of the present complexes.
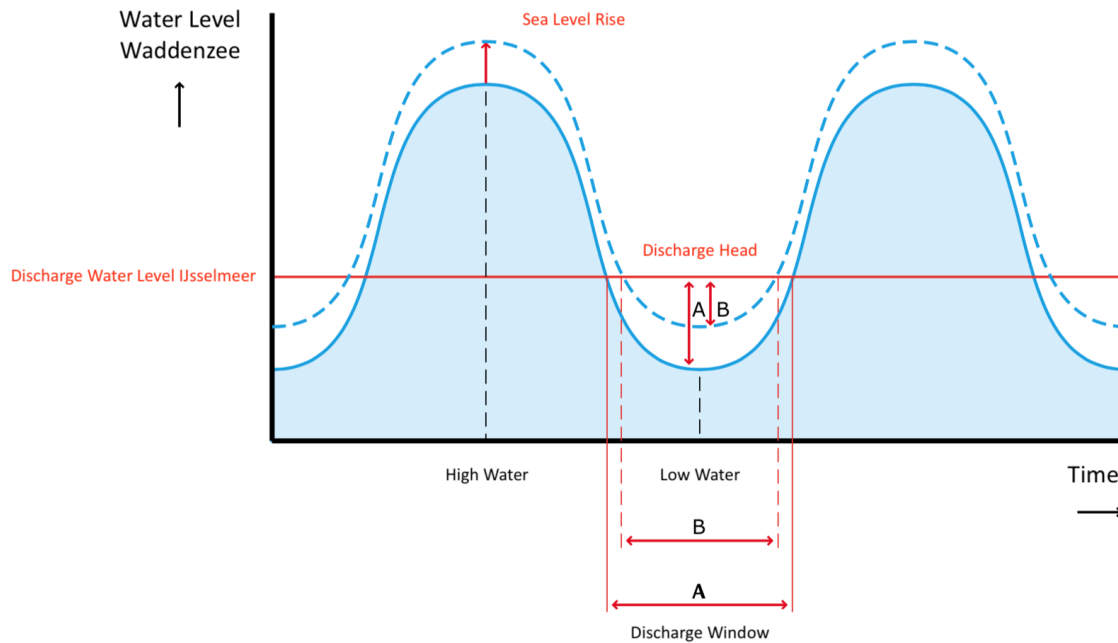
Figure 4. Problem situation of the discharge capacity at the Afsluitdijk (Witteveen+Bos, 2013).

1.2 Problem Definition

The amount of people living on this planet and in coastal areas is the largest in history. These people are moving closer to the water due to the lack of space. To protect them, large structures are needed in environments that can be extremely violent and dynamic. To build such structures with more confidence in the future, the understanding of dynamic fluid-structure interaction (FSI) is very important.

The discharge sluices in the Afsluitdijk contain relatively thin gates that would have to withstand wave impacts that occur with storms once every 10.000 year, see Figure 5. These gates are therefore a perfect example to study their method of design. As described in Appendix A.2.3, during a storm with a water level of NAP + 2.50 m, which is the exact same height as the bottom of the defense beam, high wave impact loads on the gates can occur. This beam is in the original situation in front of the northern gate. The reason the pressures on the gate are so large is because during impact the wave is trapped between the defense beam at the top and the gate at the front. The gate is relatively thin and will start to deflect on impact. During a storm with many waves, this dynamic behavior can be potentially problematic. The failure mechanisms that play a role are exceedance of the yielding stress and fatigue of certain parts. Failure of parts is caused when a single load exceeds the maximum resistance of the structure. The wave impacts lead to dynamic behavior which have a relatively low return period of approximately 1 year. Fatigue may therefore be an issue. The reference design that was made for the replacement of the Afsluitdijk gates has shown to have knowledge gaps regarding the estimation of the impact wave pressure and determining the response of the immersed gate structure including the involved FSI. Both are discussed in the remainder of this section.

Hofste (2012) and Hofland (2015) both have done small scale test to determine design forces for the Afsluitdijk situation with defense beam. They both found that at certain water levels, lower than the design conditions, the gate will be faced with the most severe pressures amplified due to the presence of an overhang. The situation with the overhang or defense beam is clearly seen in Figure 6. To mitigate this amplification of the force, the new design of the structures is adapted, see Figure 5. However, the governing load conditions are still based on test from Hofland (2015) and gates in a different location still have an overhang, see section 2.1. It is rather difficult to predict the force of

3

an impulsive wave load. Some methods are available, but none have been fully validated. An interesting mathematical method is described by Wood and Peregrine (1996) and is therefore numerically rephrased and analyzed in this research, see Chapter 5.
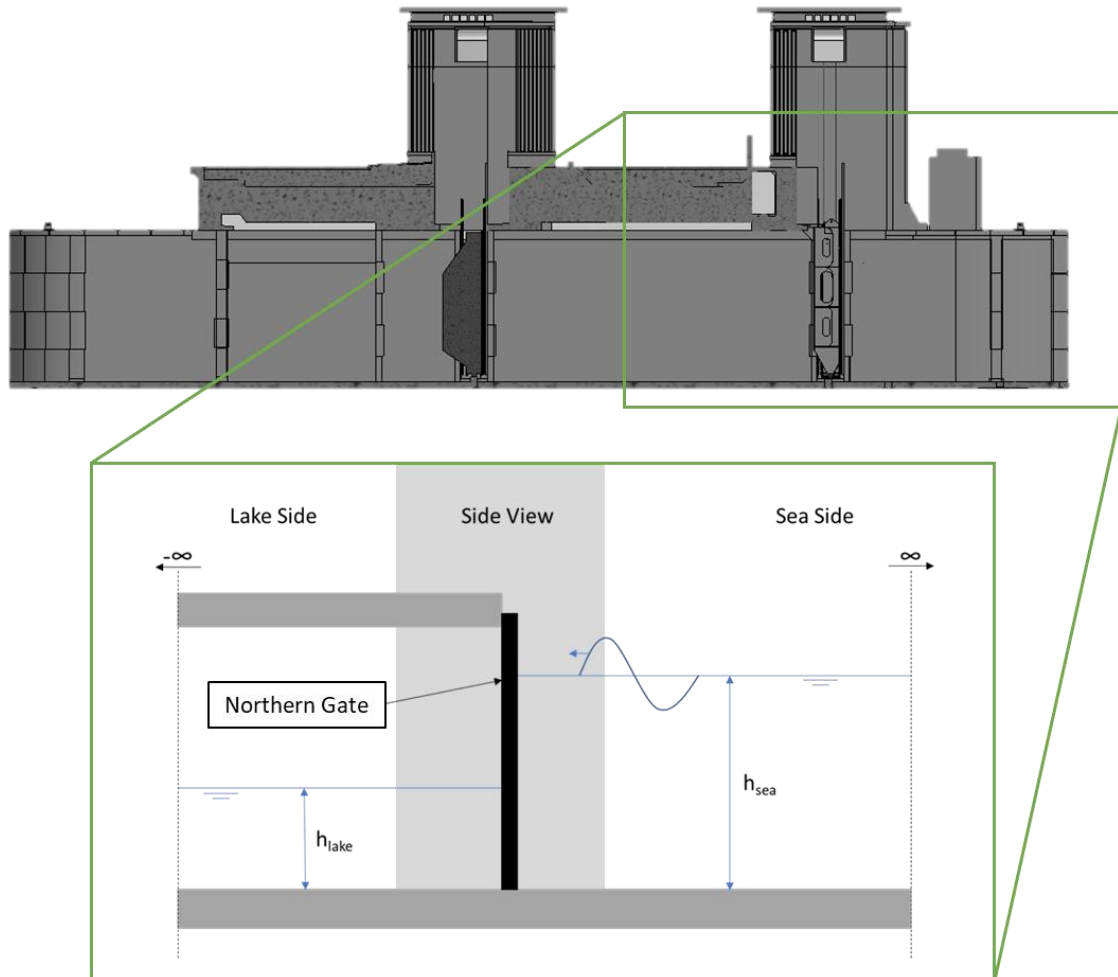
Figure 5. Simplification of the problem at the northern gate of Den Oever in the new situation.

In order to design relatively thin partly or completely submerged gates located in a wave climate there is no dynamic calculation easily available. The method that is most common in partly submerged structures, that must deal with wave impact, is the Goda-method. However, this method is not suitable for a dynamic calculation for structures with a relatively low weight. A dynamic calculation is needed when the structure itself responds significantly to each wave impact by a displacement, which is the case for relatively thin gates like the ones in the discharge sluices in the Afsluitdijk. The current approach to solving such a problem uses the method of Kolkman and Jongeling (2007). They simplify the problem to a single degree of freedom system (SDOF) in order to solve the entire problem quasi-statically. This is an improvement for low-weight structures compared to the Goda-method but still not precise as the simplification to a SDOF system does not always comply and no complete coupling between the fluid and the structure is applied.

Tieleman (2015) has derived a method that can possibly do a dynamic calculation of such a problem by using a semi-analytical model that includes the fluid-structure interaction. However, this method has not been applied or validated in many situations yet, making it an interesting method for further research. Tieleman et al. (2018) show that application of this method may for some cases result in

lower stresses than Kolkman and Jongeling (2007), potentially leading to a more economic design. The semi-analytical method yet depends on a representation of the gate by thin plate structures. When coupling the model with a sophisticated finite element method, more complex shapes and constraints are possible.

The scope of this study will be the design of gates in dynamic and impulsive environments, where the northern gate of the tower discharge sluice at Den Oever is used as a case. The case is used to compare the engineering practice with Kolkman and the dynamic fluid-structure interaction model also with coupling of a finite element method to analyze the real design instead of a thin plate with equivalent stiffness.

Furthermore, In the preliminary design phase it is difficult to perform dynamic calculations as the result is influenced by many parameters and variables. Coupling the semi-analytical FSI model with a finite element method could be sufficiently accurate for preliminary design yet computationally efficient. This opens the possibility to obtain a design based on a parametric model.

This has been executed in this research, see Chapter 0. An artificial intelligence is used to quickly find proposed optimal designs based on the chosen parameters and demands.

1.3   Research Questions

This section briefly describes the research questions that will be answered during the course of the study.

1. Can a numerical method based upon the theory of Wood and Peregrine accurately predict wave impact pressures for the situation of a gate with overhang? If so, can this method be extended to also predict the effect of evasive methods such as gaps above or in front of a gate?

2. What design method is most suitable to accurately predict the dynamic response to wave impacts for flood gates without overhang in general?

   a. Can the applicability of the recently developed semi-analytical FSI model be improved to fulfil this purpose by coupling this method with a FE model?

   b. How do the results of such a model in a case study compare to the approach taken in present engineering practice?

3. Can a parametric model based on the developed design method be used to (numerically) find an optimal gate design?

1.4 Research Methodology

To find an answer to the research questions the approach for this study consists of three major parts, that match the research questions in similar order:

- Step 1: Numerical verification of Peregrine's mathematical model
- Step 2: Development of the fluid-structure interaction model and comparison to engineering practice
- Step 3: Parametric model and optimization

These three steps can be seen as global steps of the process. Together the steps will help to improve the design method of submerged plate structures in a dynamic environment based on the Afsluitdijk as a case. In this chapter the reasoning behind the steps and their method of validation is explained. The complete hydraulic boundary conditions of the case can be found in the Appendix. The following sections briefly show the process and reasoning of each step.

1.4.1 Step 1: Numerical Verification (Peregrine)

The first global step is a verification of the method described by Wood and Peregrine (1996). The goal of this step is to be able to utilize a method that can calculate the horizontal pressures on a vertical surface where the design layout such as an overhanging structure play a role. Therefore, the focus is on the old sluice design with the defense beam in place. Although it is already known that this beam will be removed in the new design, it is still important for this research as model tests have been executed with this configuration. Figure 6 shows a simplification of the cross-section for this first situation.
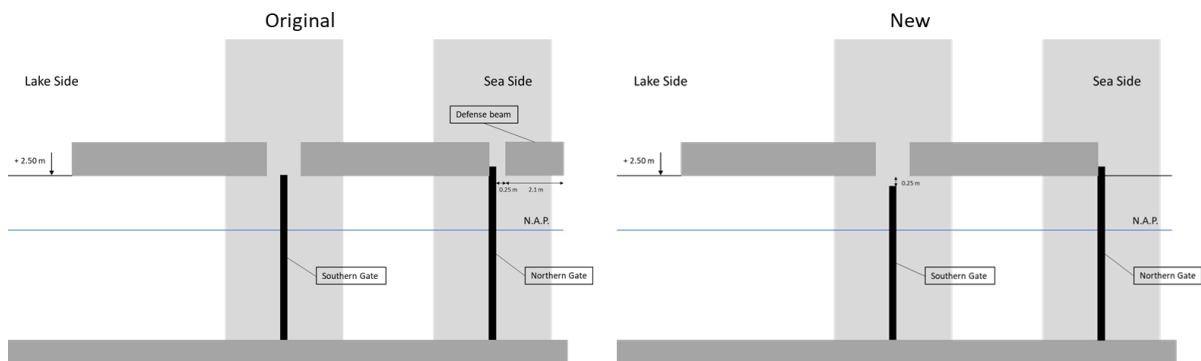
Figure 6. Schematization of the cross-section of the original (left) and new (right) situation at Den Oever.

The defense beam with a length of 2.1 m, see Figure 16, compared to the height of the gate (7.15 m) has a ratio of 0.3, is comparable to the ratios from 0.5 to 2 that were calculated by Wood and Peregrine (1996). Together with the experiments done by Hofland (2015) and Hofste (2012) makes it possible to compare the results with the theoretical method. This is indicated by the red and blue paths from Figure 7. The complete explanation of the mathematical method of Peregrine is found in Chapter 5. The paper of Wood and Peregrine (1996) gives an analytical solution using conformal mapping. This research uses a numerical adaptation that can replicate the solutions of Wood and Peregrine using their notion to directly calculate the pressure impulse field. When agreeable results have been reached, the numerical method will be applied to the same input variables as the model tests of Hofland (2015) in order to find an empirical relation.
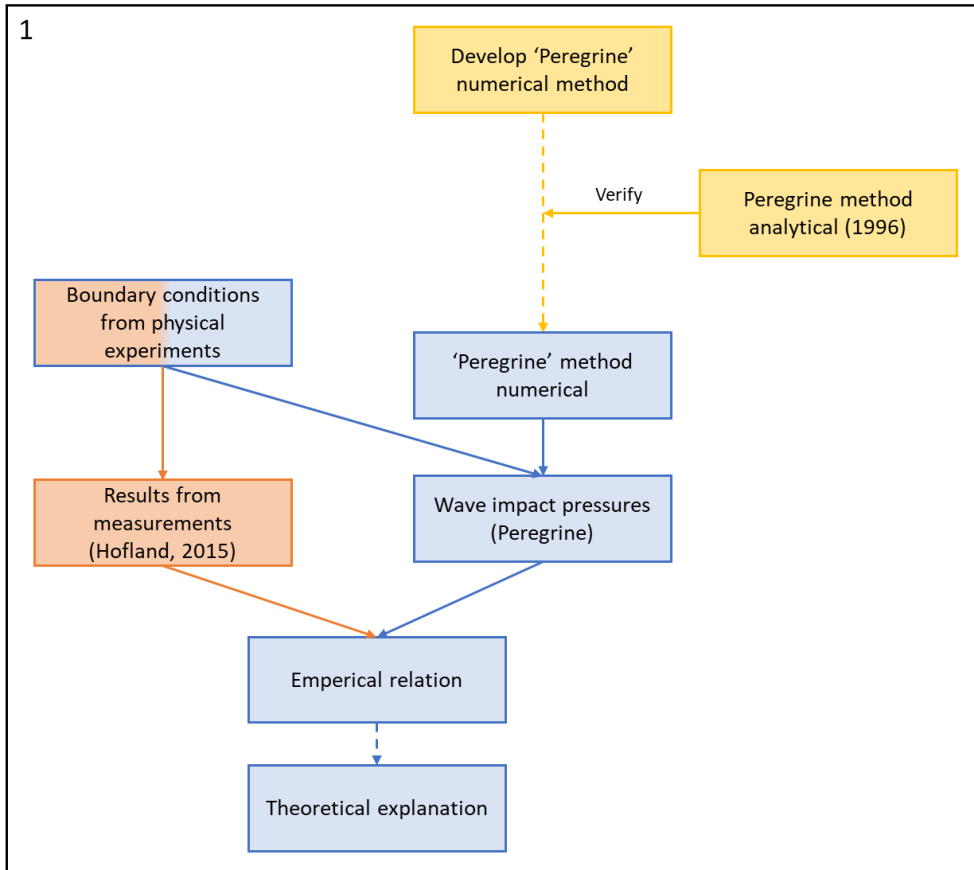
Figure 7. Schematization of the first global step (Yellow: Verification numerical method, Blue: Verified numerical method applied with BC's from Hofland (2015), Red: Results from physical experiment by Hofland (2015)) .

The first global step as is shown in Figure 7, is focused on the verification and use of the notion prescribed by Wood and Peregrine (1996) of calculating the pressure impulse field directly. The arrows returning in the process indicate an internal iteration step for either a verification or a modification because of an unsatisfying result.

1.4.2 Step 2: Comparison of Design Methods
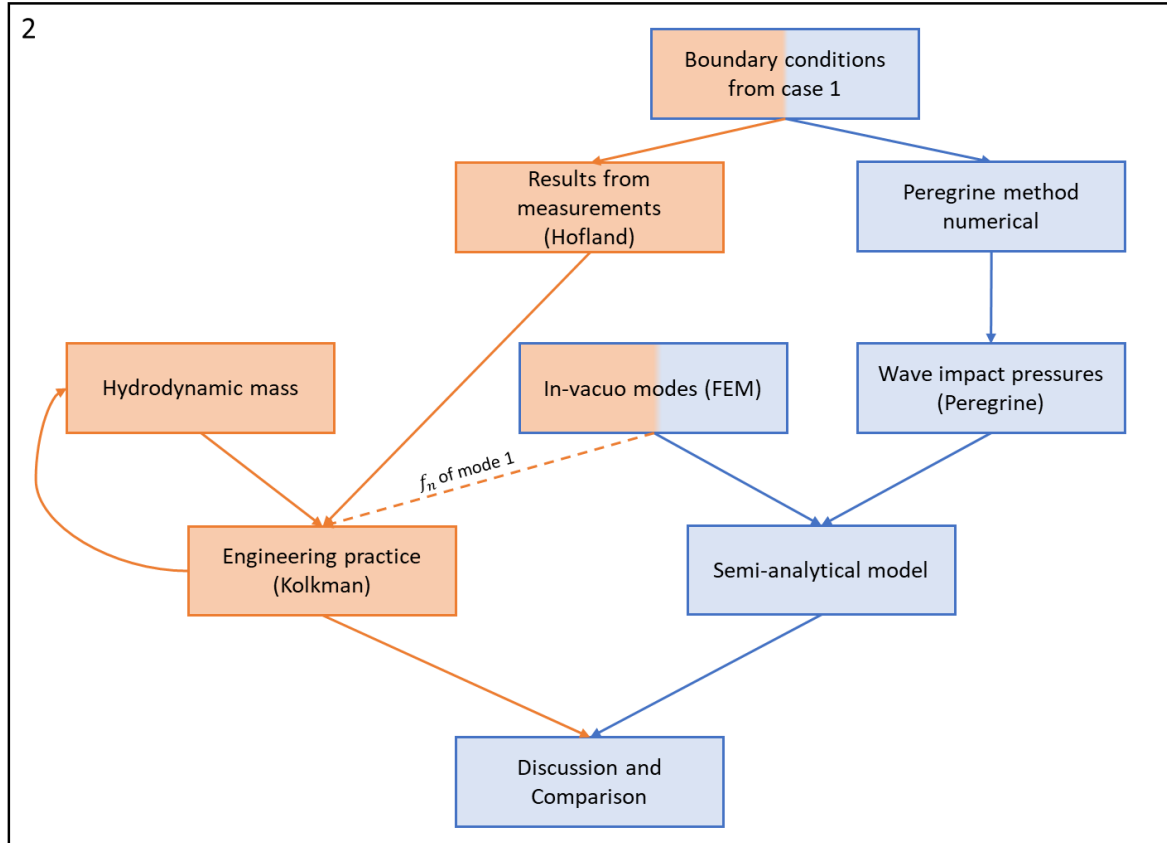
Figure 8. Schematization of the second global step (Red: engineering practice based on Kolkman, Blue: semi-analytical method).

An overview of the second global step is found in Figure 8. The goal of this part of the research is to analyze and compare both methods as shown in order to find a recommended approach for a relative thin-plated structure subjected to wave impact. This will be done by utilizing the case of the Afsluitdijk. This case uses the measurements of Hofland (2015), which is important for the verification of the semi-analytical method. The case concerns the northern gate of the discharge sluice complex at Den Oever, see Figure 9. The complete explanation of the Kolkman method, which is the current engineering practice, is found in Chapter 3 and will not be discussed here. The Kolkman method is indicated by the red path and is compared with the blue path, which indicates the semi-analytical method containing Fluid-Structure Interaction (FSI) based on the method of Tieleman (2015). This FSI model receives its input from the Peregrine method. This second global step focuses on the comparison of the current method (Kolkman) and the experimental method (Tieleman) that has theoretically more potential. The semi-analytical method is coupled with a Finite Element Method (FEM) that allows for complex structural shapes and analysis of real designs without simplifications.
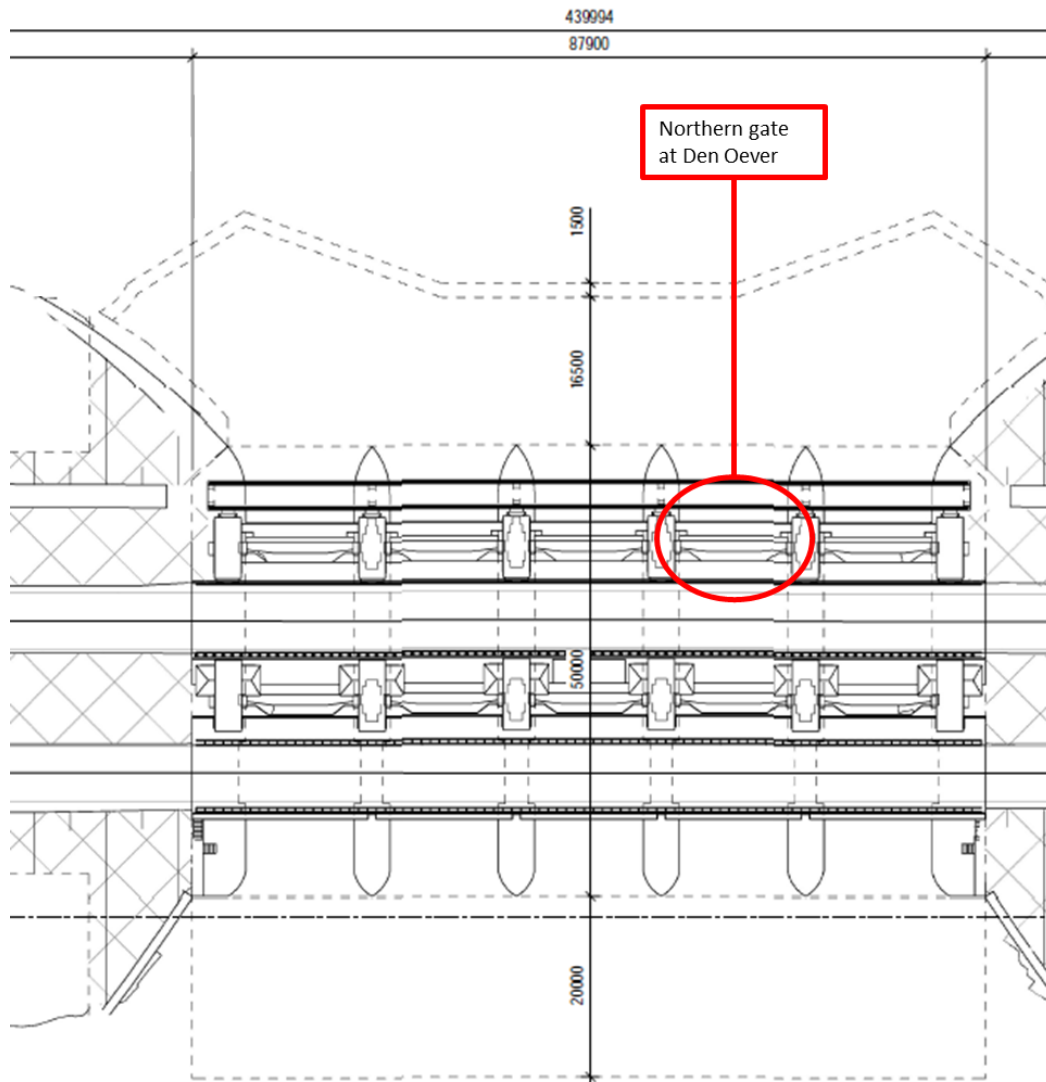
Figure 9. Top view of discharge sluice gates at Den Oever with the case highlighted (red).

1.4.3   Step 3: Parametric Model and Optimization

The last step of the research introduces a parametric model based upon the semi-analytical model coupled with a finite element method. The model contains a simplified gate design for the Afsluitdijk case, but with many variable parameters. Because of the dynamic properties of the calculation, it is difficult to grasp the influence of each parameter correctly. Therefore, an artificial intelligence based on genetic algorithm and neural networks is created to find the optimal design for the case. The optimization is based on the lowest amount of material volume in the structure while still maintaining a sound structural design according to a built-in structural analysis. The goal of this step is to see if it is possible to find a more optimal design by implementing the semi-analytical model coupled with a finite element model.

1.5 Report Structure

A schematic overview of this report's structure is given in Figure 10. Chapters 2 to 4 contain description of the system and required background information needed to understand and solve the problem. Chapter 2 gives a description of the Den Oever northern gate case. This includes an overview of the design of the new complex at Den Oever concerning the redevelopment of the Afsluitdijk. The design shown functions as the input in further analyses in this report. The current engineering practice, which is based on the quasi-static Kolkman method, is the first. This method is analyzed with regard to the design of Chapter 2 in Chapter 3. 3.3 contains an analysis that gives clarification on the application of this method. The governing hydraulic conditions of the new design are found Appendix B, and are used for the calculation according to the engineering practice in section 3.2 and other models in this thesis.

Chapter 4 provides some theoretical background to support the methods applied in this thesis in Chapters 5 and 6. Also, some viable research relating to the case of the Afsluitdijk are shown and examined and are used as input in Chapter 5 to test the developed numerical method.

Chapter 5 focusses on the loading of the system and is the start of the first step in the research. The gate is primarily loaded by wave impact and because of an overhanging structure in the original design, the governing load is difficult to determine. The engineering practice used model tests, examined in Chapter 4 to determine a pressure distribution, but section 5.2 shows that a numerical method, explained and validated in Appendices D and E respectively, is a possible alternative.

The description of the semi-analytical model with fluid-structure interaction based upon a coupled modal analysis can be found in Chapter 6. A method is shown how to link this semi-analytical model to a finite element model in order to solve more complex designs. The comparison with the current engineering practice from Chapter 3 is made with the same case from Chapter 2.

Chapter 7 refers to the same semi-analytical model from Chapter 6, but with the addition of a parametric model. This parametric model further analyses the application of the semi-analytical model by optimizing a design focused on the governing load cases. This optimization is ruled by an artificial intelligence that can optimize such a problem in a fraction of the time, see section 7.2. Finally, the conclusions and recommendations are made in Chapter 8.
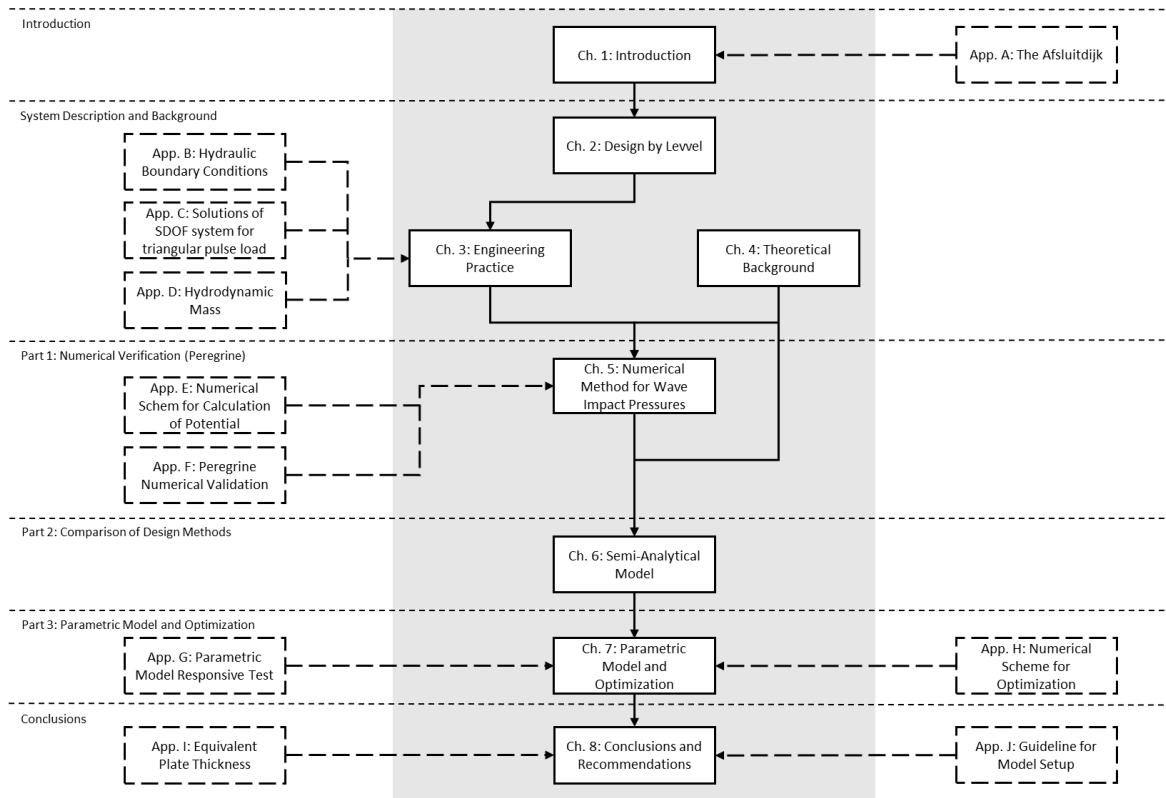
Figure 10. Schematic overview of report structure.

2 Design by Levvel

Consortium Levvel is responsible for the reinforcement of the complete Afsluitdijk, however the scope of this report will focus on the discharge sluice complex at Den Oever. As explained in the previous chapter the case examined will be the northern gate at the tower discharge sluices. This chapter will briefly explain the complete design of Levvel at the discharge sluice complex at Den Oever, before going more in-depth on the renewed design of the tower discharge sluices, see 2.2. The last two parts of this chapter contain an analysis of the design of the gate itself and an overview of the structural criteria respectively on which the design is based.

2.1 Discharge Sluice Complex

The design is still in development by the engineers of consortium Levvel. The final design, which will be built, can therefore differ from the figures and dimension shown in this chapter. Figure 11 shows the differences in the original complex and the new design. The differences are very much integrated into the original design and can be hard to spot.

Figure 11. Original view of the discharge sluice complex at Den Oever (top) and 3D view of the new design (bottom) (WEB: flickr.com/photos/siebeswart/28446128408, aerial photo from Siebe Swart; WEB: http://www.waterforum.net/rijkswaterstaat-gunt-project-afsluitdijk-aan-consortium-levvel/).

The new layout can be divided into three parts, see Figure 12. The tower discharge sluices (green), which are the original discharge sluices and will be discussed in more detail in the next section as they are part of the scope of this research.
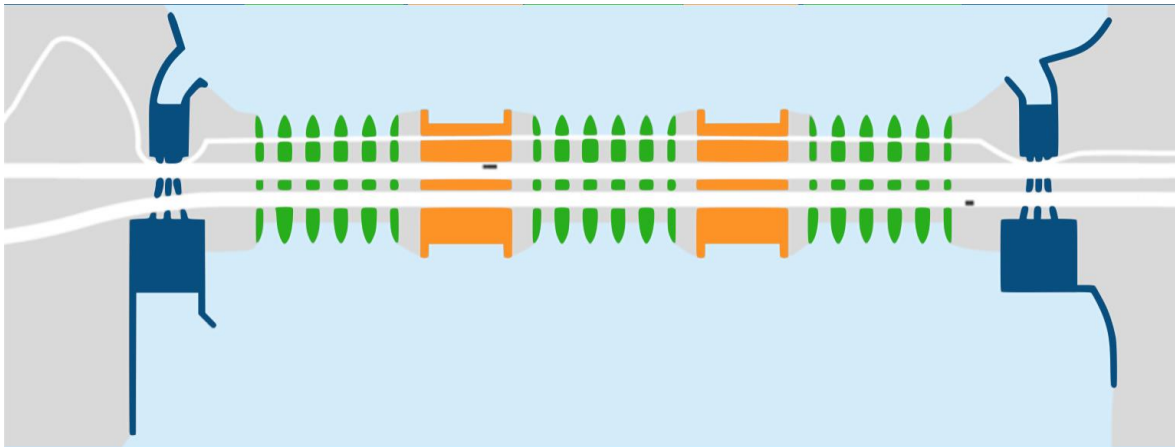
Figure 12. Top view basic layout of the Stevinsluizen as designed by Levvel. Green are the tower discharge sluices. Orange are the new discharge sluices. Blue are the new pumping stations.

The two islands separating the three tower discharge sluices will each contain 4 extra sluices to increase the natural discharge of the excess water of the IJsselmeer, see Figure 12 in orange. These new discharge sluices are designed to minimize the visibility of the gates as an aesthetic choice, which is why they are tucked away in the structure, see Figure 13.

Figure 13. Artist impression of the new discharge sluices at Den Oever (WEB: http://www.waterforum.net/rijkswaterstaat-gunt-project-afsluitdijk-aan-consortium-levvel/).

At last, the largest pumping stations of Europe will be placed at either end of the existing sluice complexes, see Figure 12 in blue. Each station will contain three large pumps. An impression of the cross-section can be seen in Figure 14. The pumping stations are needed if the sea water level will become so high that the discharge sluices, even with the new sluices, do not have a natural outflow large enough to fulfill the requirements.

Figure 14. Artist impression of the new pump station at Den Oever (https://www.architectuur.nl/nieuws/benthem-crouwel-architects-versterkt-afsluitdijk/)

2.2 Tower Discharge Sluices

The old discharge sluices or tower discharge sluices will be redeveloped. They are located at the green highlighted places and each section contains five sluices. As mentioned before, each sluice has two gates, a northern at the Waddenzee-side and a southern at the IJsselmeer-side. The overall outer appearance of these complexes will stay the same, see Figure 15, but many modifications will be applied; The entire sluices will be renovated to prevent the further degradation of the concrete; The defense beam will be removed; The bottom protection will be enhanced; A new gate lifting system will be installed inside the towers and new gates will be placed. This section will focus on the removed defense beam, the new lifting system and the location of the gates. The northern gate will be analysed in the next section.
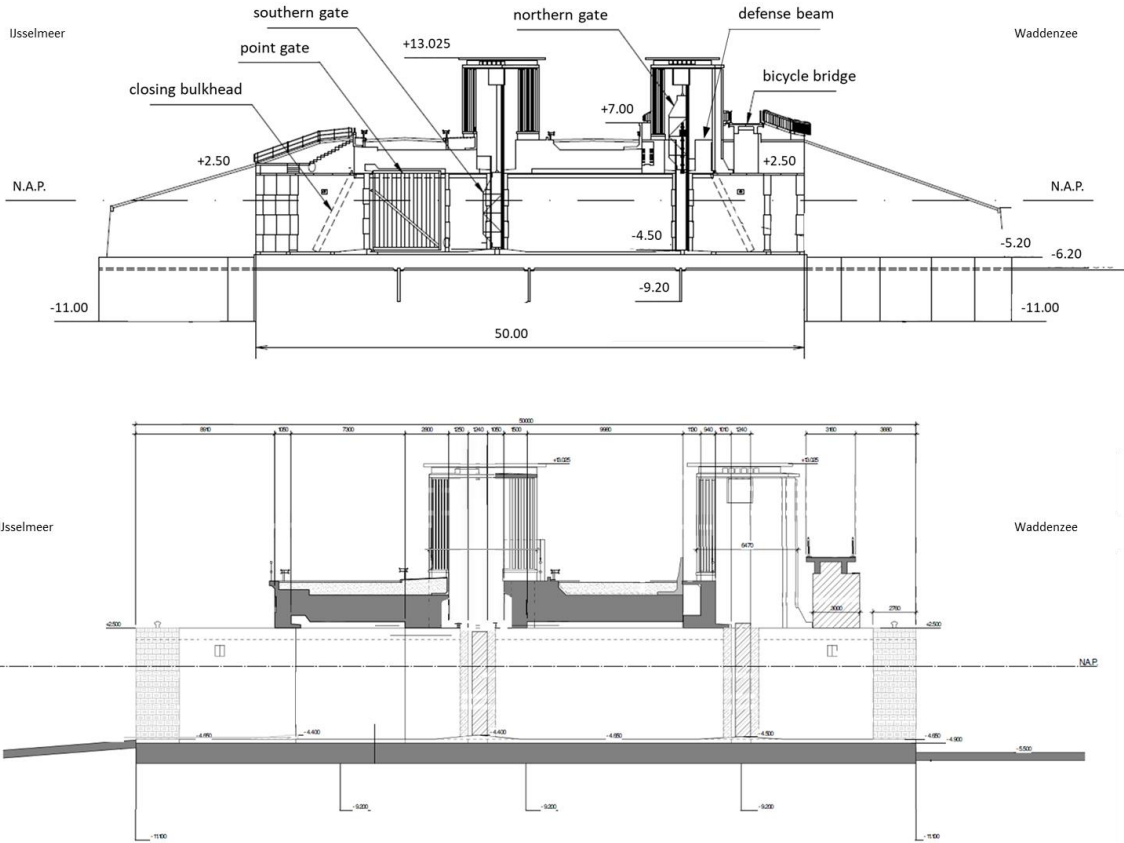
Figure 15. Side view of the original (top) and new (bottom) tower discharge sluice at Den Oever.
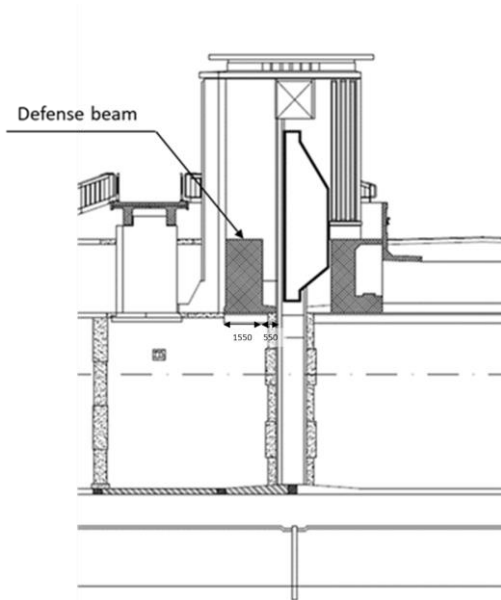
Figure 16. Detail of the original structure of the northern gate also depicting the defense beam.

The gates are just like in the current or old sluices 15.85 m apart. The defense beam, located in front of the northern gate, see Figure 16, will be removed to prevent the amplification of the wave impact of a storm with water levels lower than the bottom of the beam. This is further discussed in Chapter 5. The beam is also obsolete for its design purpose, which was to prevent impact of a bomb during war. Figure 17 shows the detail of how the top of the gate will lean against the concrete structure of the complex. This to avoid water from entering the area between the gates in situation of high-water

levels, which potentially could lift the entire concrete road deck and damage the structure. This concrete deck is the exact negative of the shape, which is why the top of the northern gate fits perfectly.
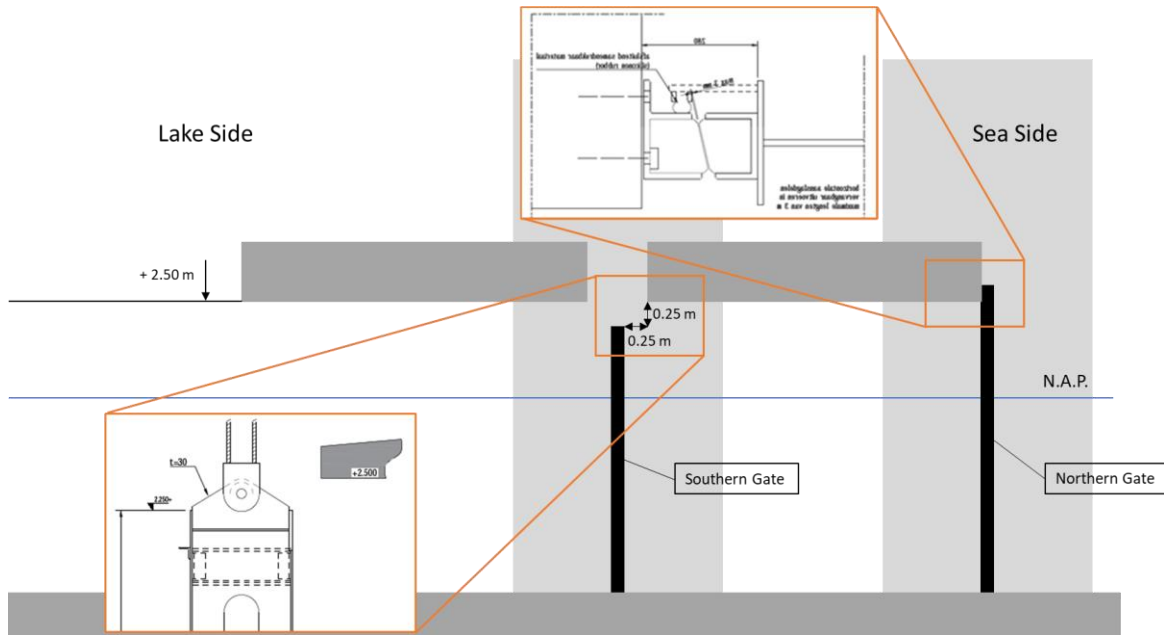
Figure 17. Schematic cross-section of the new discharge sluice with detailing of the top of each gate.

The southern gate is different in the sense that it does not contact the concrete deck. Figure 17 also shows this detail. The distance between the edge of the gate and the concrete is 0.25 m. In the same figure it can also be seen that the gate is lower than bottom of the concrete deck. This distance is also 0.25 m and is designed to avoid a part of the load.
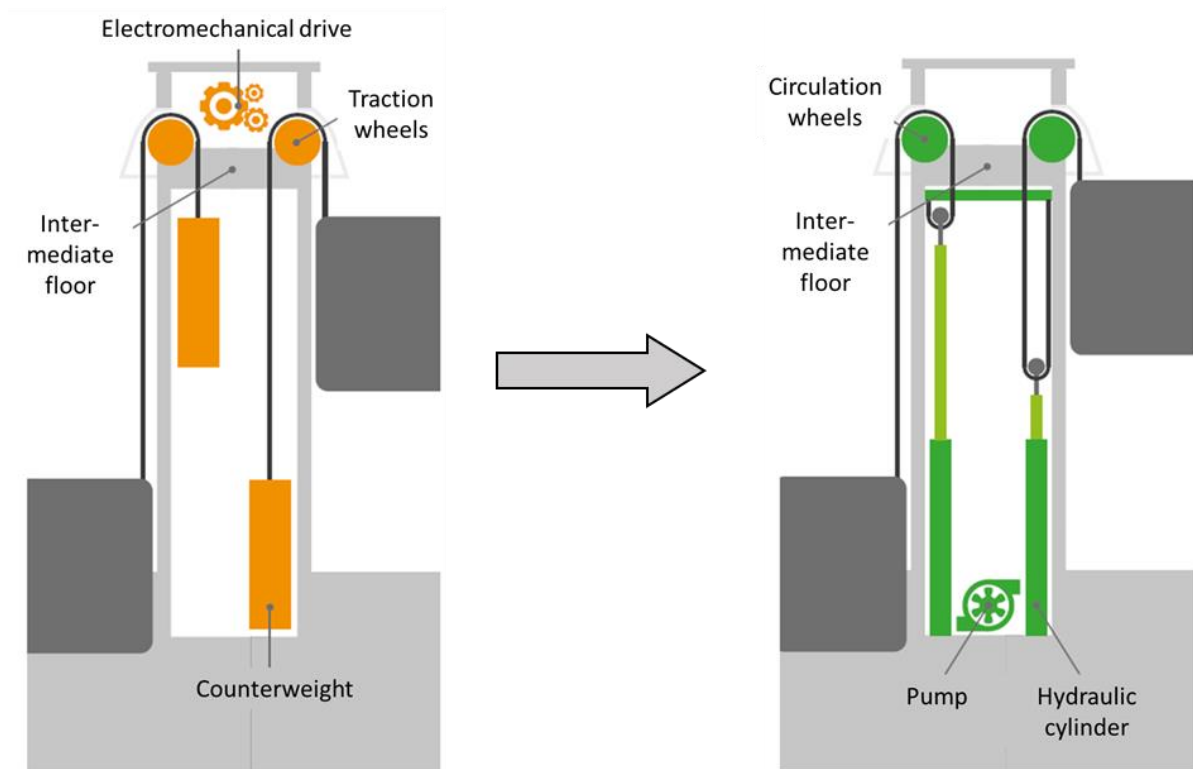
Figure 18. Schematic overview of the replacement in the gate lifting system in the tower discharge sluices (Witteveen+Bos, 2013).

16

The lifting system of the gates will be removed and replaced by a different kind. The old or current system is a mechanical lifting system which will be replaced by a hydraulic one. Figure 18 shows the replacement of the lifting system in a schematic overview. In the new lifting system, the gates will be guided by friction instead of rollers as it originally was.

2.3   Design of Northern Gate

The case analyzed in this research focusses on the northern gate at Den Oever. In the previous sections the surrounding of the gate has been shown, where this section will go into detail on the structural design of the gate itself. Figure 19 shows the complete design as it will be used in this thesis.
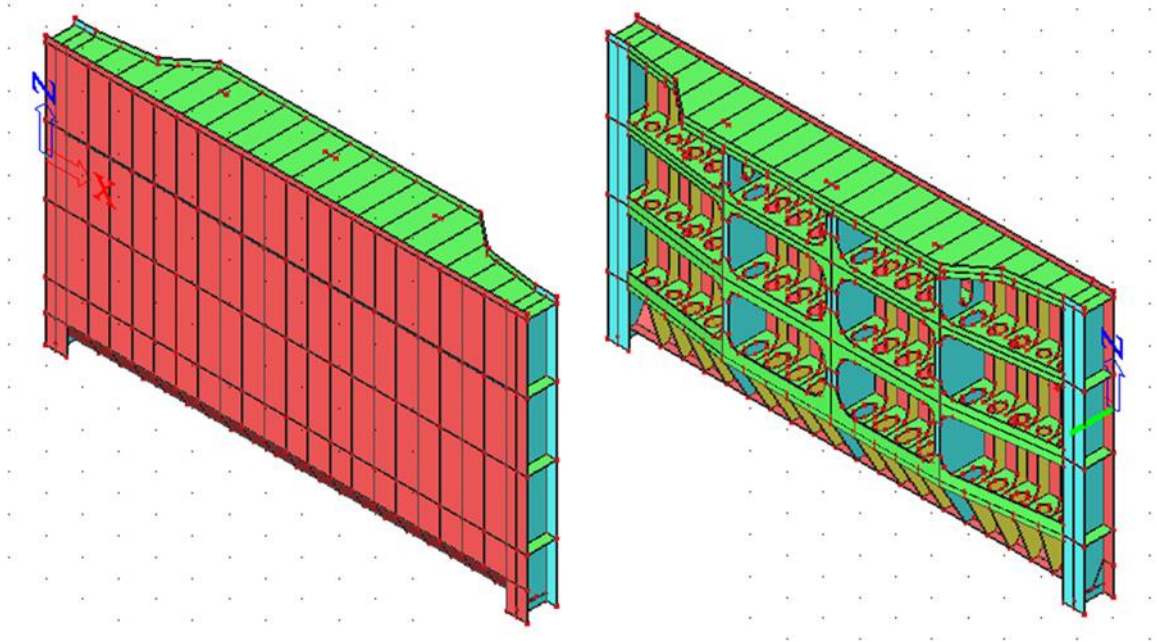
Figure 19. 3D rendering of the front (left) and back (right) of the new northern gate at Den Oever in SCIA from Levvel.

The basic layout of the gate can be simplified to the main plate that faces north and several stiffeners facing south. The location and size of these stiffeners is of importance, because it influences the overall stiffness and strength of the gate, see Figure 20. The thickness of the plate, webs and flanges of the structural parts of the gate are all 15 mm.
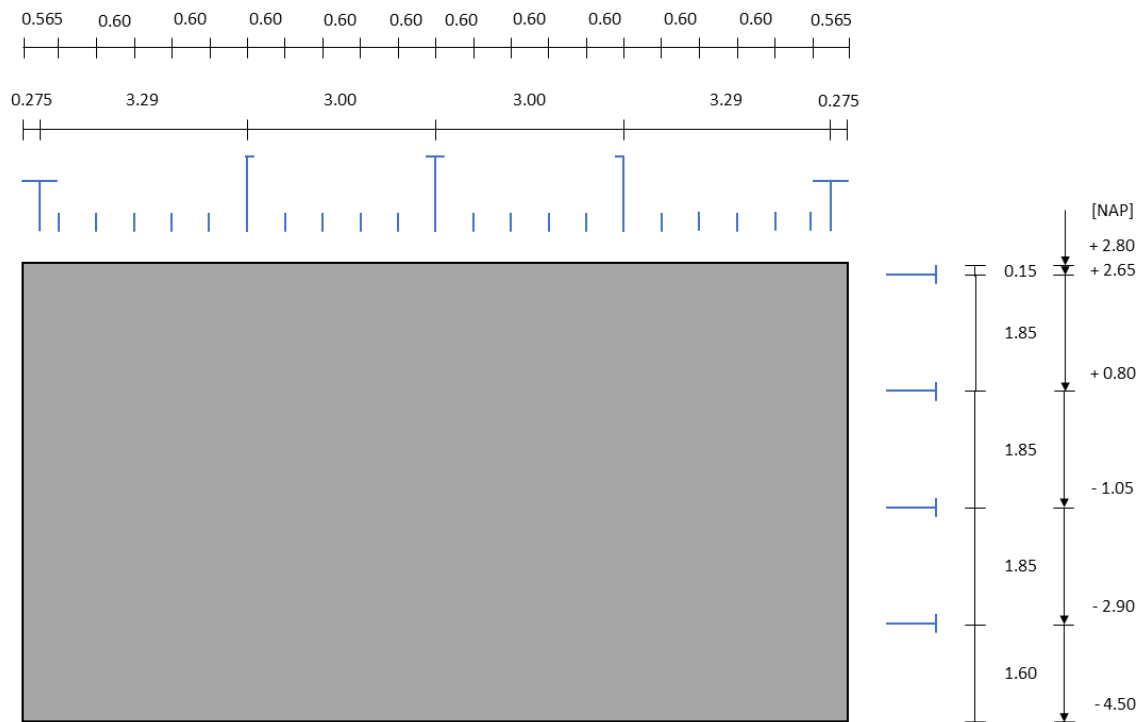
Figure 20. Location of the vertical and horizontal stiffeners (blue) in the northern gate at Den Oever [m]. Heights (NAP) are in closed position.

The location of the supports, especially in the horizontal direction, are important in the description of the design, see Figure 21. The gate is modeled with supports on 3 edges in a closed position. The top is a line support and both sides are modeled with point supports as the new guiding system is best described by such supports. Vertical supports are less important as the main loading in this thesis is based on horizontal wave impact.
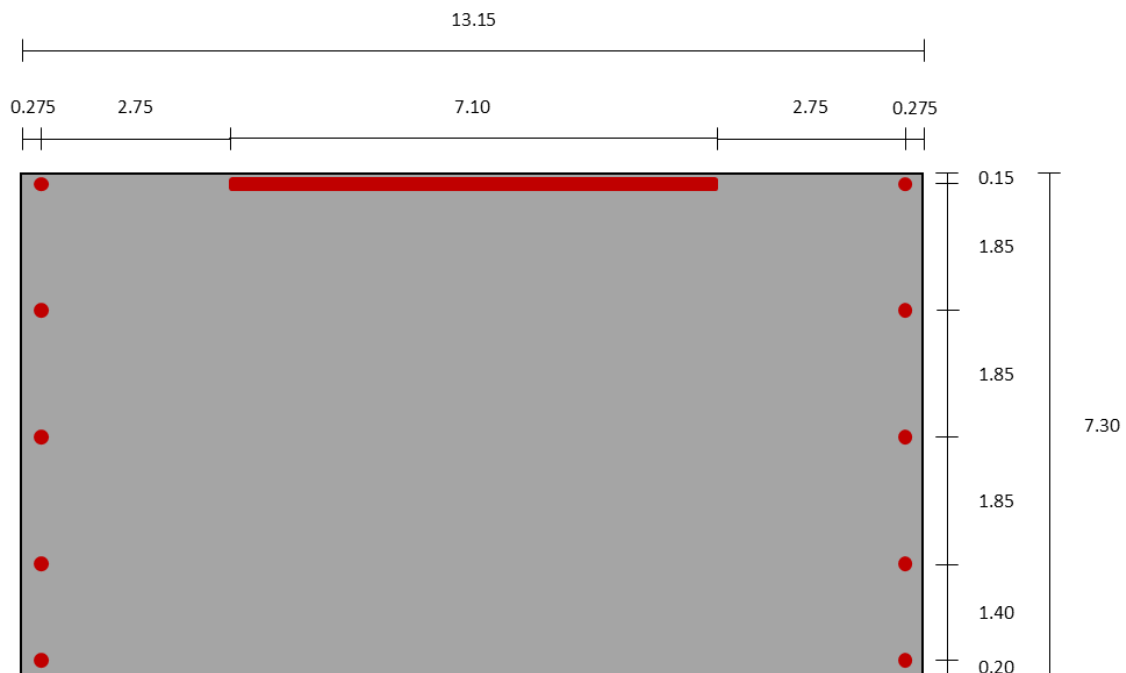
Figure 21. Location of the horizontal (y-direction) supports in the northern gate at Den Oever (10 point supports and 1-line support) [m].

The bottom of the gate has a sharp edge, see Figure 22. This is important when modelling the gate, because of the angle that front plate shows. The reason for this relative sharp bottom is to minimize the vertical motion due to horizontal flow underneath the gate in a partially open situation.
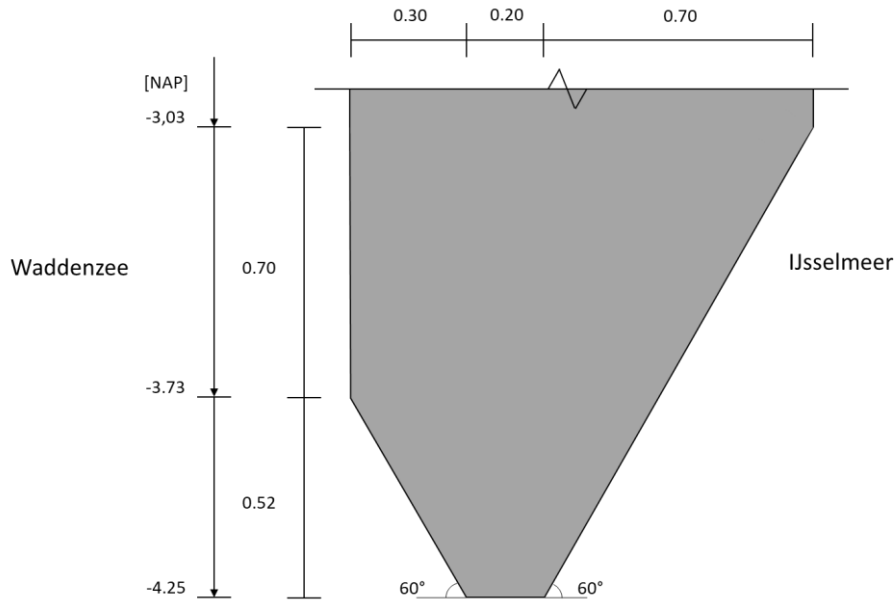
Figure 22. Simplified cross-section of the bottom of the northern gate at Den Oever [m]. Heights (NAP) are in closed position.

2.4   Structural Analysis

This section contains an overview of the structural analysis that forms the base of the gate design. The gate will be subjected to loads in different situations and should be able to withstand these within the demanded criteria, which are derived from the Eurocode. Three of these criteria are mentioned as they apply to the case of this research. The situation from the case is in the ultimate limit state, which is why the criteria are also shown in the ultimate limit state.

2.4.1   Yield Strength

The entire structure consists of different shaped sheets of solid steel, as seen in the previous section. The steel has quality S355, which shows the strength of each section. A stress higher than 355 N/mm^2 will result in yielding. Using a finite element method, the entire gate can be reviewed in detail and should suffice. The yield criterion that the applied finite element method uses is an equivalent three-dimensional stress based on the Huber-Hencky-Von Mises criterion, see Figure 23. Equations 2.1 and 2.2 show how the translation from the basic stresses to the principle stresses eventually result in the equivalent stress (σ_E).

$$\sigma_E = \sqrt{\sigma_1^2 + \sigma_2^2 - \sigma_1 \sigma_2} \qquad\qquad 2.1$$

$$\sigma_{1,2} = \frac{1}{2} \left(\sigma_x + \sigma_y \pm \sqrt{\left(\sigma_x - \sigma_y \right)^2 + 4\tau_{xy}^2} \right) \qquad\qquad 2.2$$
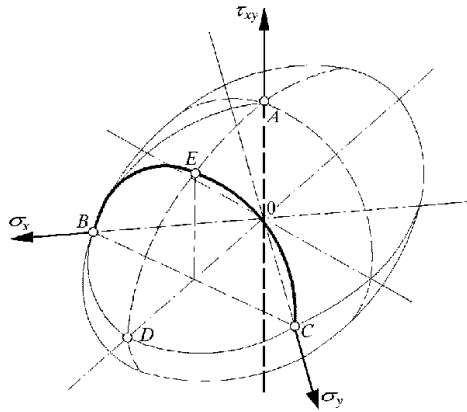
Figure 23. 3D visualization of the yield criterion according to Huber-Hencky-Von Mises (Cichanski & Sempruch, 2005).

Certain sections can result in a higher stress than the yield criterion allows. This section will then be plastically deformed. The structure will not immediately fail as it can redistribute the load to sections that still have elastic capacity. These, most of the time, local sections are calculated by hand and do not need the application of the finite element method.

2.4.2 Fatigue

A structure subjected to cyclic loading, when the nominal maximum stress values are typically less than the yield limit, can result in progressive damage. This process of weakening of the material is called fatigue. Designing a structure to prevent failure by fatigue requires an analyzing method as provided by the Eurocode, see Figure 24 for an overview. This cumulative damage method analyzes the loading and focusses on the cyclic behaviour of the expected stress in the lifetime of the structure. Important is the data used for the estimation of the fatigue strength as well as the type of cycle counting method. In Figure 24 the reservoir method is shown as example, but other methods like level-crossing, peak, simple-range and range-pair cycle counting methods are also available (Standard Practices for Cycle Counting in Fatigue Analysis, 1997).
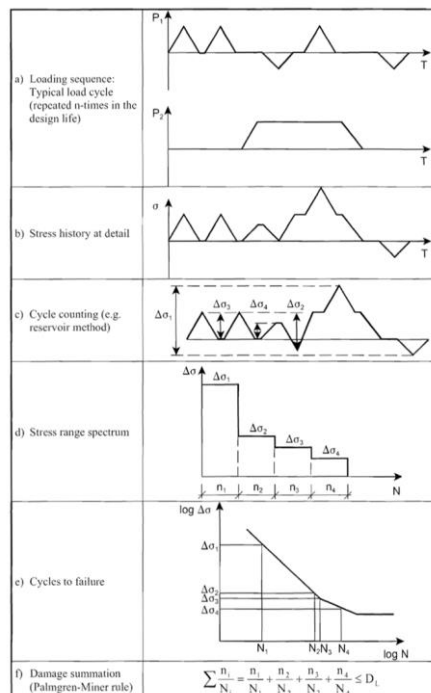
Figure 24. Cumulative damage method (Eurocode 3: Design of steel structures (EN 1993), 2005).

The welded connections in the gate design can fail due to fatigue. The gate consists entirely out of steel and the connections between the different sections such as the stiffeners and the plate or even the separate section of the main plate is all welded. The design conditions for the discharge sluice gates are composed of storms with various return periods. A storm increases and decreases in strength over a period of several hours. Within the rise and fall, different wave conditions are found. Those wave conditions can all contribute to possible failure by fatigue. The storms have been simplified and deconstructed to a few representative conditions over a longer period, to see if such failure occurs, see Figure 25. The stress at the locations of the welds are calculated by FEM for all the representative conditions from the considered storms. The stresses are related to several cycles and together the structure can be checked for failure by fatigue.
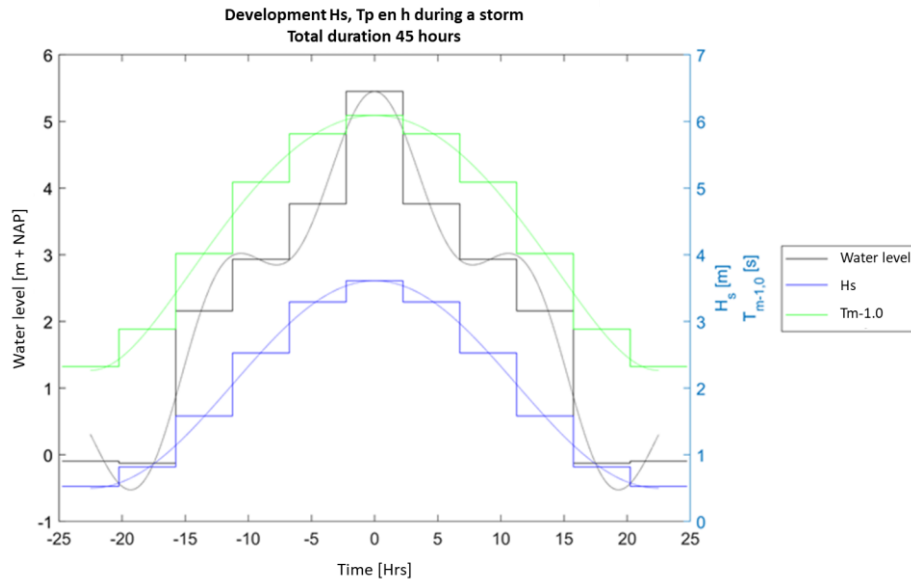
Figure 25. Representation of the parameters for a storm with a return period of 10.000 years for fatigue calculation.

2.4.3 Stability

The check for stability is focused on the buckling resistance of the main plate of the gate design at the Afsluitdijk. To establish the buckling resistance of a structure or part of a structure two methods can be applied. Using a finite element method, the buckling eigenvalues (k_g) and modes can be found by performing a stability analysis. The governing buckling mode (usually the lowest mode) is selected together with the location of the buckling representative stress (σ_{rep}). The location of this point will be the first to yield when the structure is loaded to its buckling resistance. The critical buckling stress (σ_{cr}) is found using Equation 2.3 as well as the reduced slenderness ($\bar{\lambda}$) with Equation 2.4.

$$\sigma_{cr} = k_g \cdot \sigma_{rep} \qquad\qquad 2.3$$

$$\bar{\lambda} = \sqrt{\frac{f_y}{\sigma_{cr}}} \qquad\qquad 2.4$$

Finally, the buckling resistance is calculated with Equation 2.5, where S_{rep} is the maximum von-mises stress in the representative load case. The buckling curve can be found with tables in the Eurocode and is sensitive to imperfections, residual stresses and post buckling behaviour.

21

$$R_d = \frac{\kappa f_y S_{rep}}{\gamma_m \sigma_{rep}} \qquad 2.5$$

Another method is to simplify the problem into a large beam, where the stiffeners are represented by simple supports, see Figure 26. The waves are interpreted as a distributed load. The calculation is then executing by Euler's formula. The difference between the two methods is that the second one is more conservative as it does not take any reduced effective length into account.
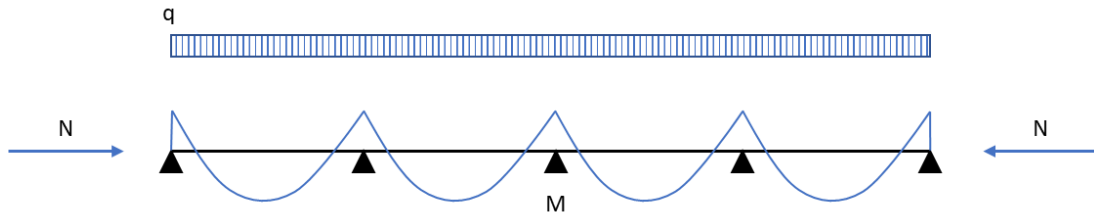
Figure 26. Simplification of the buckling problem of the main front plate.

2.5 Conclusion

The new structures will be integrated in the original complex and will hardly be noticeable, due to the design criteria composed by RWS. It also resulted in the fact that the towers that contain the lifting mechanism will also be reused. However, the large defense beam in front of the original discharge sluices will be removed. The northern gate that is right behind the defense beam will receive a new design and will lean against the top concrete deck with its top horizontal stiffener. This gate is also used as the case to compare both design methods analyzed in this thesis in Chapter 3 and 6. The structural analysis briefly explains the method applied to check the strength of the design, however some have been left out like the calculation of the main buttresses. The main buttress is the beam that supports the gate at the sides in the tower. The focus of the structural analysis lies in the mechanisms that translate to the analysis of the parametric model in Chapter 0.

3   Engineering Practice

The international or national building code does not specifically state anything on how to deal relatively thin-plated structures partly submerged in a fluid actuated by dynamic loading. However, the structure is not allowed to fail in conditions that are below its design requirements. This results in a conservative approach to make sure the design does not fail due to amplification of the dynamic behavior. This chapter analyzes the approach of Witteveen+Bos to the dynamic wave impact problem at the discharge sluice gates at Den Oever and Kornwerderzand. The results described in this thesis can differ from what is used in the actual designs but share the exact same approach and assumptions. Section 3.3 contains an analysis for clarification of the Kolkman method and allows an engineer to understand the system in an early stage of the design when a wave spectrum is known.

3.1   Kolkman Method

Kolkman and Jongeling (2007 B) have derived an approach to solve such problems as are encountered at the discharge sluice gates at Den Oever and Kornwerderzand. The method they advise is a quasi-static solution based upon a Single Degree of Freedom system (SDOF) and is currently the only method applied in such situations. Figure 27 shows the approach based upon the situation at the Afsluitdijk.
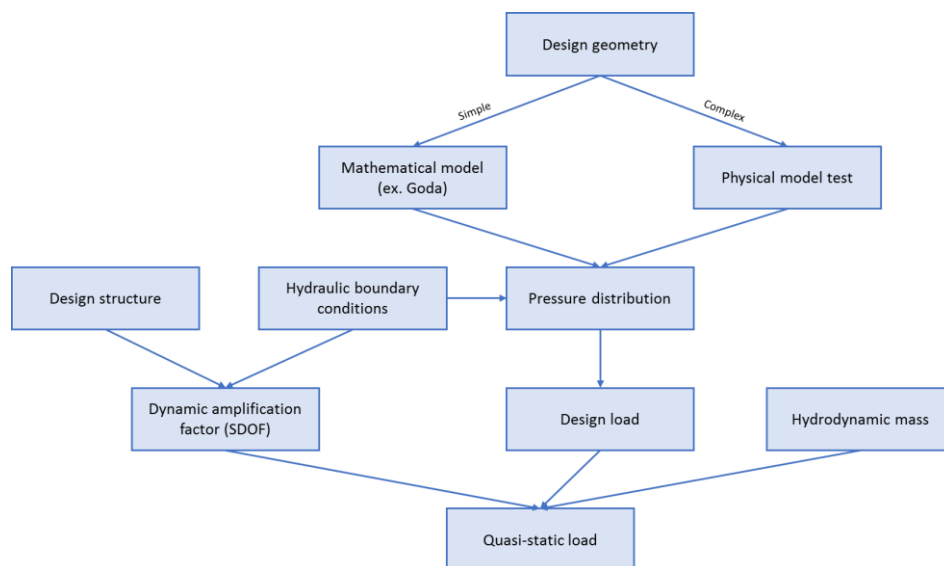
Figure 27. Schematic representation of the Kolkman approach for a structure partially or completed submerged in water

The most important contribution of the method is the Dynamic Amplification Factor (DAF). This factor is based upon the dynamic response of the SDOF system. A SDOF system contains only a single point of mass that can be set in motion in a single direction, see Figure 28. Such a system can be used to describe the dynamic displacement triggered by some force.
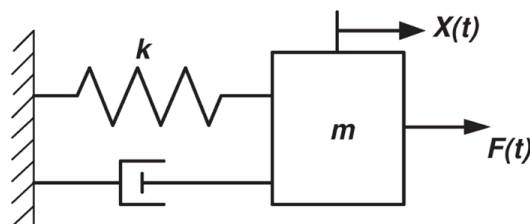
Figure 28. Schematic representation of a mass-spring damper system (SDOF) (Kolkman & Jongeling, Dynamic behaviour of hydraulic structures part B, 2007)

The equation of motion to describe a single degree of freedom system.

$$m\frac{d^2x}{dt^2} + c\frac{dx}{dt} + kx = F(t)$$

3.1

In this equation, x is defined as the displacement in the horizontal direction, m is the mass, c the damping k as stiffness, F as the external force and 't' is time. For the discharge sluice gates, the entire mass of the gate is represented by the single mass (m) in this model. To calculate the DAF, the natural frequency of this SDOF system must be found. This is easily done, using Equation 3.1, without the presence of damping, see 4.5.1 for more information. However, the engineering practice usually applies a finite element method containing the model of the structure to find the natural frequency to avoid calculating a representative stiffness of the structure.
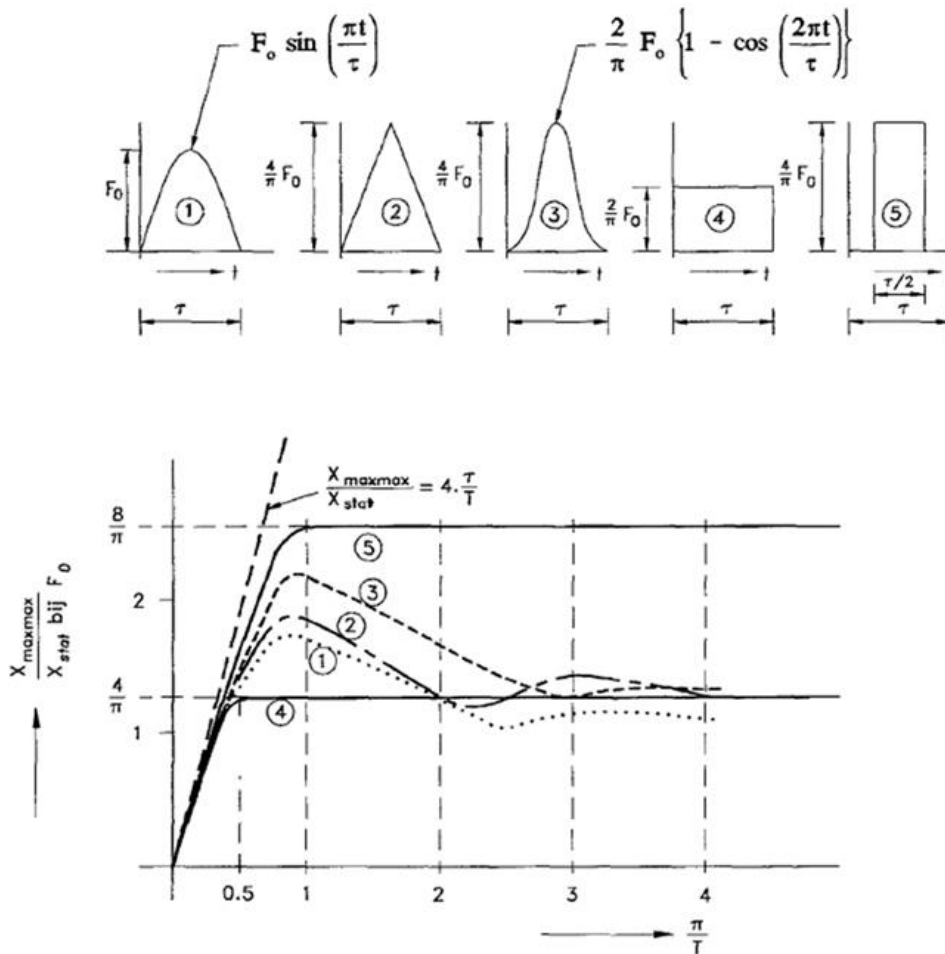
Figure 29. Normalized maximum response for different representations of a load (Kolkman & Jongeling, Dynamic behaviour of hydraulic structures part B, 2007).

Without the presence of damping, the maximum response of the structure can be determined when chosen a simplified representation of the loading, see Figure 29. The DAF is a dimensionless number which describes added dynamic effect by dividing the maximum response of the SDOF system over the static situation, see the y-axis. The x-axis of the figure shows the natural period of the load over the natural period of the structure, based on its natural frequency. For the case of a wave impact, the symmetrical triangular shape (2) is the most accurate, as can also be seen in example in Figure 30. The calculation method is elaborated in Appendix C, where the effect of the shape is also shown. The length of this triangular load is equal to the period of the load and will be used in the calculation

of the DAF. The DAF is therefore very sensitive to the design conditions and the mass of the structure. In the next section it is explained how these were dealt in the design by Levvel.
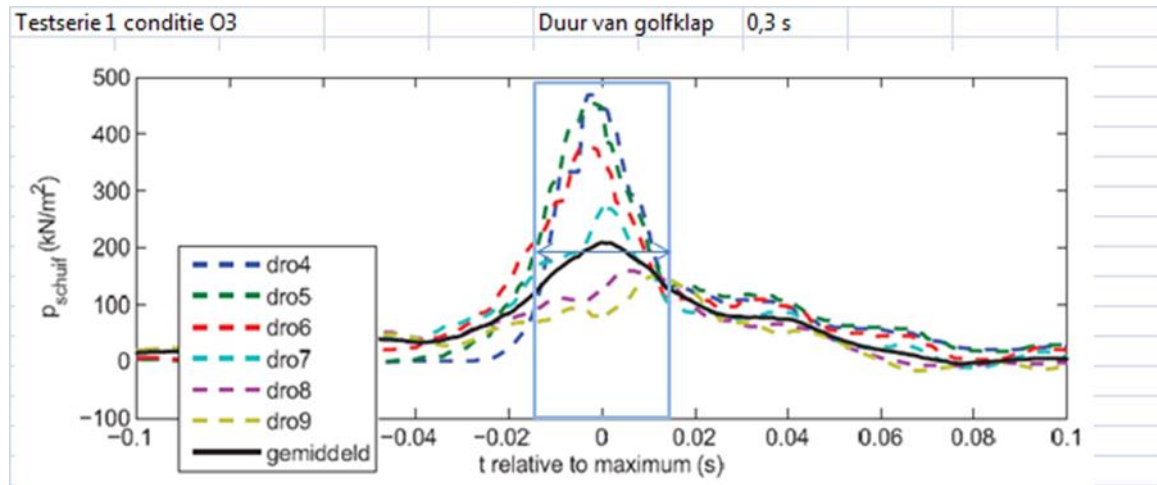
Figure 30. Time signal of the representative wave for the northern gate during the model test (duration of wave impact is 0.3 [sec]) (Hofland, 2015).

3.2 Application of Kolkman by Levvel

Because of the design at the Afsluitdijk, which contained an overhanging structure, it was not possible to determine an accurate design load in a preliminary design phase. The only available method is to perform a model test with the expected design conditions. Such a model test was executed by Deltares under the supervision of Hofland (2015), which is further explained in 4.2. The idea of a model test is to analyze the force of the loading under the expected design conditions. The results of these tests see Figure 30, mainly the time length of the impact based upon 2000 waves form the base of the design condition of the gates.
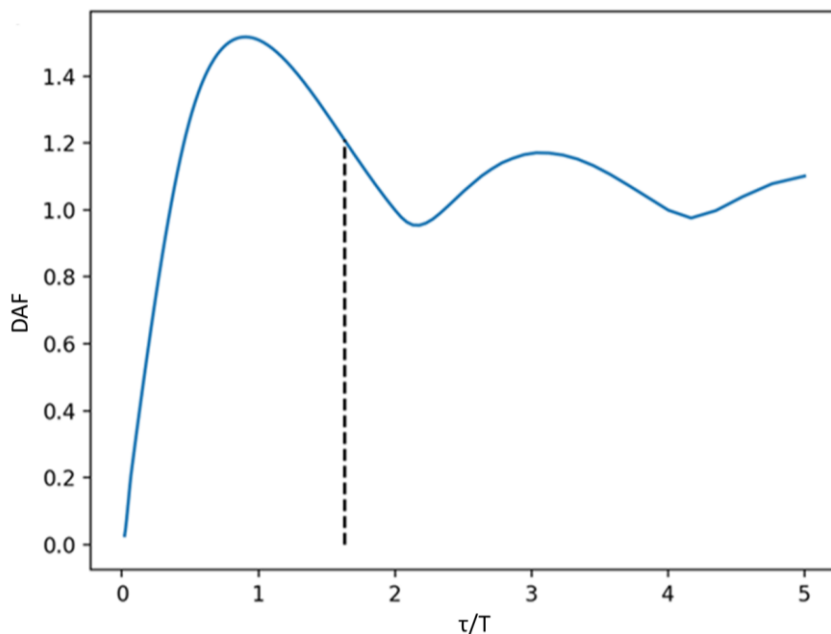
Figure 31. Response of the SDOF without damping due to a symmetrical triangular load and showing the DAF of the in-vacuo design by Levvel.

The natural frequency of the gate in-vacuo is found with a finite element method (SCIA Engineer). The gate design by Levvel from Chapter 2 has an in-vacuo natural frequency of 20.29 Hz. Using a symmetrical triangular shaped representative load derived from the model tests, the maximum

response was calculated, see Figure 31. The x-axis shows the period of the design load over the first natural period of the structure.

In order to increase the accuracy of this simplified method, damping and hydrodynamic mass are introduced. First the damping, which can originate from three regions: The steel itself causes some structural damping; The water within the supports act as a cushion and possibly damp the displacement in some way; At last the support itself will consist of a guiding system with some type of rubber attached to it that will be compressed between the gate and the support during an impact of a wave. Together these three are expected by Levvel to result in at least 2 per cent of damping. The movement of the tower or structure surrounding the gates, which could possibly add to the damping is neglected as these structures are more than 80 times heavier than the gate. The same holds for the subsoil below the bottom slab. Secondly during the impact of a wave, the surrounding water will also be displaced in correspondence with the gate. This volume of water has a certain mass, called a hydrodynamic or added water mass, and contributes to the determination of the natural frequency of the SDOF system. The hydrodynamic mass can be calculated using a method explained in Kolkman (2007 B). This method is based upon a two-dimensional calculation of the added water mass, which considers the wave radiation for a horizontally vibrating gate with water on one side. The bottom section of the gate will vibrate horizontally, and this method allows to decide how large that bottom part should be all the way up to a completely vibrating gate as is the case for the Afsluitdijk.

$$m_w = C_l \cdot \rho d^2 \qquad\qquad 3.2$$

$$\Psi = \omega^2 \cdot h/g = (2\pi \cdot 20)^2 \cdot 7.3/9.81 = 11751 > 100 \qquad\qquad 3.3$$

Equation 3.2 shows how to calculate the hydrodynamic mass according to Kolkman. Only the coefficient C_l needs to be determined, which can be done using Figure 32 and Equation 3.3. Figure 32 also shows that Ψ will stay on the same line for the Afsluitdijk and will only differ when the natural structural frequency falls below 2.5 Hz. The gates in the Afsluitdijk will vibrate in their entirity resulting in an h/d of 1. The coefficient C_l is hereby equal to 0.6.
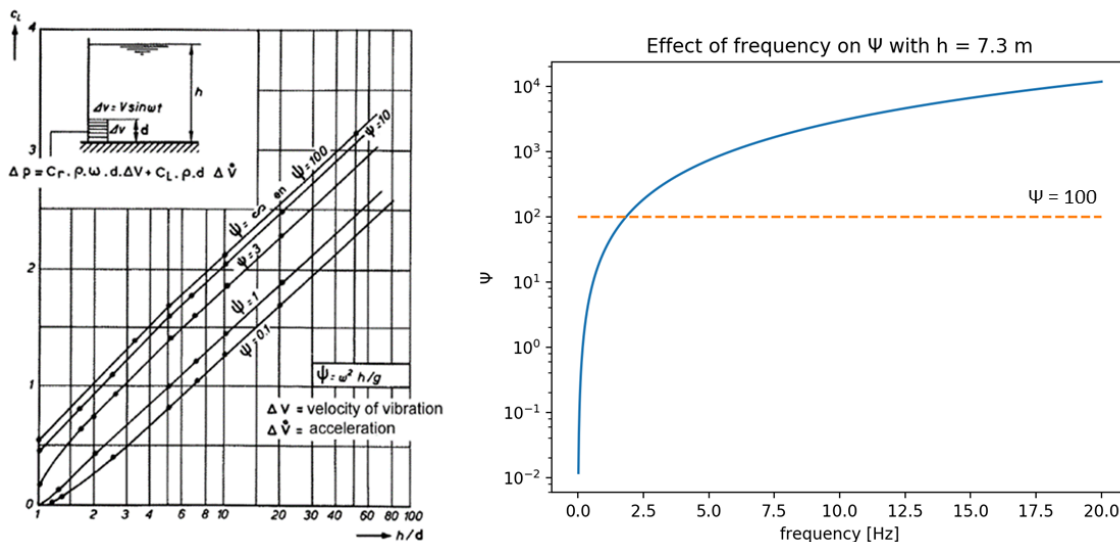
Figure 32. Left: Coefficient C_L compared to h/d (BOOK: Dynamic behavior of hydraulic structures). Right: Effect of the natural frequency of the structure on Ψ with a constant h.

To find the immersed frequency of the gate, Equation 3.4 is used. The mass of the structure is determined by the volume and density of the material used in the design. The added water mass is

calculated with Equation 3.2 with d = 7.3 and 3.29 for both sides of the gate during the design conditions, see Appendix B. Finally, the in-vacuo frequency was known from the modal analysis in a Finite Element Method.

$$f_{immersed} = \frac{f_{in-vacuo}}{\sqrt{\frac{(m + m_w)}{m}}} = \frac{20.29}{\sqrt{\frac{(36 + 505)}{36}}} = 5.23 \, [Hz] \tag{3.4}$$
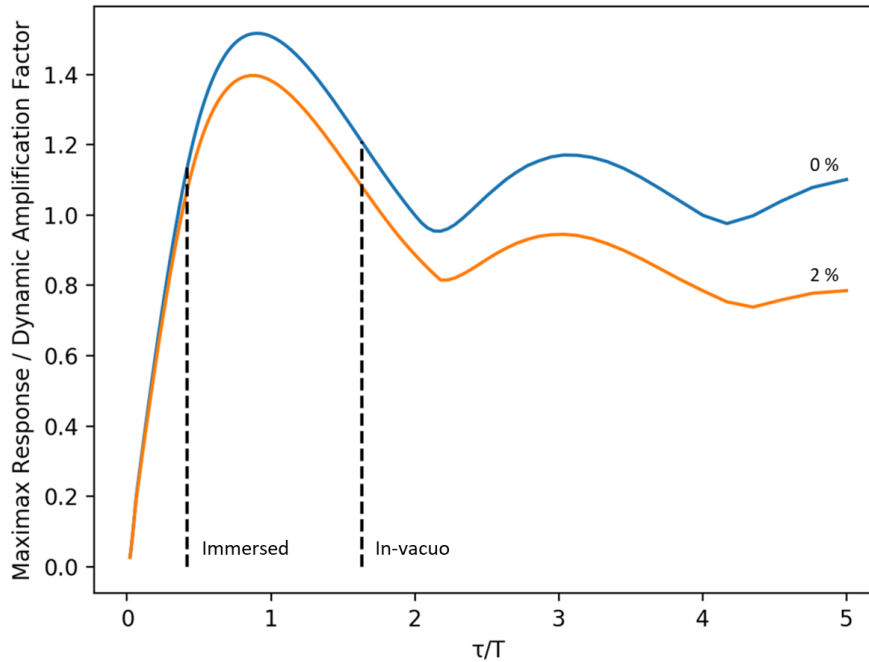
Figure 33. Response of the SDOF without and with (2%) damping due to a symmetrical triangular load and showing the DAF of the in-vacuo and immersed design by Levvel.

Applying the damping and the hydrodynamic mass will result in a shift of the DAF for the structure, see Figure 33. The resulting factor is lower than before the application of those two components, see Table 1. The shift passes the maximum, which raises the idea that an error in calculation or assumption can increase the factor significantly. The sensitivity of the method is therefore analyzed in the conclusion of this chapter, see 3.4.

Table 1. Parameters and results of the northern gate designed by Levvel required for the application of Kolkman's method.

Structure	Frequency [Hz]	τ / T [-]	Damping [%]	DAF [-]
In-vacuo	20.29	1.63	0	1.21
Immersed	5.23	0.42	0	1.13
In-vacuo	20.29	1.63	2	1.08
Immersed	5.23	0.42	2	1.07

3.3 Separation of DAF-variables

Previous sections show the quasi-static approach applied when encountering such a dynamic highly impulsive wave impact. The approach has its limitations in the assumptions of a simplistic SDOF system. It was found that the variables 'τ' (period of the load/wave) and 'T' (first natural period of the structure) are of great importance to the Dynamic Amplification Factor (DAF). Small deviations could lead to a significant increase of the DAF, resulting in a conservative approach to the method. An improvement is suggested by creating a 'DAF'-map, allowing the engineer to quickly see what

DAF can be expected for a certain hydrodynamic environment. This 'DAF'-map separates the variables 'τ' and 'T', see Figure 34. Figure 34 consists of two figures, which are both identical in use but have different scales where the right one is on a log-scale.
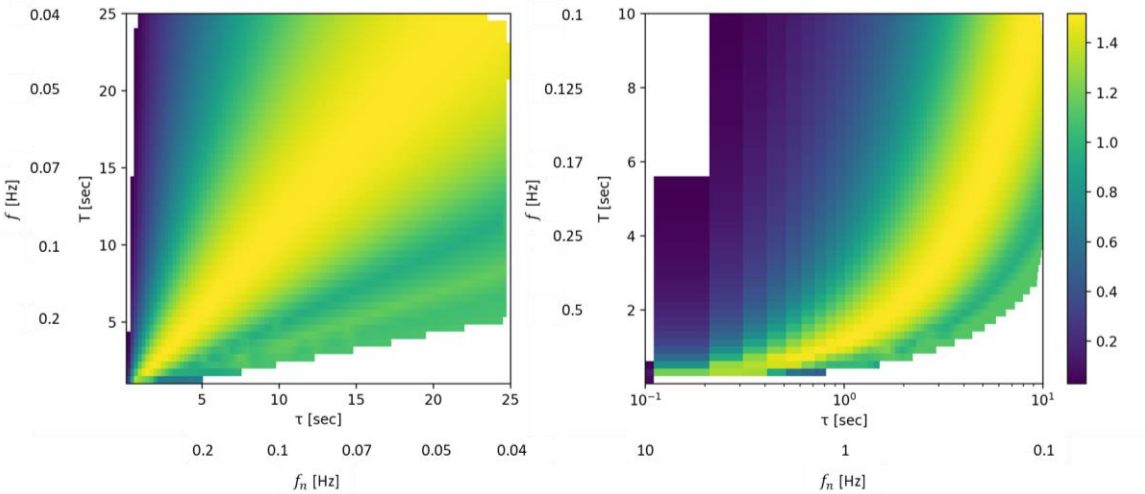
Figure 34. DAF map with separated variables τ and T with and logarithmic x-axis on the right.

This map can be used by placing a wave spectrum, which relates to the design conditions, perpendicular to the expected natural period or frequency of the structure. This way it quickly shows the response of such a structure to particular waves (long or short).
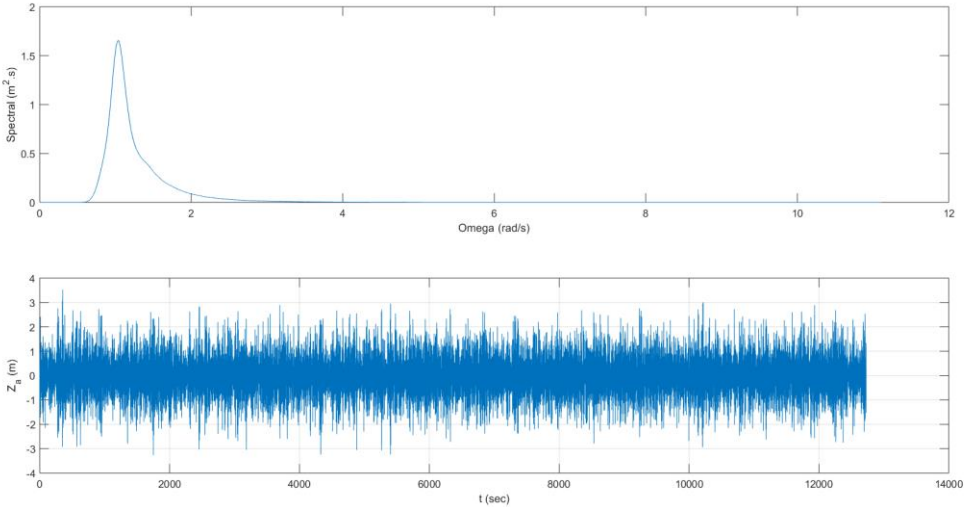
Figure 35. Wave spectrum (top) created from random storm signal (bottom) with input from Hofland (2015)
(Hs = 2.08 [m], Tp = 4.55 [sec]).

Using the wave spectrum from Figure 35, an example of the implementation of this map is shown in Figure 36. The blue lines represent the dynamic amplification of the in-vacuo (normal line) and immersed (dotted line) gates at Den Oever. When inserting the wave spectrum (calculated from the data (Hofland, 2015)) the spectrum is nowhere near the maximum amplification and that 1 can be assumed. However, the design condition, which is from the same dataset, is right in between the maximum amplification of both gates. The reason is that the design condition is at the gate and is a short impulsive force caused by the overhanging structure. This could be generally applied, when

understanding the translation between the offshore wave spectrum and the onshore impulsive spectrum.
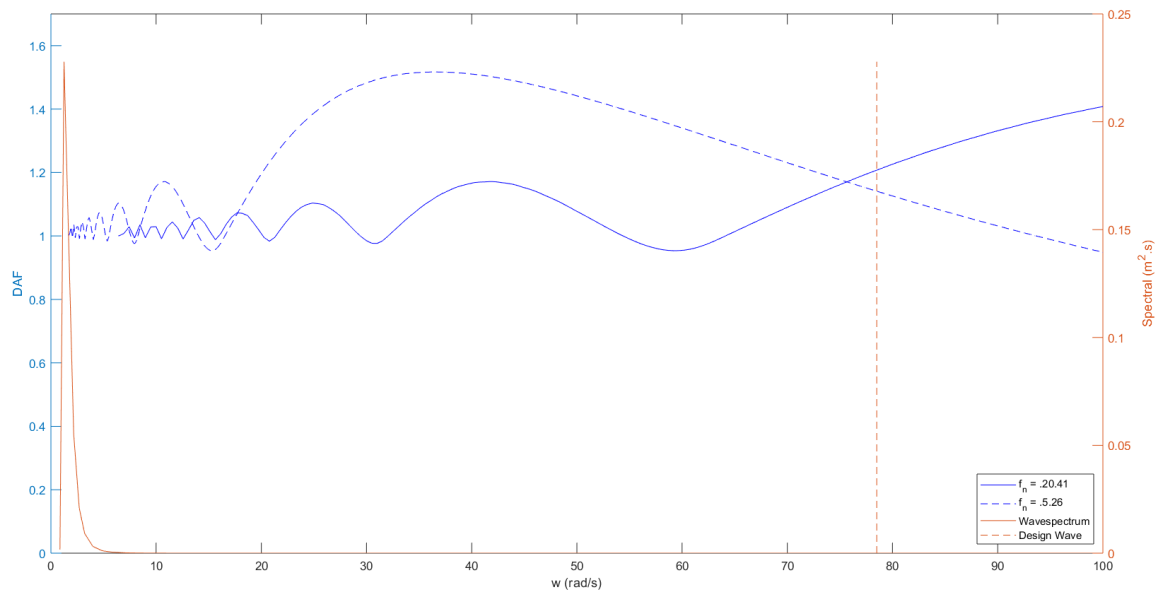
Figure 36. Implementation of the 'DAF'-map with the wave spectrum from Hofland (2015) together with the design wave condition versus the dynamic amplification of the in-vacuo (20.29) and immersed (5.26) gate.

3.4 Conclusion

The many uncertainties of this approach lead to an unknown probability of safety of this approach. The shift seen in Figure 33 together with the simplifications lead to a conservative approach. In this approach the maximum possible amplification factor is taken for all load scenarios. This has been made visible in Figure 37 for the situation with and without damping.
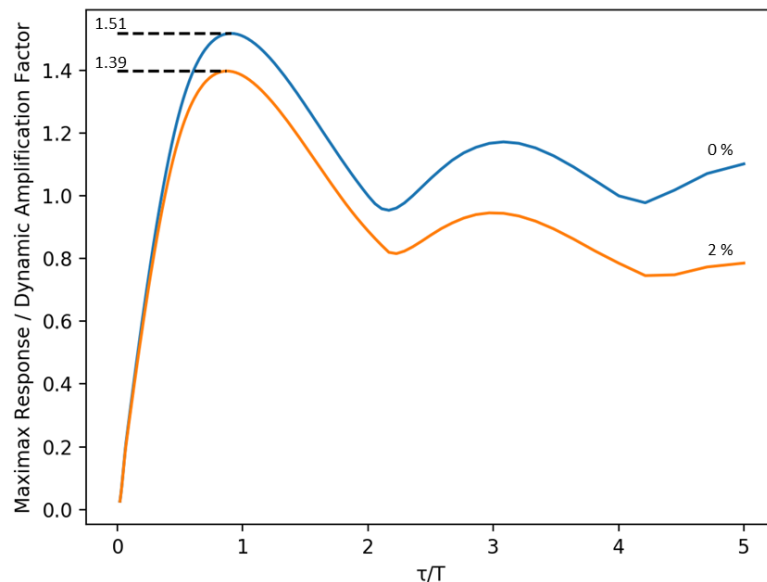
Figure 37. Maximum dynamic amplification factor of the situation with (2 %) and without damping.

The conservative solution of this method is applied in many load conditions making it even more conservative. It is believed that this approach does not need to be as conservative and can be more refined than its current state. The effect of the wave loading is now only applied to the design

conditions while the effect of the period of such a design wave is a major contributor to the DAF. In the discussion, Chapter 8.1.2, the effect of both variables has been made visual in a useable map.

Furthermore, the sensitivity of the hydrodynamic mass and damping are exposed in Figure 38 and Figure 39. The hydrodynamic mass has been calculated with a few assumptions and should therefore be analysed. Figure 38 shows that the effect is relatively low, however when applied to a different case the figure could look somewhat different. Appendix D gives other methods of calculation of this hydrodynamic mass containing different assumptions that provide a better understanding. Also showing another method from Westergaard resulting in a total hydrodynamic mass of 601 ton.
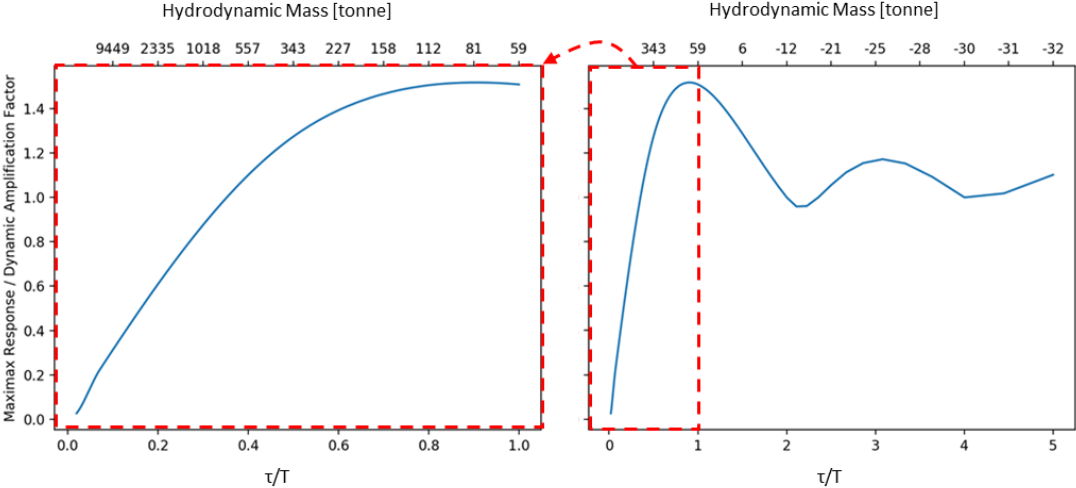
Figure 38. Effect of hydrodynamic mass (Equation 3.2) with in-vacuo frequency of 20.29 Hz to dynamic amplification factor.

The effect of damping has a relatively large influence on the DAF, as can be seen in Figure 39, compared to the hydrodynamic mass. The amount of damping that can be applied in such a complex case is however difficult to determine and should be dealt with care. Possibly more damping than 2 % can be enforced, but while little is known about the intersection of the different origins of damping, a conservative approach should be applied.
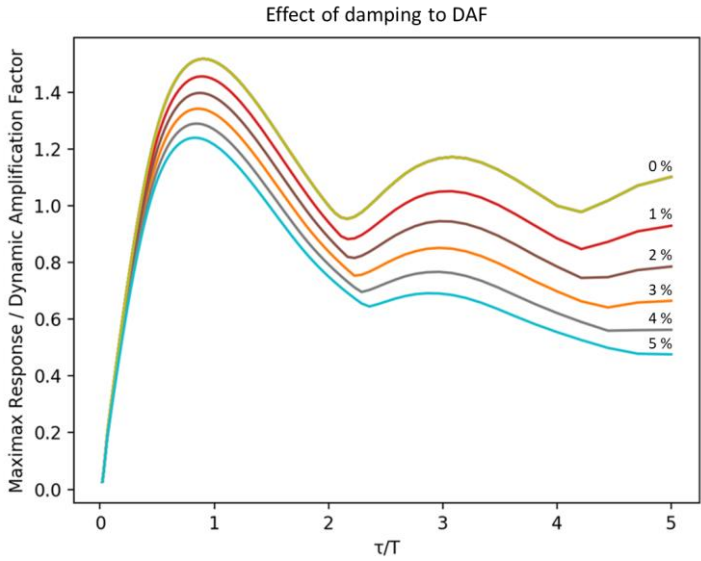
Figure 39. Effect of damping to dynamic amplification factor from 0 to 5 %.

Even though the Kolkman approach is applied, the design is altered to mitigate the possible problems. The uncertainties are too great, and the effect can have a large impact to its lifetime. Suggestions

made in this section are a good consideration, but Levvel made some other modifications. Namely it is better to avoid a load if possible than to overdesign in order to be more confident in its safety. The applied modifications are lowering of the height of the gate and leaving a horizontal gap between the gate and the bottom of the concrete road deck as seen in Chapter 2. Both these modifications are designed to avoid the amplification of the wave impact, thereby lowering the design conditions and lowering the design load theoretically. It is not known what the effect of these modifications have to the lowering of the wave pressure at certain design conditions, but will be investigated with the use of a numerical approach in Chapter 5. The result of Kolkman's quasi-static method will be used in comparison with the proposed model from Chapter 6.

4 Theoretical Background

This chapter contains some theoretical information that is used in the research. Some information is already mentioned in the corresponding chapters and will not be repeated. This chapter functions as an extension of the theory discussed in other chapters and double as a literature study to give the research context.

4.1 Wave Theory

The governing load at the gates of the discharge sluice complexes is caused by waves. As explained in Chapter 1, the Afsluitdijk is situated in between two large bodies of water. The Waddenzee at the northern side and the IJsselmeer at the southern side. Both bodies of water are not able to produce swell waves. Swell waves are present at the Noordzee, but these will be diffracted by the Wadden islands when reaching the Waddenzee. Thus, are considered unnoticeable. This means that the main wave loading onto the Afsluitdijk is caused by wind waves. The random wind-induced pressures cause a flat body of water to move up and down. This process is further enhanced by the air pressure of the wind moving in the same direction as the wave, which is schematically visualized in Figure 40.
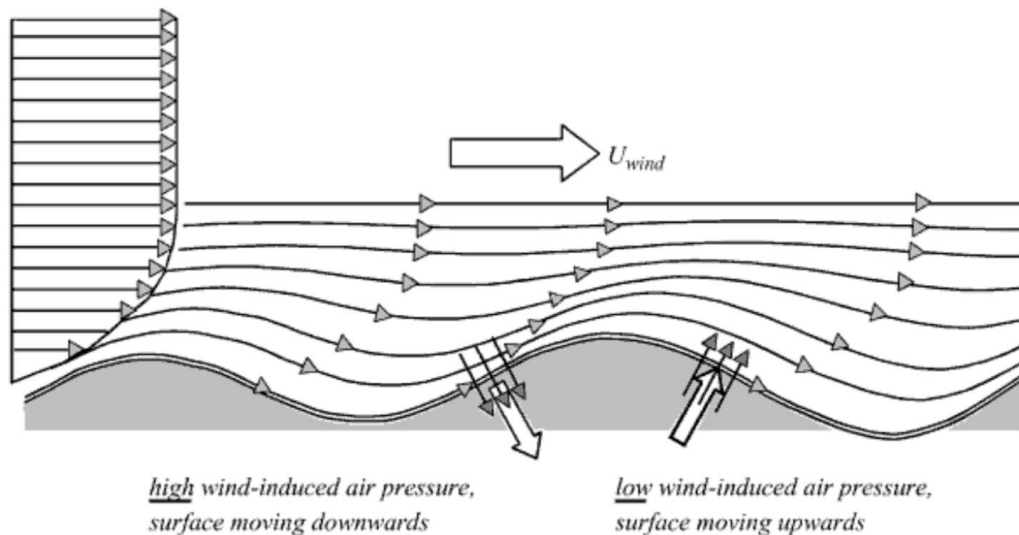
Figure 40. Airflow over the already altered surface with related pressures (ref: Holthuijsen)

The Waddenzee is still in contact with the North Sea and therefore influenced by the tidal wave. The IJsselmeer does not experience any tidal effect but is influenced by the discharge of the connecting rivers. This results in a lower water level in Winter. Finally, both sides also experience a water level set up during a storm, however these can be many times larger in the Waddenzee than in the IJsselmeer.
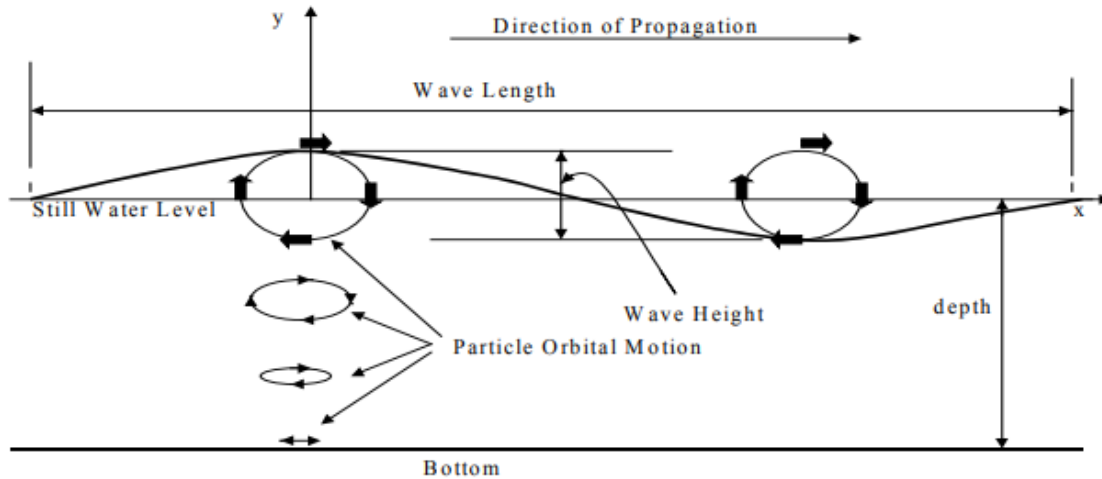
Figure 41. Definitions for linear wave theory.

When the waves have been formed, they propagate by the rules of linear wave theory. The main definitions of this theory are shown in Figure 41. The linear wave theory is a solution of the Laplace equation, see Equation 4.1 for a two-dimensional domain. With the use of boundary conditions, such as the bottom and free surface, the particular flow of any situation can be determined. Some simplifications can be used when the water body of interest is deep (d/L > 0.5) or shallow (d/L < 0.04). The complete equations and derivations will not be shown in this report as they are part of the prerequisite of the subject. However, it is interesting to show the horizontal and vertical velocities that can be derived of the Laplace equation for irrotational flow, see Equation 4.2 and 4.3. This can be needed for input of the calculation of wave pressures at the gate.

$$\frac{\delta^2\varphi}{\delta x^2} + \frac{\delta^2\varphi}{\delta y^2} = 0 \qquad\qquad 4.1$$

$$u = \left(\frac{\pi H}{T}\right) \cdot \frac{\cosh(\frac{2\pi(y+d)}{L})}{\sinh(\frac{2\pi d}{L})} \cdot \cos(2\pi\left(\frac{x}{L} - \frac{t}{T}\right)) \qquad\qquad 4.2$$

$$v = \left(\frac{\pi H}{T}\right) \cdot \frac{\sinh(\frac{2\pi(y+d)}{L})}{\sinh(\frac{2\pi d}{L})} \cdot \sin(2\pi\left(\frac{x}{L} - \frac{t}{T}\right)) \qquad\qquad 4.3$$

The wind waves travel freely over the body of water until they impact on the gates of the discharge sluice. This report concentrates on extreme pressures focused on the steel gates, causing a dynamic response. These pressures can be reached in two situations. Firstly, waves can break under certain special conditions when an erosion hole is assumed in front of the structure. This is important, because a breaking wave causes a different and more violent type of impact than a non-breaking wave. When waves break non-linearity will start to play a role and the linear wave theory does not hold anymore. Another reason for high pressures due to waves are partially enclosed systems. This is found at the Afsluitdijk as a defense beam is in front of the gate closing the system vertically. This results in extreme pressures at the gate, which was explained in Chapter A.2.3 and has been researched in two occasions. These two studies and their findings are interpreted in the following section.
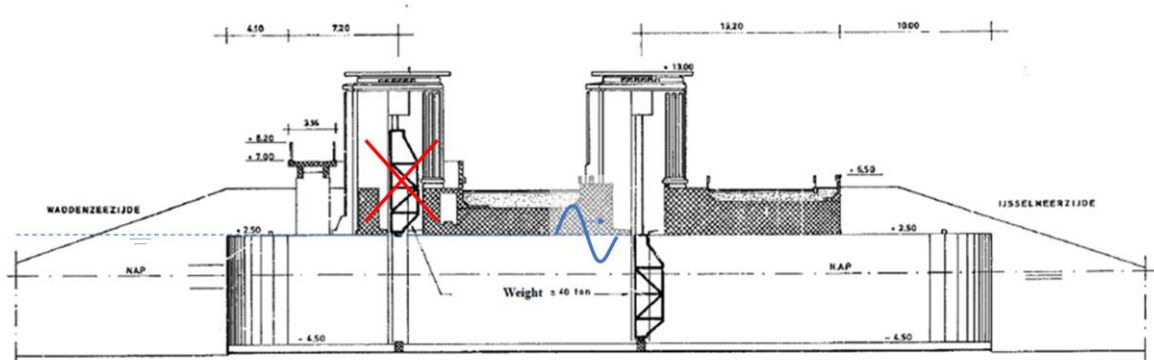
Figure 42. Cross-section of Discharge Sluice, where northern gate malfunctions in governing load situation.

The new design as explained in Chapter 2 will remove this defense beam, thus removing the problem. Nevertheless, the highway will remain in place. In a situation that the northern gate would not function the highway would function in the same manner as the defense beam before. Peregrine worked on the subject in a theoretical way and his papers are summarized in the last section of this chapter.

The difficulty of modelling wave impacts is the large variability of pressures measured in even identical situations. However, Bagnold (1939) found that the pressure impulse is a more consistent measure of a wave impact and can be used to reproduce a realistic scenario, see the definition of the pressure impulse in Equation 4.4. The subscript b stands for before the impact of the wave and subscript a after the impact. These findings of Bagnold are the foundation of the research done by the following researchers in this chapter.

$$P(x) = \int_{t_b}^{t_a} p(x,t)dt \qquad\qquad 4.4$$

4.2   Defense Beam Studies

Hofste [8] and Hofland [7] both worked on the loading of waves onto the Stevinsluizen. Hofste focused his research on the defense beam and what type of impact load could be expected in a governing load situation. This governing situation being a storm with a water level at exactly NAP + 2.50 m, which is at the same level as the bottom of the defense beam, see Figure 43.
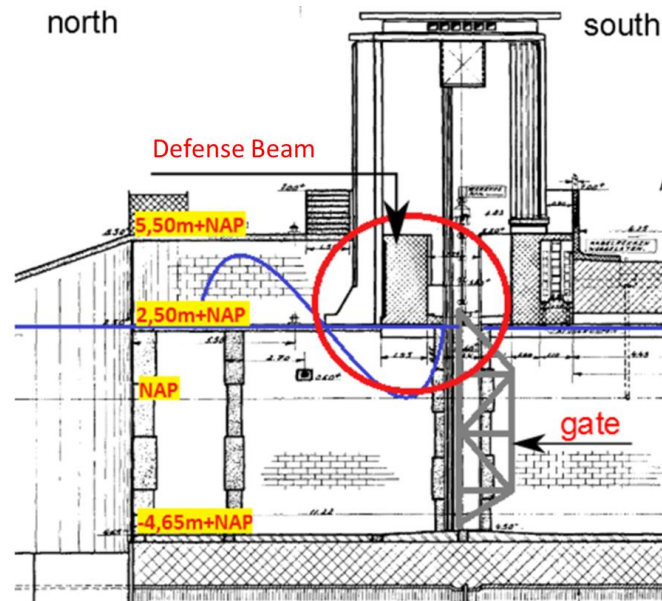
Figure 43. Governing load situation for the defense beam at the Stevinsluizen at Den Oever (Hofste, 2012).

Hofste did numerical and physical modelling to find his answers. For numerical modelling the program ComFLOW was used, which makes use of the incompressible Navier-Stokes equations. The size of the grid cells and chosen time step determined the results of the wave impact. No point of convergence of the pressure peak to the grid cells was found and the best results came with the price of long computation times. For the physical modelling a small-scale test set-up (1:15) was made in the laboratory. The shortest wave tested (full scale period of 3.9 s) at the governing water level created a maximum force measured at $35H_i$ on the beam. Meaning 35 times the $\rho g H_i$, where H_i is the wave height of the incoming wave.

Hofland did only physical modelling and besides the effect of the defense beam also looked at the effect of the bicycle bridge and the amount of overtopping during design conditions. The small-scale test set-up had a geometric scaling factor of 16. The largest force measured by Hofland was around $32H_i$, which is comparable with the measurements of Hofste. Although his result was reached with the water level at a lower height of NAP + 2.00. Hofland also tested the scenario where only the southern gate would be closed, and waves would impact from the Waddenzee. The results of this scenario gave forces about 4.5 times lower than with the northern gate.

The reason the lowest water level caused the largest measured force in the test of Hofland is because a robustness of 0.1 m was added to the NAP + 2.5 m test. This robustness is normally needed due to the uncertainties caused by interpolation errors in the basic levels. However, the test was done in order to find a worst-case scenario, which is expected to be at the bottom of the beam or lower. The addition of the robustness results in a water level that is higher than the expected worst-case scenario resulting in the fact that the lowest scenario at NAP + 2.0 m creates the largest response. Furthermore, the lowest scenario follows the exact same wave conditions as the scenario with a water level at NAP + 2.5 m. The calculation for this lowest water level was not executed in the model and results in an overestimation of the actual wave conditions at NAP + 2.0 m.

4.3   Air Entrapment

When waves break and crash into a structure, air can be trapped between the water and the structure. This air pocket can dampen the impact pressure as it distributes the load over the area of the air pocket. Larger air pockets lead to more damping of the pressure. If the compressibility of the fluid becomes import, then the addition of air pockets will increase the complexity of the problem. This is since the quantity, size and distribution of the air bubbles are difficult to determine and predict.
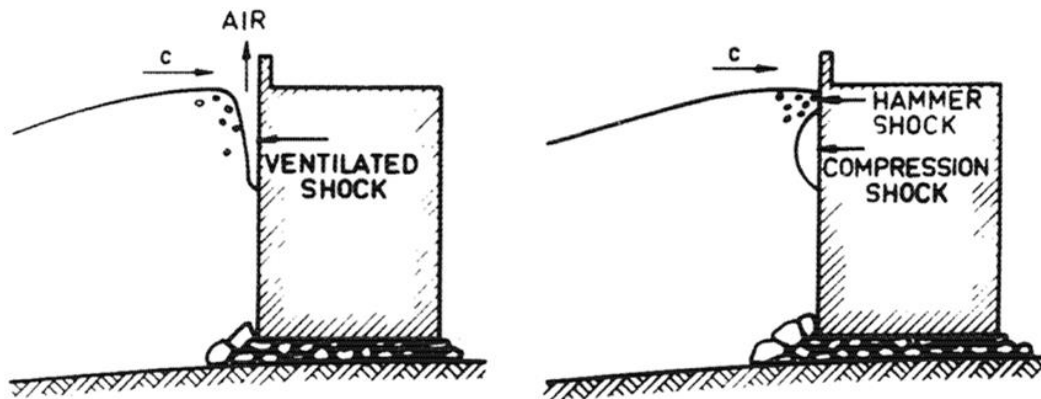
Figure 44. Shock wave phenomena (Lundgren).

Various types of waves result in different impacts on structures. These different impacts can cause more or less air pockets to arise, which can give a more or less violent impact. Figure 44 shows with a basic schematization, these differences. It should be mentioned that the word shock is a strange application of the word, because there is no evidence associated with shock waves of compression in the fluid, which is what the word by definition describes.

4.4   Dynamics (Response)

The response of this problem can be subdivided into three main parts. First, the response is dynamic, which means it is affected by inertial forces. The system will have to be simplified to be able to analyze the problem of interest. The three parts which will be discussed in this chapter respectively are the structure, the fluid and the interaction between both. The structure in this case is the lifting gate in the discharge sluices. The fluid are the water bodies on either side of the gate.

4.5   Structural Dynamics

As mentioned, fluid-structure interaction will be a main topic of this report. This section of the report will be focused on the dynamics of the structure without any fluid. The dynamic behavior of a structure is analyzed using the equation of motion, which can be derived by applying two methods; The displacement method and the lagrangian method.

The displacement method

The displacement method prescribes the displacement in all degree of freedoms to achieve the result of the acting forces. To reach the complete equation of motion Newton's second law is applied for each degree of freedom respectively.

$$m_i(x_i) = \sum F(x_i, \dot{x}_i, \ddot{x}_i, x_i', x_i'' \dots) \qquad\qquad 4.5$$

Where,

m$_i$ =   The lumped mass for a degree of freedom equal to i
F   =   The force in the system
$\ddot{x}_i$ =   The lumped mass acceleration for a degree of freedom equal to i

The Lagrangian method

The Lagrangian method places Newton's second law into a solution that is particularly suitable for complex coordinate systems. The equation is based on the conservation of energy, which governs the motion of particles and rigid bodies.

$$L_x\big(t, q(t), \dot{q}(t)\big) - \frac{d}{dt} L_v\big(t, q(t), \dot{q}(t)\big) = 0 \qquad 4.6$$

Where,

L_x, Lv = The partial derivatives of L with respect to the second and third arguments

L = (K - P) The Lagrangian function

K = The total kinetic energy

P = The total potential energy

4.5.1   Single Degree of Freedom System

In the previous chapter, the basics of a SDOF system were explained. This section will continue with the explanation of some characteristics deemed interesting for dynamic analysis.

Natural frequency

In absence of the damping force the natural frequency of the vibrating system can be easily found. The classic equation to do so is changes into the following.

$$m \frac{d^2y}{dt^2} + ky = 0 \qquad 4.7$$

Which results in a harmonic vibration, where Y defines the amplitude of the vibration.

$$y = Y \sin(\omega t) \qquad 4.8$$

Using the preconditions that F = 0 and c = 0, the equation immediately results in the value of the angular frequency ω and consequently of the frequency f_n.

$$f_n = \frac{\omega_n}{2\pi} = \frac{1}{2\pi}\sqrt{\frac{k}{m}} \qquad 4.9$$

The natural frequency is important for dynamic analysis. The reason is that if a system is exercised by a force that oscillates at the natural frequency of the system a greater amplitude than at other frequencies is experienced.

Dimensionless damping

The relation between the damping and the critical damping is called the dimensionless damping, represented by y. In case of increased damping, and in case of free vibration, not only the amplitude decreases faster over time, but also the frequency of the vibration decreases. In case of critical damping the frequency has become zero, and in case of a free vibration the deflection relative to the zero position is reduced over time, but thus not change sign. The dimensionless damping in a single degree of freedom system is equal to the following. (derivation of equation found in Kolkman part C chapter 3).

$$\gamma = \frac{c}{2\sqrt{km}} = \frac{c}{2m\omega_n} = \frac{c\omega_n}{2k}$$

4.10

Response characteristic in the frequency domain

In case of periodic oscillation, the amplitude of the internal force is represented by a factor A for amplification multiplied with the amplitude of the external force. A is a function of the relation of the excitation frequency, f, relative to the natural frequency, f_n. This results in the normalized response diagram. The phase diagram is also related to this. The phase angle, Φ, indicates how much the in-phase movement is behind the excitation.

$$F = \hat{F} \sin(\omega t)$$

4.11

Resulting in the fundamental solution for the movement.

$$y = Y \sin(\omega t - \varphi)$$

4.12

In case of resonance, where the damping is not too large, the resonance frequency approximates the natural frequency. The equilibrium amplitude that is reached follows from the condition that the residual forces together also cause an equilibrium. The amplitude of the external periodic force therefore equals the amplitude of the damping force.

$$Y = \frac{\hat{F}}{\omega c}$$

4.13
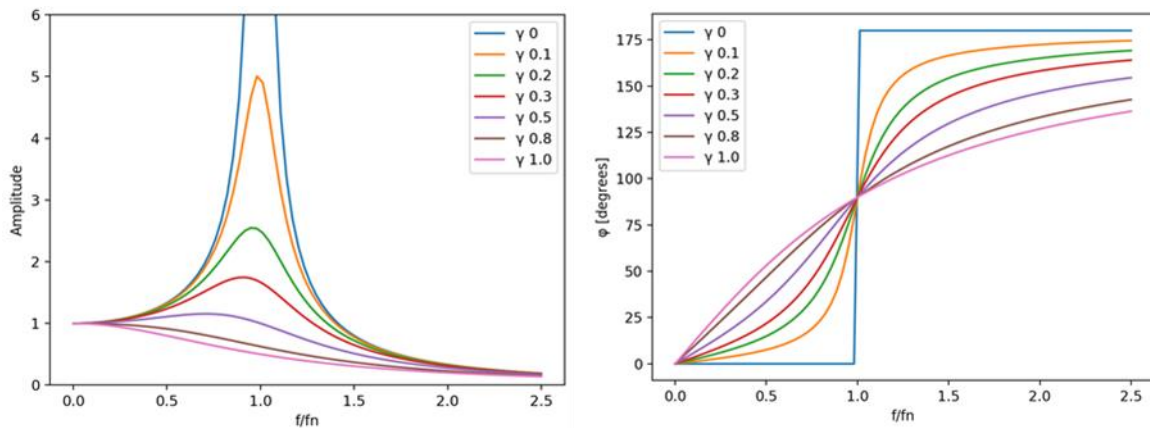
Figure 45. Response curve and phase diagram of a SDOF as a function of f/fn with different values for damping.

To analyze a dynamic behavior of a system, excited by a non-harmonic force, in the frequency domain, a Fourier transform can be applied. This can be done, because any time signal is a summation of harmonics. An inverse Fourier transform is used to go from the frequency domain back to the time domain if needed. The reason for the use of a frequency domain is based on mathematics. It is faster and easier to calculate in the frequency domain and also frequency dependency can be included, which is difficult in the time domain. The main limitation of the Fourier transform is that it can only be applied to linear systems, which is not the case if system is kept in the time domain.

The frequency domain describes the behavior of the system as amplitudes versus frequencies, whereas the time domain does it versus the real time. Analyzing in the frequency domain results in an operator, that expresses the response of the system for a certain frequency in the domain. There are methods that iterate between both domains and are called hybrid domain analysis. These

advanced methods contain the best of both worlds as they can include non-linearity and frequency dependency.

4.5.2   Multi Degree of Freedom System

A single mass can be expressed in all direction or it could also describe the movement of multiple masses in one direction. The general description is different to the classic equation of motion described in the previous section because it is now defined in matrices and vectors.

$$\underline{\underline{M}}\ddot{x} + \underline{\underline{C}}\dot{x} + \underline{\underline{K}}x = \underline{F} \qquad\qquad 4.14$$

Where,

$\underline{\underline{M}}$	=	The mass matrix
$\underline{\underline{C}}$	=	The damping matrix
$\underline{\underline{K}}$	=	The stiffness matrix
$\underline{F}$	=	The force vector
$\ddot{x}$	=	The acceleration vector
$\dot{x}$	=	The velocity vector
x	=	The displacement vector

Depending on the system, the equation of motion for each degree of freedom can be found. A common problem is that the damping matrix can be nondiagonal. This results in the fact that the equation of motion is coupled. To solve this one can either assume a diagonal matrix with a pragmatic approach or use more elegant approach like the Fourier or a rougher method like the Rayleigh method.

4.5.3   Continuous System

Instead of a discrete or lumped mass system, the continuous system distributes the mass over a line, plane or volume element. Such a system has infinite degrees of freedom and therefore results in an infinite amount of eigenmodes and natural frequencies. This method is more detailed than the discrete system.

4.5.4   Plate and Shell Analysis

The analysis of vibration in plates and shells dates to the 17th century. Robert Hooke, a famous English physicist, did an experiment in 1680, where he placed flour on a plate and ran a violin bow along the edge of the plate. The result was that neat symmetrical patterns emerged in the flour. About one-hundred years after Hooke, Ernst Chladni, a German physicist, repeated his experiment and found that patterns emerge when the resonance of the plate is reached and the flour flows to the areas where no vibration occurs, which are the nodes. These patterns are called Chladni-figures, because of his findings. Nowadays we can vibrate a plate at a precise frequency, and you can find many different interesting patterns. These patterns are created due to the fact that a structure has infinite modes, each having its own natural frequency. The shapes becoming increasingly complex when reaching higher frequencies as can be seen in Figure 46.

Figure 46. Example of a Chladni-figure on a rectangular plate (WEB: geek.com/news/chladni-plate-experiment-makes-for-a-jaw-dropping-video-1558421/).

Plates and shells can be considered as thin or thick structures. If the system is considered thin, Love's theory applies, and shear deformation and rotational inertia can be neglected. It is typically considered a thin-plated structure if the thickness to width ratio is less than 0.1. However, the thickness to wavelength ratio is also important, because for low frequencies the Lamb waves occur and for high frequencies Rayleigh waves. If the thickness is smaller than the wavelength than a Lamb wave will be observed. If the thickness of the plate is thicker the Mindlin-Reissner theory must be applied. This theory does account for shear deformation and rotational inertia.

4.6   Fluid Potential Flow

The domains on either side of the gate contain a body of water, which should be analyzed on its dynamic behavior. The liquid studied for this report will be sea- and freshwater, as the IJsselmeer is a freshwater lake and the Waddenzee is in direct contact with the oceans thus containing saltwater. The fluid potential flow can be used to describe fluid motion. Some assumptions must be made in order to derive the correct equations. These assumptions are based on the characteristics of the liquid and can simplify the derivations if applied. Analyzing the dynamic behavior in a filled tank, the liquid can be assumed as linear, inviscid and incompressible (Canny, 2018). Linear means that the rotational flow is neglected. An inviscid liquid assumes that the effect of viscosity is zero. Lastly, an incompressible fluid means that the density will remain the same in time. Using these three assumptions, the governing equation of motion reads as follows.

$$\frac{\partial^2 \varphi}{\partial x^2} + \frac{\partial^2 \varphi}{\partial y^2} + \frac{\partial^2 \varphi}{\partial z^2} = 0$$

4.15

The equation of motion can also be written in terms of pressure.

$$\frac{\partial^2 p}{\partial x^2} + \frac{\partial^2 p}{\partial y^2} + \frac{\partial^2 p}{\partial z^2} = 0$$

4.16

The frequency domain is important for the increase of a certain effect. Low frequencies (smaller than ≈1.27 [Hz]) will include surface waves and high frequencies (larger than ≈16.77 [Hz]) the effect of compressibility should be considered (Tieleman O. C., 2015). The transition region both effects can be neglected. When compressibility is required Equation 4.17 will have to be applied as the

governing equation and if the surface waves cannot be neglected the boundary condition at top boundary will have to resemble Equation 4.19.

$$\frac{\partial^2 \varphi}{\partial x^2} + \frac{\partial^2 \varphi}{\partial y^2} + \frac{\partial^2 \varphi}{\partial z^2} = \frac{1}{c_p^2} \frac{\delta^2 \varphi}{\delta t^2}$$

<div align="right">4.17</div>

Where,

$$c_p = \sqrt{\frac{K}{\rho_f}}$$

<div align="right">4.18</div>

$$\frac{\delta \varphi}{\delta z} = \frac{\omega^2}{g} \varphi$$

<div align="right">4.19</div>

4.7 Fluid-Structure Interaction

Fluid-structure interaction is a vast field, from small oscillations like vibro-acoustics to general problems of transient motion. The reason that it is important to model fluid-structure interaction accurately is mainly to predict the instability of coupled systems and to predict the performance of fluid-structure systems.

In fluids, such as liquids or gasses, displacements can be very large and are therefore viewed in a domain where particles can flow in and out. This is referred to as a Eularian representation, where the observer is fixed in an inertial reference. This is fundamentally different from the Lagrangian representation, which is used in solid mechanics where properties are considered for a given material point. However, it is possible to find a Lagrangian function for a certain property that has a Eulerian description. The transformation is shown in the following function.

$$a_{Lagrangian}(X, t) = a_{Eulerian}(x = X + u_{Lagrangian}(X, t), t)$$

<div align="right">4.20</div>

4.7.1 Numerical Method

The problem can also be solved using a numerical method. Numerical methods break down the problem in many small elements and solve the entire domain numerically, because some boundary conditions are known. Many types of numerical methods are available to solve these problems and Figure 47 shows which ones to use for a given situation. The Boundary Element Method (BEM) is highlighted in red, because it would be the best choice for this problem.
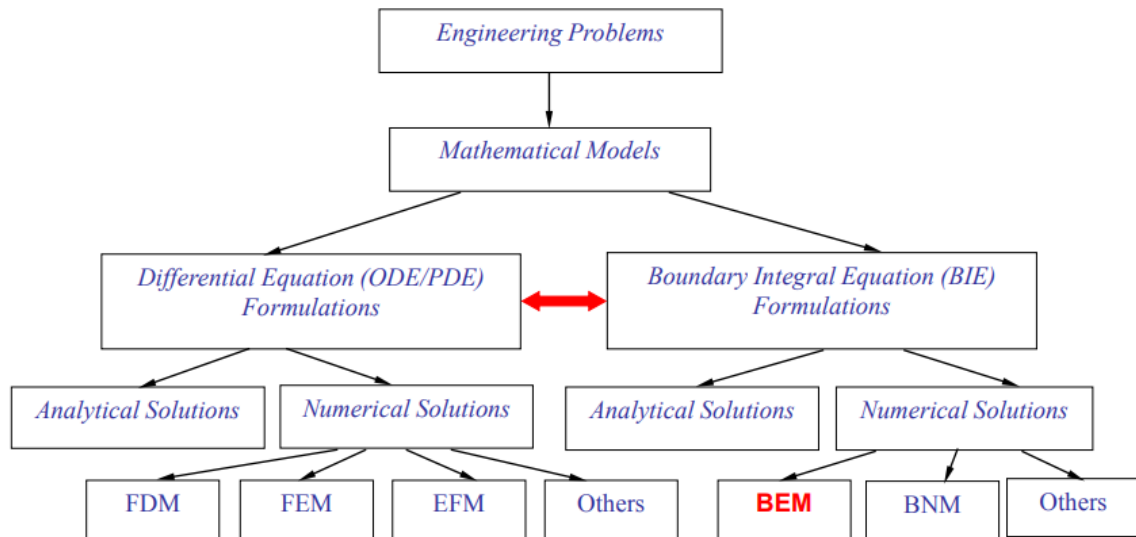
Figure 47. Main approaches to engineering problems focused on the numerical solutions.

Instead of many thousands of volume elements, which are needed for a Finite Element Method (FEM), a BEM only uses surface elements. It applies surface elements on a three-dimensional domain and line elements on a two-dimensional domain. The calculation time is therefore fast compared to other numerical methods and gives a similar result in many applications like infinite domain problems, stress concentration and thin shell-like structures.

4.8 Conclusion

The decision to remove the defense beam in the tower discharge sluices was made correctly, when looking at the amplified pressures that are the result of such structure in section 4.2. The reason that such a defense beam is redundant also has a large claim. The hydrodynamic boundaries of the gate are still determined with the defense beam in place even though it will be removed. Therefore, and for future purposes it is still interesting to see if another approach besides a model test can be utilized as alternative. The next Chapter 5 continues this subject.

Furthermore, it seems that a single degree of freedom system is a highly simplistic approach to such a complex dynamic problem as shown in Chapter 3. However, the mechanics of a relatively simple method makes it a good instrument for comparison as it is easier to grasp. Lastly the element used in the gate design are all thin plated and do not require the Mindlin-Reissner approach. Nevertheless, this can be easily applied when the FE-model is introduced into the method in Chapter 6.

5 Numerical Method for Wave Impact Pressures

To calculate the strength and response of a design with any method, first a correct design load for the wave impact must be found. However, as explained in section 3.2, this was rather difficult due to the overhanging structure in front of the design. To determine the design load for the Afsluitdijk, a model test had to be executed. These tests cost time and money, and if possible, should be avoided. This chapter contains a method that could potentially give a solution that would eliminate the procedure of a model test in future endeavors.

Peregrine has developed mathematical models to calculate pressures and sudden velocity changes when an incompressible fluid impacts a solid surface. He has done so for impact on a vertical wall (Cooker & Peregrine, 1995) and on a vertical with an overhang (Wood & Peregrine, 1996). The following sections will involve their findings focused on the scope of this report. Their research is used to develop a numerical method in order to calculate the wave impact pressures impulses on a vertical surface with an optional horizontal solid top boundary of finite length. This numerical method is described and verified in section 5.2.

5.1 Impact Vertical Wall with Addition of Cantilever (Wood & Peregrine)

Wood & Peregrine noticed, just like the results of (Hofste, 2012) and (Hofland, 2015) shows, that a sudden wave impact on a horizontal overhanging structure or cantilever leads to a rapid rise in pressures. The notion of (Wood & Peregrine, 1996) was to analyze the problem of a wave hitting upward under a deck jutting out from a wall as mathematically equivalent to a plate dropping onto a body of water and setting the water in motion. For the analysis of their mathematical formulation they neglected the viscosity and surface tension. Also, the compressibility of the fluid is neglected even though it might be important for a brief moment. Even for impact velocities well below the speed of sound, it is neglected. Next to the impact zone there is a small region where nonlinear terms are not negligible, see (Howison, Ockendon, & Wilson, 1991). However, the approach of the pressure impulse gives a good approximation, see (Wood & Peregrine, 1996).
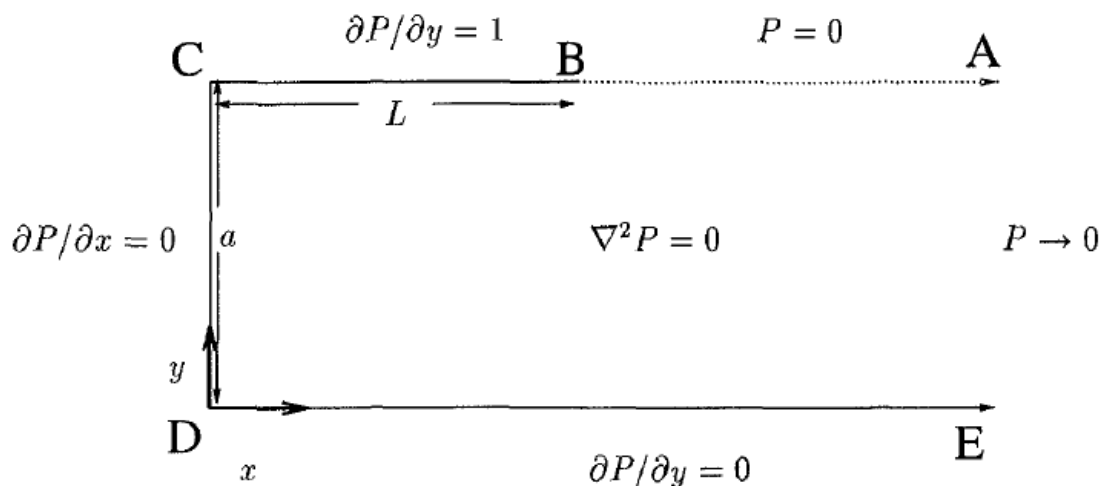
Figure 48. The schematic representation of the mathematical problem of Wood & Peregrine. Showing the height of the wall a and width of the deck L (Wood & Peregrine, 1996).

Figure 48 shows the approach of Wood & Peregrine to solving the pressure-impulse in the domain of interest. The pressure impulse as defined in Equation 4.4 has been made dimensionless by dividing P with $\rho U_0 H$, where U_0 equals the maximum vertical velocity at impact. Bagnold (1939) observed experimentally that the pressure-impulse is approximately constant even though the peak pressure

changes unpredictably between apparently identical wave impacts, making it a good variable for a wave impact model. The boundary conditions are shown, where it should be noted that on boundary BC the derivative is equal to 1, representing the horizontal plate or cantilever dropping into the body of water. Their paper shows a mathematical approach of solving the problem analytically based on the approximation that the equation of motion can be written as Equation 5.1. An assumption that allows this approximation is that the time interval of the wave impact, which the pressure-impulse is based on, is relatively short compared to the other timescales in the problem. During this short time the fluid-motion changes so rapidly that the equation of motion is valid. Also, the convective terms are neglected, which is consistent except in small regions near the impact where jets might form.

$$\frac{\delta u}{\delta t} = -\frac{1}{\rho}\nabla p \qquad\qquad 5.1$$

Integrating Equation 5.1 with respect to time through the short impact interval and use the definition for the pressure impulse from Equation 4.4 results in Equation 5.2. Taking the divergence of Equation 5.2, it is found that the pressure impulse satisfies Laplace's Equation, see Equation 5.3.

$$u_a - u_b = -\frac{1}{\rho}\nabla p \qquad\qquad 5.2$$

$$-\nabla^2 p = 0 \qquad\qquad 5.3$$

To solve the problem analytically Wood & Peregrine used mathematical tools such as conformal mapping that introduce complexity fairly quick when the domain of interest contains some geometrically inconsistencies.

5.2   Validation with Physical Test

To see if this theoretical model constructed by Wood & Peregrine (1996) can be used with acceptable accuracy it needs to be compared with real situations. The mathematical method is compared with a physical model test. The test from Hofland (2015) is used, which is a scale model test of wave impact at the gates at Den Oever and Kornwerderzand also including the overhanging defense beam, which is now part of the hydraulic boundary conditions for the gates of the discharge sluices in the Afsluitdijk. In order to compare the results, the mathematical method must be replicated, however the analytical method explained in Wood & Peregrine (1996) is complex and not easily adapted. Therefore, a numerical method in Python was created that can replicate Peregrine's schematization. The numerical method has been verified with the analytical solution, which is presented in Appendix E for the numerical scheme and Appendix F for the complete validation. Figure 49 shows one of the results of the numerical representation when replicating the same input found in the paper. The results are very similar which allows for the continuation of the comparison between the model test and the numerical method based on Peregrine's notion.
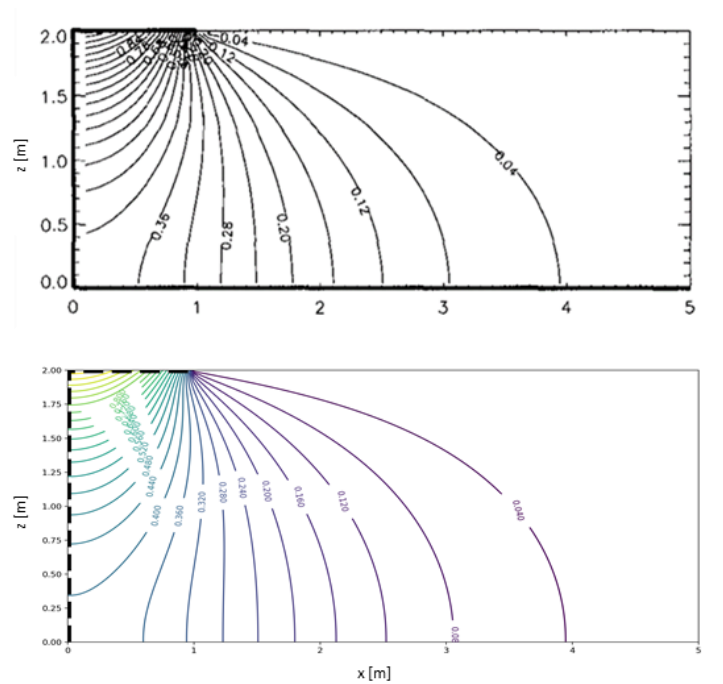
Figure 49. Analytical (top, from: Wood & Peregrine (1996)) and numerical (bottom) solutions with a = 2 (length cantilever over height water column).

The physical tests were executed for multiple situations for both the Southern and Northern gates. For the validation of the mathematical model only the tests of the Northern gate were used as they have the direct influence of the defense beam. In Figure 50 the model set up for the Northern gate is schematized. The interest is only in the effect on the gate, leaving out the results of the three sensors in the bridge deck. Not shown in the figure is that a 1:3 slope was placed somewhat seaward of the structure to model the edge of the scour hole present at the Afsluitdijk. This slope caused breaking waves to be included in the wave action, resulting in a mixture between horizontal and vertical impact.
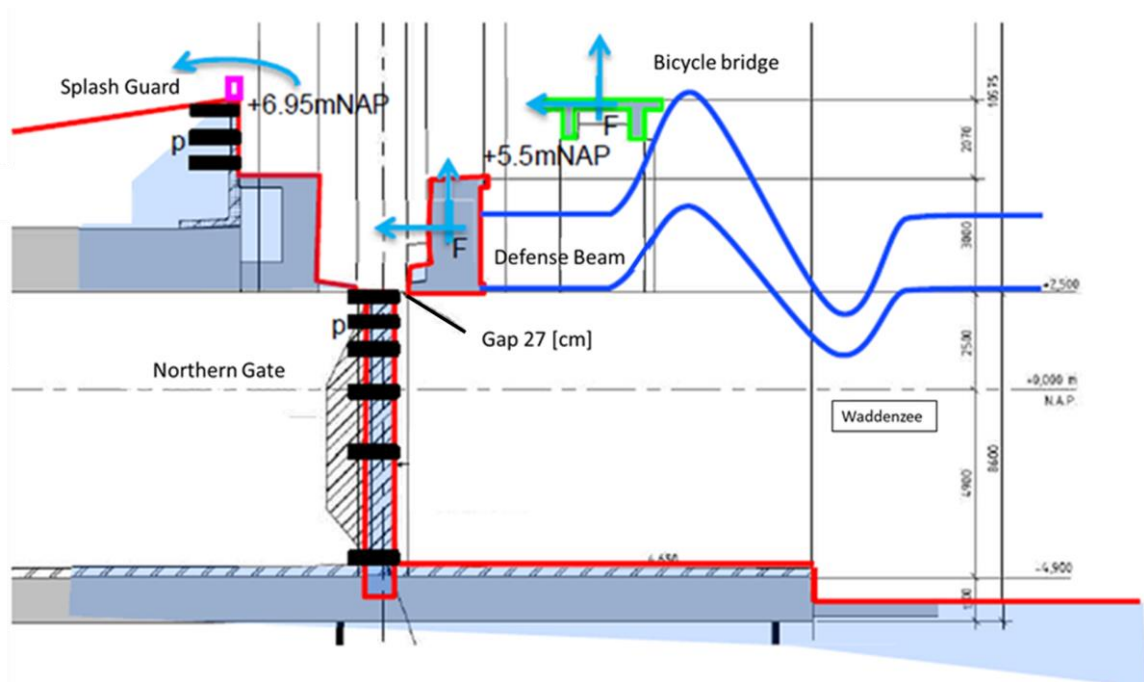
Figure 50. Model schematization of the tests by Hofland (2015) for the Northern gate and defense beam (Hofland, 2015).

Figure 51 shows the exact spatial distribution of the sensors in the gate. The fourth column shows the values normalized over the length of the overhanging structure. This scaling is introduced in order to create a comparable length over height ratio. The spatial integration of each sensor is determined by distance between each sensor. The exact middle between two sensors is also the division between the domains of those sensors. This is visualized in the last column with the corresponding domain length. Within each domain the measured value of the sensor is maintained, see Figure 52 where the gray areas represent the domain with equal pressure.

Type	Real depth [m]	Bottom zero [m]	Normalized [m]	Length covered [m]
Top	+ 2.50	+ 7.15	+ 3.40	
Sensor 4	+ 2.31	+ 6.96	+ 3.31	0.175
Sensor 5	+ 2.00	+ 6.65	+ 3.17	0.200
Sensor 6	+ 1.43	+ 6.08	+ 2.89	0.375
Sensor 7	+ 0.37	+ 5.02	+ 2.39	0.750
Sensor 8	- 1.76	+ 2.89	+ 1.38	1.175
				0.725
Sensor 9	- 4.60	+ 0.05	+ 0.02	
Bottom	- 4.65	+ 0.00	+ 0.00	
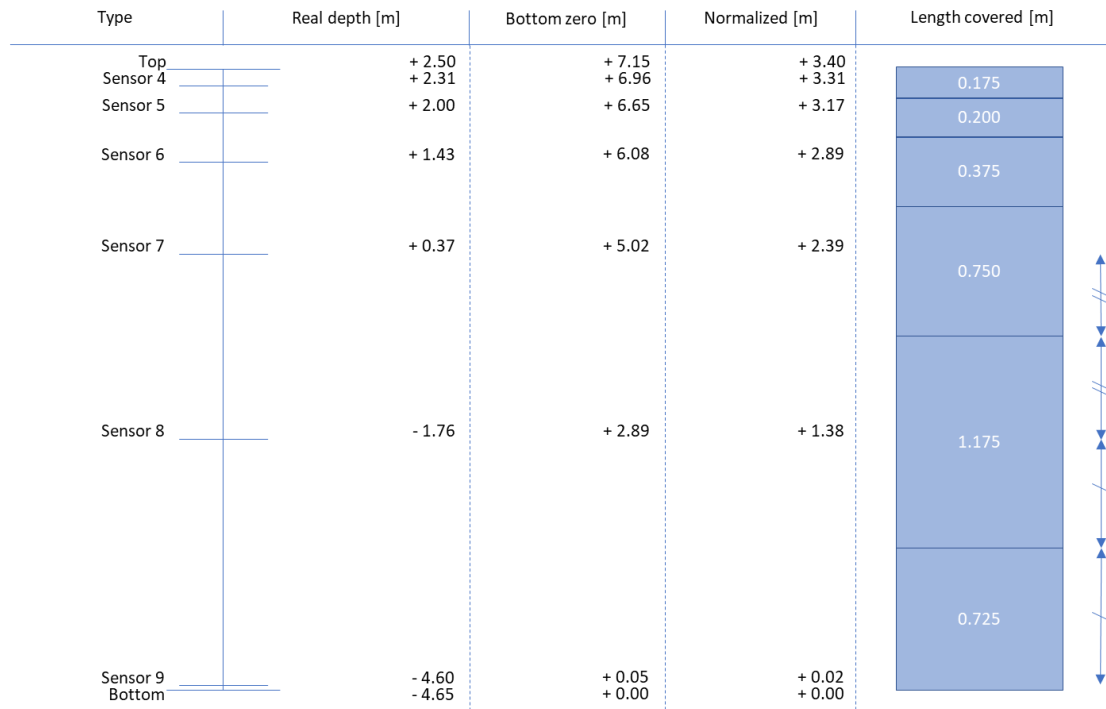
Figure 51. Height of each sensor from Hofland's experiment and its corresponding covered length.

Only the situations where the corner is filled with water during impact are used, because it complies with the assumption made in the mathematical method of Peregrine. This is the case when the mean water level is at the same level as the bottom of the overhanging structure. Two situations are within this demand and are shown in the following table. The difference between the water level and the bottom of the defense beam are still 0.1 m, but this is regarded as negligible.

Table 2. Input variables for the two situations of interest from Hofland (2015)

ID	Den Oever	H_s [m]	$T_{m-1.0}$ [s]	T_p [s]	h [m + NAP]
O3	Low water	2.08	3.88	4.55	2.6
	Kornwerderzand				
K3	Low water	1.69	3.95	5.02	2.6

The results of the two tests (O3 and K3) are shown in Figure 52 and Figure 53. The results show the maximum pressures of the test with a 95% confidence of each individual sensor (dotted line) and at the maximum force (solid line). The pressure distribution at the maximum force is taken as comparison. Results that show a maximum do not comply with a significant wave height as input. The significant wave height (H_s or H_{mo}), which equals the average of the highest one third of the waves or equals 4 times the standard deviation ($4 \cdot \sqrt{m_0}$) using a Rayleigh distribution, should be converted to the maximum wave height (H_{max}). In order to compare the physical scale test of Hofland and the numerical method derived from Peregrine the relation of H_{max} and H_s has to be defined. According to the Rayleigh distribution, the 1% highest waves or maximum in this case compared

with the significant wave height (4 times the standard deviation) equals 1.77 as shown in Equation 5.4.

$$\frac{H_{max}}{H_s} = 1.77 \qquad\qquad 5.4$$
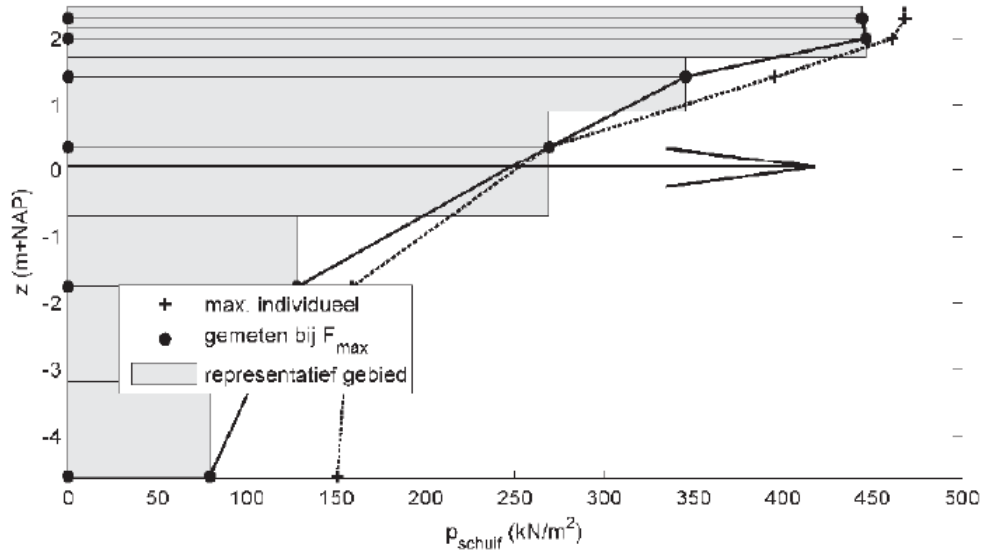
Figure 52. Results of the measured pressure of test O3 (REPORT: Modeltesten golfkrachten spuisluizen Afsluitdijk meetrapport).
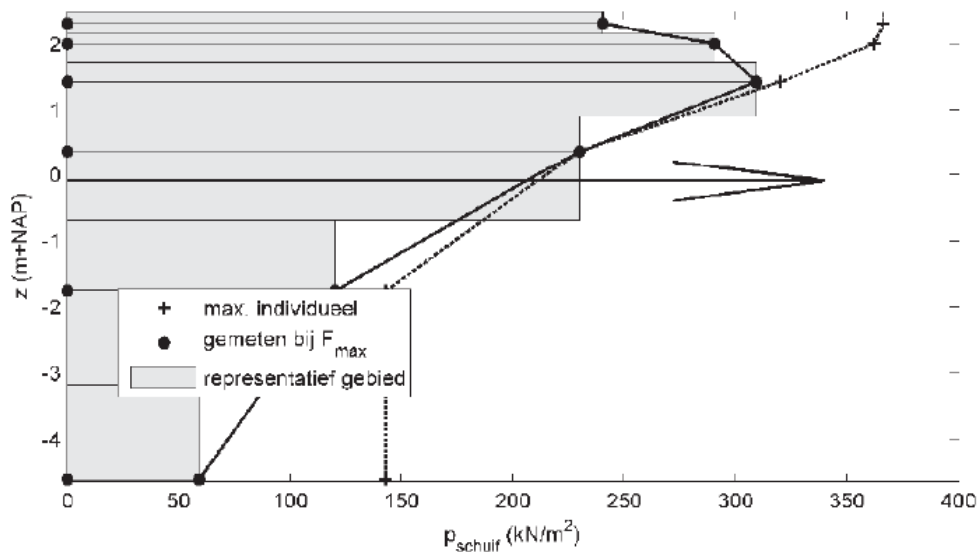
Figure 53. Results of the measured pressure of test K3 (REPORT: Modeltesten golfkrachten spuisluizen Afsluitdijk meetrapport).

As mentioned before, the numerical method derived from Peregrine requires a vertical velocity as input. The vertical velocity can be calculated using linear wave theory, see Equation 4.3. The vertical velocity, U_{max}, is calculated at the correct height, which is 0.1 m below the water level, and using the H_{max}, see Table 3.

ID	Den Oever	H_s [m]	H_{max} [m]	L [m]	h [m + NAP]	U_{max} at 2.5 NAP [m/s]
O3	Low water	2.08	3.68	29.37	2.6	2.43
	Kornwerderzand					
K3	Low water	1.69	2.99	34.02	2.6	1.81

The U_{max} is used to convert the pressure impulse or potential calculated with the numerical method, as can be seen in Figure 54, into a pressure distribution over the height of the water column, see Figure 55. Equation 5.5 shows the method of conversion. It is based on the reasonable assumption that an impact of a wave has a triangular shape in time. The impact duration is based on the time signal measured during the experiments, see Figure 30.

$$p = \frac{I_P \cdot \rho_f \cdot U_{max} \cdot 2}{T_s} \quad [kN/m^2] \qquad 5.5$$

Where,

I_p = Pressure-impulse [-]
ρ_f = Fluid-density [kg/m^3]
U_{max} = Maximum vertical particle velocity [m/s]
T_s = Timescale of wave impact [s]
p = pressure [kN/m^2]

Using Equation 5.5 over the complete height at the location of the gate (x = 0), the pressure distribution is calculated, see Figure 54. The output is only shown at the locations of the sensors of the physical experiment done by Hofland (2015) for comparison. The gap, see Figure 50 (27 cm) has been modeled by altering the top boundary and leaving some free surface at the location of the gap. The hole is 27 cm long, but is scaled in the same manner as the height to fit in the model. The pressure distribution measured by Hofland shows a distinct bend in the line, and is now also found in the numerical approximation, see Figure 55.
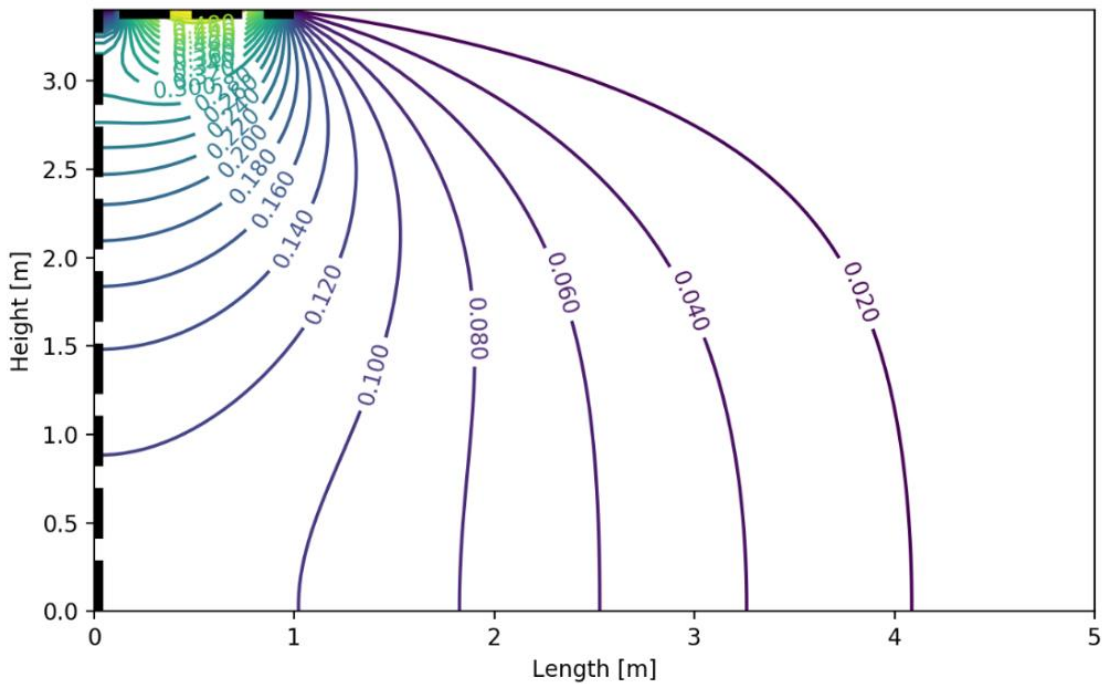
Figure 54. Pressure impulse contours of K3 calculated with Peregrine with the addition of a hole.
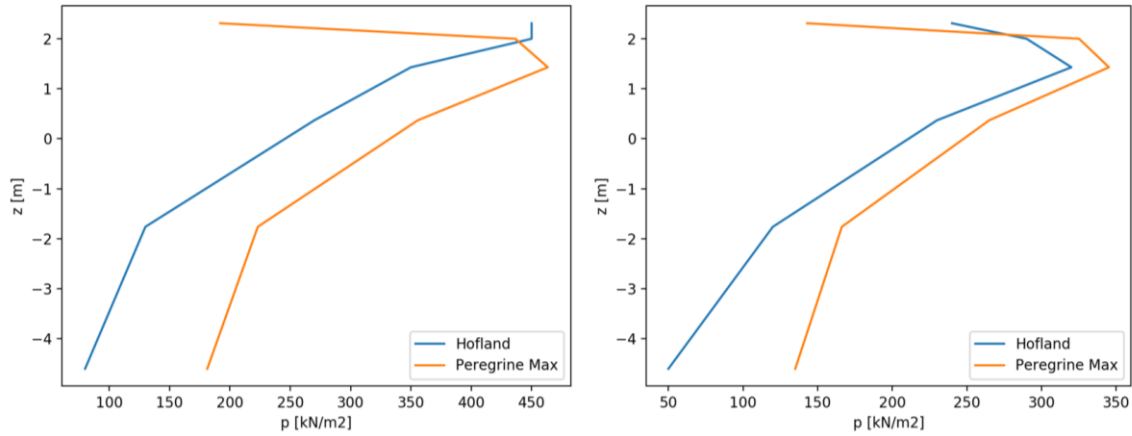
Figure 55. Pressures of O3 (left) and pressures of K3 (right) with the addition of the hole.

The numerical approximation ressembles the shape of the measured pressures fairly accurate. However the Peregrine method is still overestimating over the total height. This can be due to an overestimation of the vertical velocity or incorrect duration of the wave impact. The velocity that has been used as input is based on a the maximum vertical velocity of a linear harmonic standing wave, while in the situation of Hofland irregular nonharmonic waves are found. A translation has to be expected before the distribution will be similar.
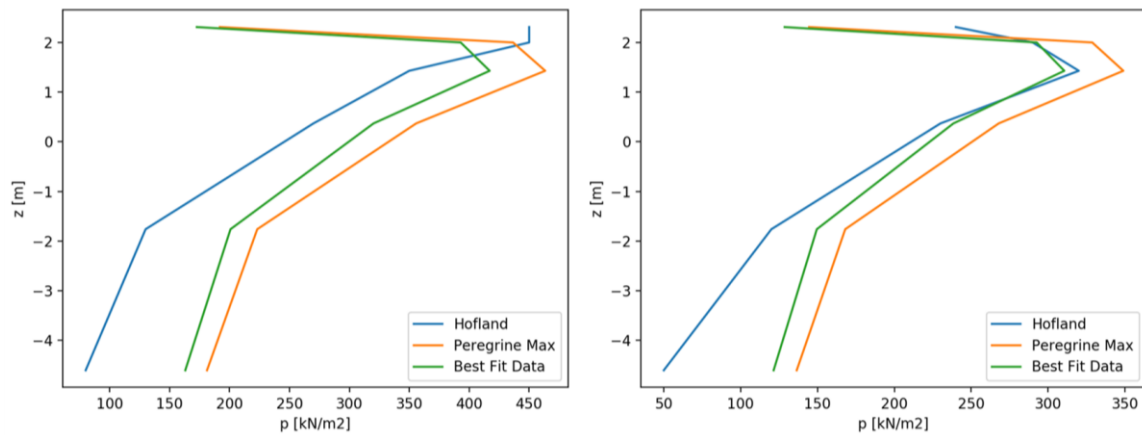
Figure 56. Pressure distribution comparison at Den Oever (left) and Kornwerderzand (right) with a best fit (RMS) to the data locations of the model test (empirical factor (V$_F$): 0.89 (left) and 0.88 (right)).

The only variables in Equation 5.5 are the time of the wave impact and the maximum vertical velocity. The time of the wave impact is determined by the measurements of the physical experiment, while the velocity follows from the linear wave theory. Therefore, a factor 'V$_F$' is placed in front of this variable, see Equation 5.6. With the use of a root mean squared analysis, the factor that results in the best fit of the pressure distribution is considered, see Figure 56. The root mean squared analysis is performed to fit the data points of the pressure distribution. For both situations a similar reduction factor is found with an average of 0.89. This results in the notion that Equation 5.6 can be considered an empirical relation with V$_F$ equal to 0.89.

$$p = \frac{I_P \cdot \rho_f \cdot g \cdot (V_F \cdot U_{max}) \cdot 2}{T_s} \quad [kN/m^2] \qquad 5.6$$

Table 4. Error of resultant horizontal force at both locations.

Location	Measured [kN]	Numerical [kN]	V_F [-]	Error [%]
Den Oever	677	861	0.94	27.1
Kornwerderzand	534	640	0.94	19.9
Den Oever	677	696	0.78	2.7
Kornwerderzand	534	515	0.78	3.6

5.3 Theoretical Explanation

The overestimation can be explained by assumptions in the theory. This section shows theoretical reasoning of the overestimation in the numerical method that is seen when fitting the data to the model tests.
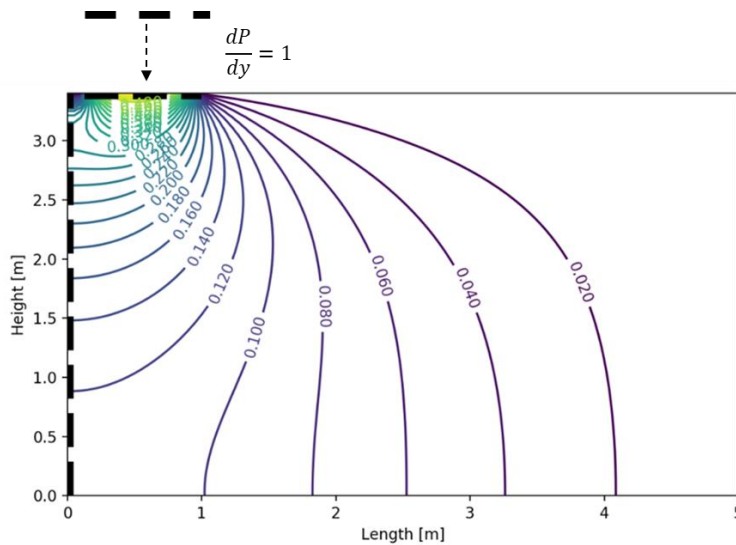
Figure 57. Physical visualization of the top boundary in the model of Wood & Peregrine (1996).

The top boundary in the methodology of Peregrine represents a vertical velocity, see Figure 57 for a visual representation. This vertical velocity can be calculated from the wave conditions using the linear wave theory derived by Airy in 1847 as is shown in the previous chapter. The vertical velocity is mathematically applied over the complete length of the boundary, representing the overhang. This creates a square shaped wave, see Figure 58. The figure also shows that the integration in both theories can explain the reduction factor needed to fit the model tests. The integration difference results in a factor of 0.94, which is relatively close to the empirical relation of 0.89 found in the previous section.
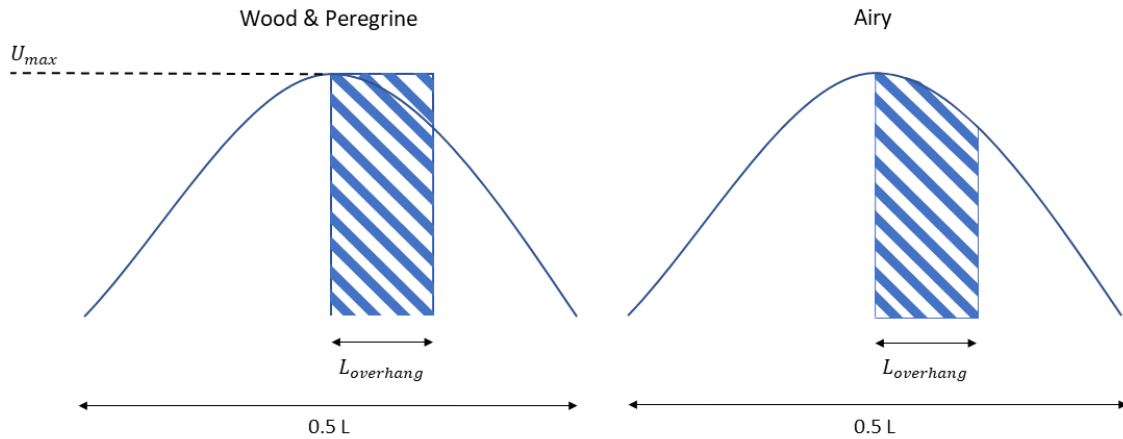
Figure 58. Visualization of the velocity integration difference in both theories.

This result gives a recommendation of how vertical pressures on a structure with an overhang could possibly be calculated. However, this theoretical explanation is based on only a single test with 2 conditions and should therefore be examined in greater depth before a correct analysis can be derived. When calculating the relative error of the results from the numerical method including the factor of 0.94 with the measurements of the model test, it still shows large deviations, see Figure 59. The figure also shows that the largest errors occur in the top and bottom of the pressure distribution but are fairly correct at the location of the largest pressures, which arguably have the most impact to the design load.
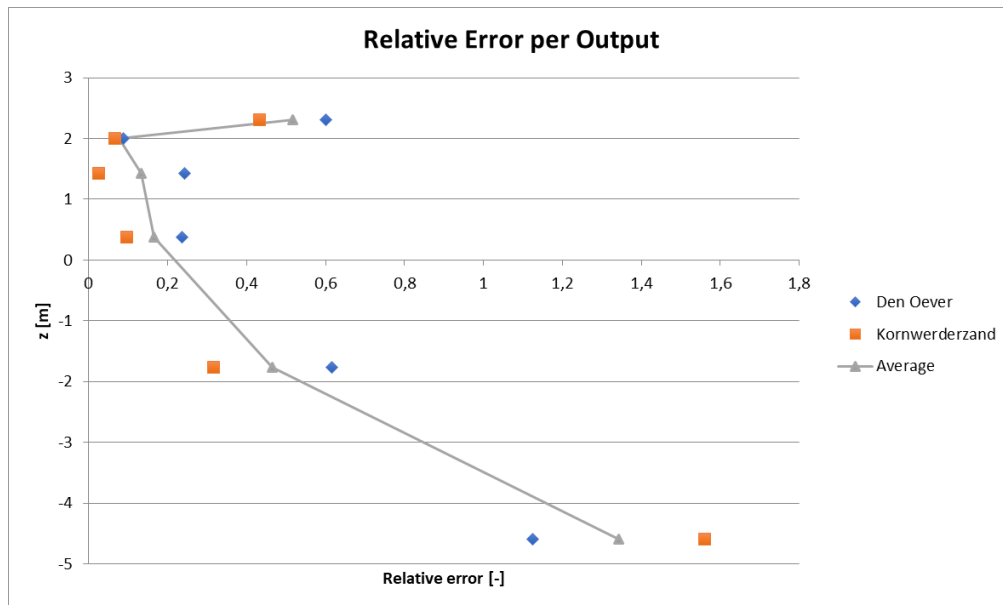
Figure 59. Relative error of numerical results with empirical relation of 0.94 of the two situations in the model test.

5.4   Conclusion

The numerical method based on the paper of Wood and Peregrine (1996) provides a good alternative to the model test executed for the case. The numerical method can be implemented as forcing into the proposed model in Chapter 6 giving the possibility to analyze and design more complex systems than before. The empirical relation derived is however only based on a single model test that was not focused on this method. Therefore, new research is recommended in Chapter 8.
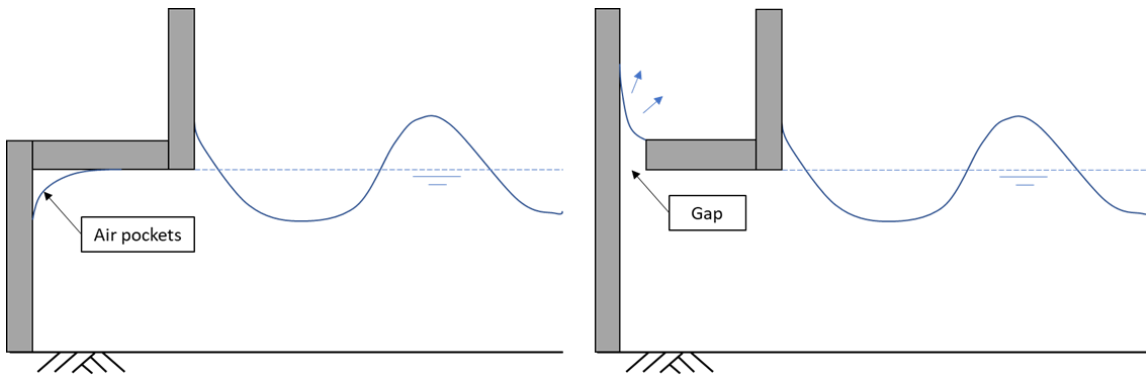
Figure 60. visualization of trapped air pockets.

As mentioned in Chapter 4.3 that the effect of air pockets can lead to great variation in the pressure distributed to the structure. Therefore, when applying the numerical method specified in this chapter it would be advised that a gap should be present. Figure 60 shows in a very simplistic manner how the effect of the air entrapment is minimized due to a good placed gap. In order to see the effect of the length of the gap compared to the length of the overhang a sensitivity analysis is executed, see Figure 61. Also, other parameters of interest have overcome the same procedure. The analysis shows the effect of each parameter to the resultant horizontal force over the dimensionless variable d/H. The case of the northern gate at Den Oever is placed in each subfigure to show some reference. The variable 'Ts', which represents the equivalent length of time of the impulsive wave impact, can be seen to have a large influence on the horizontal force. However, this is the only one that is still difficult to predict without having a model test or significant data (pressure signal at impact) at the project location.
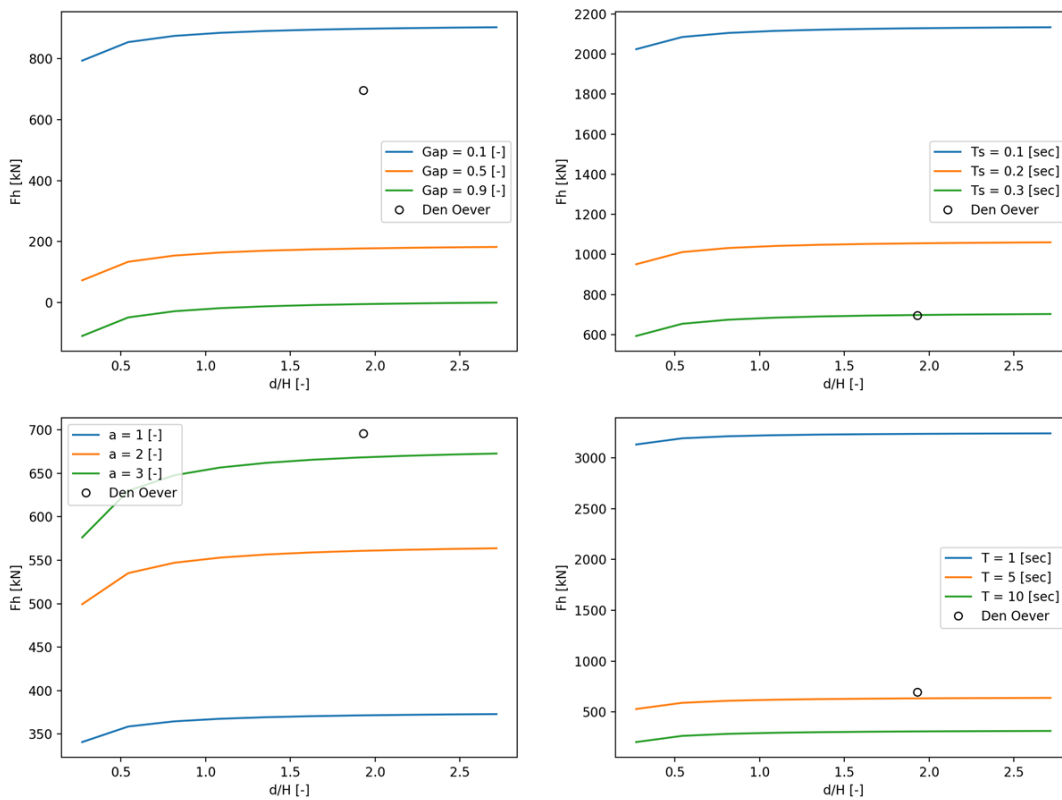
Figure 61. Sensitivity analysis of the numerical method compared to the northern gate at Den Oever (Hofland, 2015); gap = 0.128 [-]; Ts = 0.3 [sec]; a = 3.4 [-]; T = 4.55 [sec].

6 Semi-Analytical Model

This chapter elaborates on the semi-analytical model and is the start the second step in the research. The focus is on the link with a finite element method and how that is fitted within the rest of the model, see section 6.2. In section 6.3 the FSI-model is compared with the engineering practice from Chapter 3. This comparison is based on the case of the northern gate at Den Oever in the governing conditions of the gate formulated by Levvel.

6.1 Model Description

This first section gives a description of the model and the implementation of the case. The case, as discussed in earlier Chapters 1 and 2, has been simplified in a model representation, see Figure 62. In this representation the gate is still considered as a homogenous and isotropic thin plate. Section 6.2 will expand on that simplification.
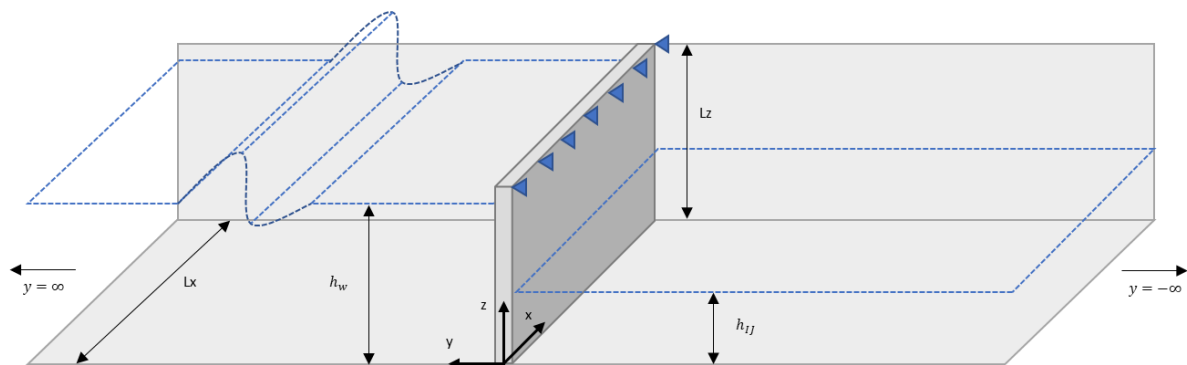
Figure 62. 3D model representation of the case.

The model is based on a semi-analytical method that can solve the interaction between the fluid and the structure (gate). This method describes the fluid response in terms of structural modal coefficients when using the interface conditions. This leads to a system of analytical equations including the external forcing, which can be solved for the structural modal coefficients. The derivation is based on (Tieleman O. C., 2015), who extended the method of (Tsouvalas, Dalen, & Metrikine, 2015). They stated that to solve the coupled vibro-acoustic problem, three methods can be used; Finite Element methods, Boundary Element methods and Semi-analytical methods. The latter had their focus as in cases of relatively simple geometry it reduces the computational time significantly. The basic derivation of the method is shown I the following steps.

- Expressing the displacement of the structure in terms of an infinite summation of in-vacuo modal shapes and coefficients found for the homogeneous structural equation of motion.
- Expressing the fluid response in terms of modal shapes and coefficients.
- Using the interface condition to express this fluid response in terms of the structural coefficients.
- Substitution of the found expressions into the forced equation, obtaining an analytical system of equations with the modal coefficients as the only unknowns.
- Solving the system of equations for each external force amplitude and frequency.

The next sections show a theoretical formulation of the basic derivation of the method. The method described is verified with a numerical model COMSOL in (Tieleman, Tsouvalas, Hofland, Peng, & Jonkman, 2018). The equations of motion and boundary conditions are presented in the frequency domain as the model operates in that domain.

6.1.1 Structural Model

The equation of motion is based on the linear bending vibrations of a homogeneous isotropic rectangular thin plate. This structural model is expanded in Chapter 6.2, but still shows the origin of the model. It is assumed that the spatial distribution of the force does not change in time, making it possible to separate the force in a space- and time-dependent part. The Fourier transform allows the transformation to the frequency domain resulting in the following equation of motion, see Equation 6.1.

$$-\rho_s \omega^2 \widetilde{w}(x,z,\omega) + D\left[\frac{\delta^4 \widetilde{w}(x,z,\omega)}{\delta x^4} + 2\frac{\delta^4 \widetilde{w}(x,z,\omega)}{\delta x^2 \delta y^2} + \frac{\delta^4 \widetilde{w}(x,z,\omega)}{\delta z^4}\right] =$$

$$-f_l(x, y=0, z, \omega) + f_r(x, y=0, z, \omega) + f_e(x, z, \omega)$$

6.1

$\widetilde{w}$ represents the complex vibration amplitude of the gate. The plate is considered geometrically thin with neglection of shear deformation. D is the uniform bending rigidity, ρ_s is the distributed mass per unit of area, f_l and f_r are the fluid pressures at either side acting on the surface of the gate, finally f_e represents the time signal of the external force distribution on the plate.

$$\widetilde{w}(x=0,z,\omega) = M_{xx}(x=0,z,\omega) = \widetilde{w}(x=L_x,z,\omega) = M_{xx}(x=L_x,z,\omega) = 0 \qquad 6.2$$

$$V_{zy}(x,z=0,\omega) = M_{zz}(x,z=0,\omega) = \widetilde{w}(x,z=L_z,\omega) = M_{zz}(x,z=L_z,\omega) = 0 \qquad 6.3$$

The top edge of the gate is simply supported just as both edges on the side, while only the bottom edge is free. These boundary conditions are shown in Equations 6.2 and 6.3.

$$\widetilde{w}(x,z) = \sum_{m=1}^{\infty}\sum_{k=1}^{\infty} A_{km}W_{km}(x,z)$$

6.4

The response of the plate can be found as the summation of the in-vacuo modes multiplied by unknown modal amplification, see Equation 6.4. The modal shapes of each structural mode and corresponding natural frequencies can be calculated by solving the homogeneous part of Equation 6.1. This can be solved analytically or numerically, where the latter is shown in Chapter 6.2.

6.1.2 Fluid Model

Both fluid domains are exactly similar besides the fact that they are each other's mirror image in y-direction. For brevity, the fluid pressure equations are elaborated for a single side of the gate, which is why the subscripts 'l' and 'r' are omitted. The motion of the compressible fluid is described in the frequency domain in Equation 6.5. It is considered irrotational and can therefore be described by the velocity potential.

$$\nabla^2 \widetilde{\varphi}(x,y,z,\omega) + k_f^2 \widetilde{\varphi}(x,y,z,\omega) = 0$$

6.5

The boundary conditions applied for the fluid domains can be found in the following Equations 6.6, 6.7 and 6.8. Zero velocity is enforced at the impermeable walls of the lock. The free surface is known from linear wave theory and the velocity compatibility is applied at the structure-fluid interface at the gate.

$$\frac{\delta\widetilde{\varphi}(x,y,z,\omega)}{\delta x}(x=0) = \frac{\delta\widetilde{\varphi}(x,y,z,\omega)}{\delta x}(x=L_x) = \frac{\delta\widetilde{\varphi}(x,y,z,\omega)}{\delta z}(z=0) = 0 \qquad 6.6$$

$$\frac{\delta \tilde{\varphi}(x,y,z,\omega)}{\delta z}(z=h) = \frac{\omega^2}{g}\tilde{\varphi}(x,y,z,\omega)(z=h) = 0 \qquad 6.7$$

$$\frac{\delta \tilde{\varphi}(x,y,z,\omega)}{\delta y}(y=0) = i\omega \tilde{w}(x,z,\omega) \qquad 6.8$$

The expression in Equation 6.9 shows the solution, where Φ_{pr} the two-dimensional modal fluid shapes in the parallel to the surface of the gate are and B_{pr} represent the fluid modal coefficients.

$$\tilde{\varphi}(x,y,z) = \sum_{p=1}^{\infty}\sum_{r=1}^{\infty} B_{pr}\cos(k_{x,p}z)\cos(k_{x,r}x)e^{-ik_{y,pr}y} = \sum_{p=1}^{\infty}\sum_{r=1}^{\infty} B_{pr}\Phi_{pr}(x,z)e^{-ik_{y,pr}y} \qquad 6.9$$

6.1.3 Modal Coupling

In order to solve the complete system of equations, the fluid response is expressed in terms of structural coefficients. The solutions of Equations 6.9 (fluid) and 6.4 (structural) are substituted into the interface condition of Equation 6.8 to reach an expression that can be rewritten to describe the fluid modal coefficients B_{pr} in terms of the structural modal coefficients. The coefficients are substituted in Equation 6.9 and subsequently in Bernoulli's pressure equation to find the fluid pressure in the entire domain, see Equation 6.10.

$$p_f(x,y,z) = i\omega^2\rho_f \sum_{m=1}^{\infty}\sum_{k=1}^{\infty} A_{mk} \sum_{p=1}^{\infty}\sum_{r=1}^{\infty} \frac{Q_{km,pr}}{k_{y,pr}\Delta_{pr}}\Phi_{pr}(x,z)e^{-ik_{y,pr}y} \qquad 6.10$$

The variable $Q_{km,pr}$ is given in Equation 6.11, where S_w is the surface occupied by the stationary fluid at $y = 0$.

$$Q_{km,pr} = \iint_{Sw} W_{mk}(x,z)\,\Phi_{pr}(x,z)dxdz \qquad 6.11$$

Equation 6.10 shows that the real values of $k_{y,pr}$ correspond to the propagating modes and yield an imaginary value of the hydrodynamic pressure in the frequency domain, which is identical to radiation damping. Also, the imaginary values correspond to the evanescent modes and yield real valued hydrodynamic pressures, which depending on the sign are equivalent to a hydrodynamic mass or stiffness.

6.1.4 Force Model

As mentioned earlier, the force is applied as a time signal, see Figure 63. This signal is transformed to the frequency domain by applying the Fourier transform. The spatial distribution of the force is assumed to stay constant in time, allowing to separate the time and space fields of the forcing functions. Also, the time signal of the force is independent of the motion of the gate.
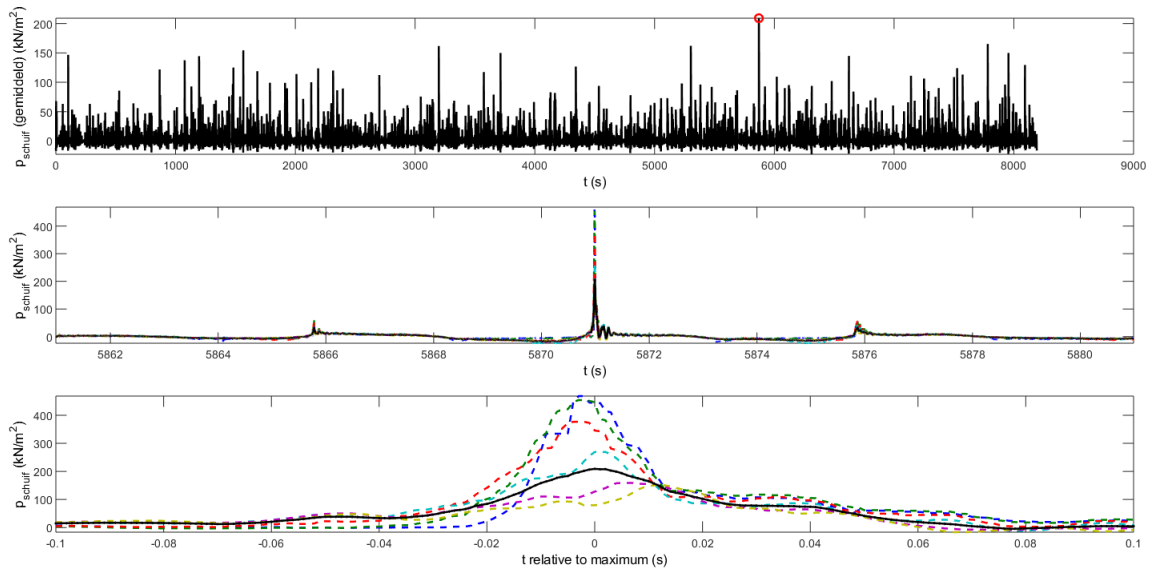
Figure 63. Time signal of the governing condition of the wave impact for the gate (Hofland, 2015).

The maximum measured wave impact of that timeseries as described in Appendix B functions as the governing condition in the quasi-static method of Kolkman, see Chapter 3. This governing load condition together with the corresponding hydrostatic pressures of each side are visualized with the gate in Figure 64. It is clearly visible that the water level at the IJsselmeer-side is very low and does not even reach the second horizontal stiffener from the bottom.
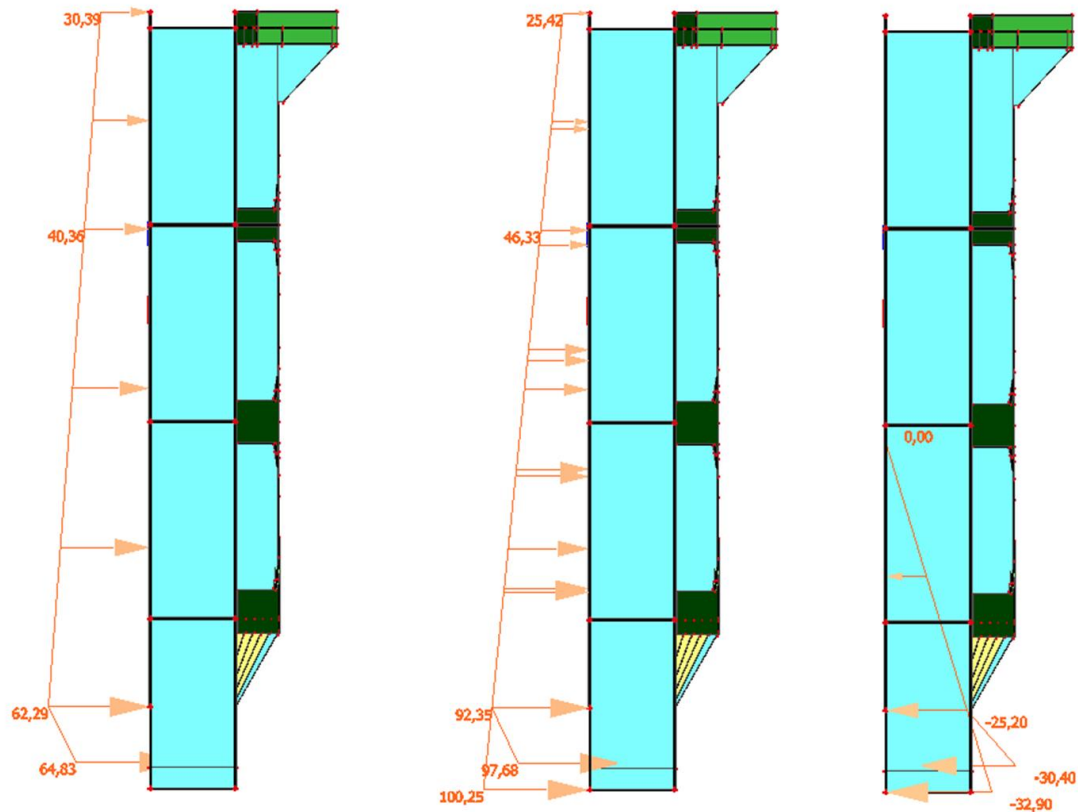
Figure 64. Distributions of the governing static loads on the gate; The wave impact (left); The hydrostatic pressure of the Waddenzee (middle); The hydrostatic pressure of the IJsselmeer (right).

6.1.5 System of Equations

The solutions of the fluid and structural model are uniquely described in terms of structural modal coefficients. The complete system of equations is a result of Equation 6.10 substituted in the forced Equation 6.1 transformed into the frequency domain, which result in Equation 6.12.

$$\sum_{k=1}^{\infty}\sum_{m=1}^{\infty}[\rho_s(\omega_{km}^2 - \omega^2)\delta_{kl}\delta_{mn}\Gamma_{ln} - L_{km,ln} + R_{km,ln}] = F_{ln} \qquad 6.12$$

Where the fluid pressures are given by Equations 6.13 and 6.14 and the modal is force by Equation 6.15.

$$L_{km,ln} = i\omega^2\rho_f\sum_{p=1}^{\infty}\sum_{r=1}^{\infty}\frac{Q_{km,pr}Q_{ln,pr}}{k_{y,pr}\Delta_{pr}}(h = h_w) \qquad 6.13$$

$$R_{km,ln} = i\omega^2\rho_f\sum_{p=1}^{\infty}\sum_{r=1}^{\infty}\frac{Q_{km,pr}Q_{ln,pr}}{k_{y,pr}\Delta_{pr}}(h = h_{ij}) \qquad 6.14$$

$$F_{ln} = \iint_S \tilde{f}_e(x,z,\omega)\,W_{ln}(x,z)dxdz \qquad 6.15$$

6.2 FSI-model Coupled to FEM & Discretization

SCIA Engineer is used to construct the modal shapes numerically, see Figure 65. The design constructed in FEM is analysed and the modal shapes calculated by the software are used in the FSI-model. These modal shapes then replace the in-vacuo modes constructed in the FSI-model and corresponding natural frequencies of Equation 6.4. This allows for further complexity of the shape of the gate, because it is not limited to the analytical solutions of the plate structure. However, the FEM gives discretized solutions instead of continuously. This section, besides the coupling, shows how this has been done.
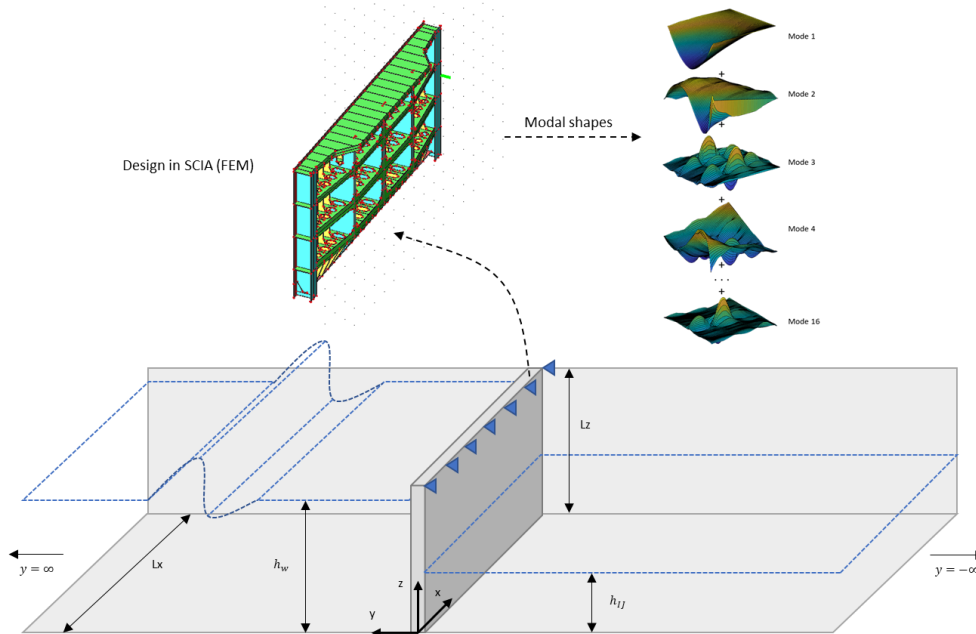
Figure 65. Visualisation of the application of a FEM within the FSI-model.

The software SCIA Engineer has been used for this report as it was available at Witteveen + Bos. However, the method is not limited to this software. The general approach can be applied to any FEM. The link between the model and the software should be the only problem. The complete schematic overview of the model as explained in the previous segment is shown in Figure 66. The addition made with FEM is found in the structural model. Appendix J contains a more detailed guideline that ensures the model functions accordingly.
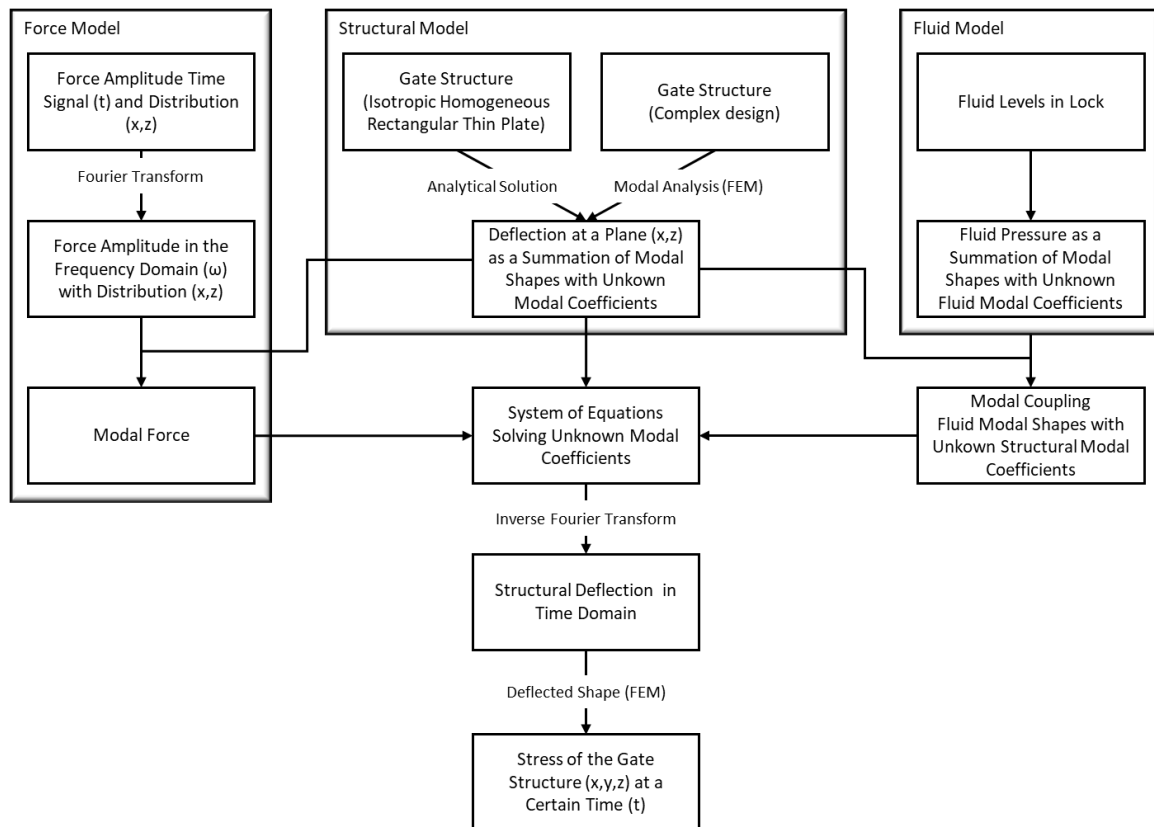
Figure 66. Schematic overview of the semi-analytical model including the link with SCIA (FEM).

61

All nodes at every location in x-y-z-coordinates of the gate are used in the calculation of the modal shapes in FEM. However, the FSI-model still operates with a flat plate assumption, meaning that a translation step is required. A virtual surface down the middle of the front plate is used as the plate in the FSI-model, see Figure 67. SCIA calculates the modal shapes of the entire structure with the influence of the stiffeners, but then only return the output of the nodes that are located in the front plate. An issue rises at the bottom section of the gate, where the front plate is angled. This is solved by locating the actual calculated shape deformations to the virtual surface that continues in a straight path, see Figure 67.
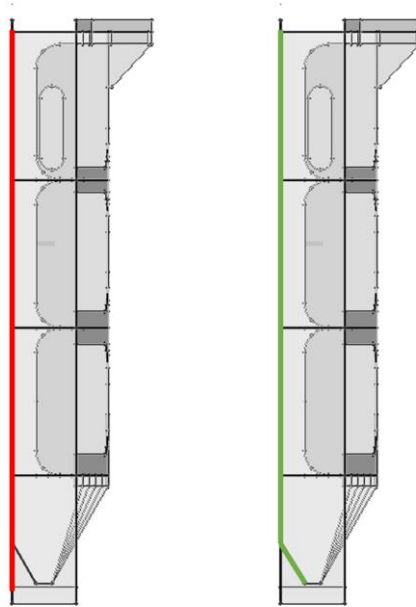
Figure 67. Side view of the northern gate showing the virtual surface (left, red) and the output surface (right, green).
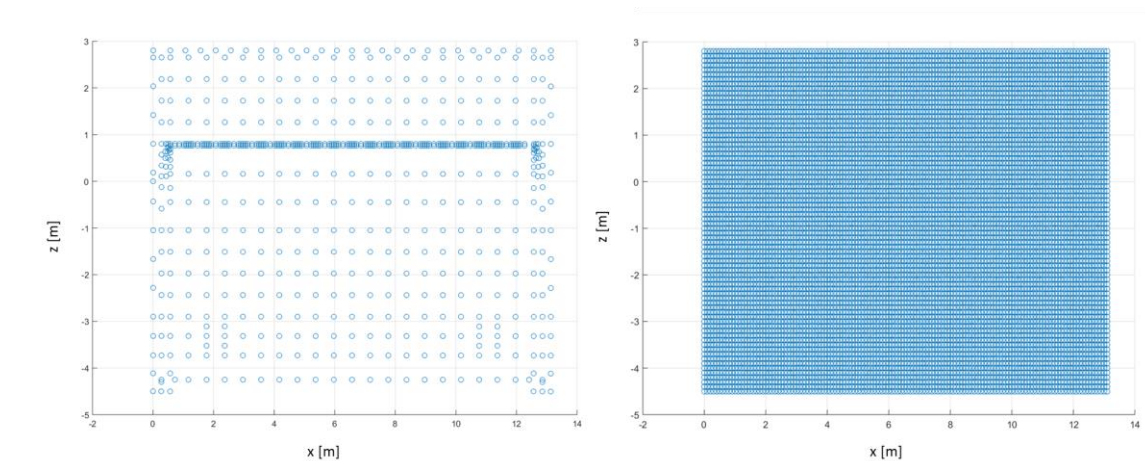
Figure 68. Discretized output raw (left) and interpolated over an equal spaced grid of 0.1 m grid size (right).

The data of each modal shape is received by the FSI-model with an accuracy of 0.5 m in both the x and z direction, see Figure 68 on the left. The raw data is then further linearly extrapolated to fit a grid with a grid size of 0.1 m in both directions as can be seen in Figure 68 on the right. The semi-analytical method of the FSI-model is based on the notion that the functions are orthogonal. Two functions are orthogonal if the integral of the multiplication of both functions, see Equation 6.16, is equal to zero when they are not same function ($f \neq g$). The linearly extrapolated modal shapes need to be fitted to a two-dimensional orthogonal function. A few options are available, but the Gram-Schmidt process is applied in this thesis (O'Leary & Harker, 2010). This process takes a

nonorthogonal set of linearly independent function and constructs an orthogonal basis over an arbitrary interval with respect to an arbitrary weighting function. The result of this process gives the Legendre polynomials (Leon, Bjorck, & Gander, 2013). The algebraic framework of the applied method can represent a virtually perfect Gram polynomial basis enabling to fit on a two-dimensional lattice.

$$\langle f, g \rangle = \iint f(x)g(z)dxdz \qquad\qquad 6.16$$

Figure 69 shows how the normalized modal shapes of two exemplary modes are linearly extrapolated from the raw data to the equally spaced grid and eventually fitted to the orthogonal polynomials.
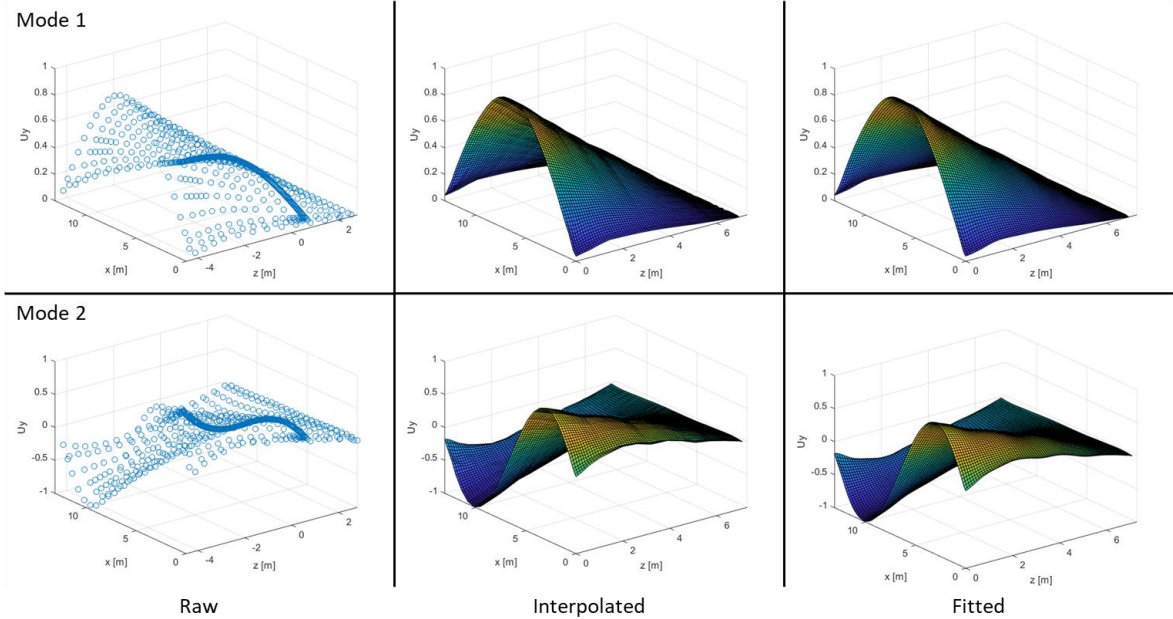
Figure 69. raw output (left), linearly interpolated (middle) and fitted to orthogonal polynomials (right) of the first (top) and second (bottom) mode.

The degree of the polynomials can be chosen in both the x- and z-directions. A modal shape is built up of these polynomials with different weight to each degree in a certain direction. The error between the shape of the surface from the FE-model interpolated and of the shape fitted to the orthogonal polynomials should be as small as possible i.e. smaller than 10 percent. The fitted shape is used further in the semi-analytical model and should represent the real situation as good as possible. Increasing the amount of degree of the polynomials in both directions lowers the error, but also increases the computation time. 25 degrees in both directions was found to result in a good fit for all 16 modal shapes. The average of the maximum relative error of all 16 shapes was 0.08 with a maximum at 0.19, which was an exception that only occurred at mode 15 and does not contribute to the maximum deflected shape, see Figure 71. When applying 36 degrees in both directions the average relative error is reduced to 0.05, showing that 25 degrees is a reasonable estimate for this application.
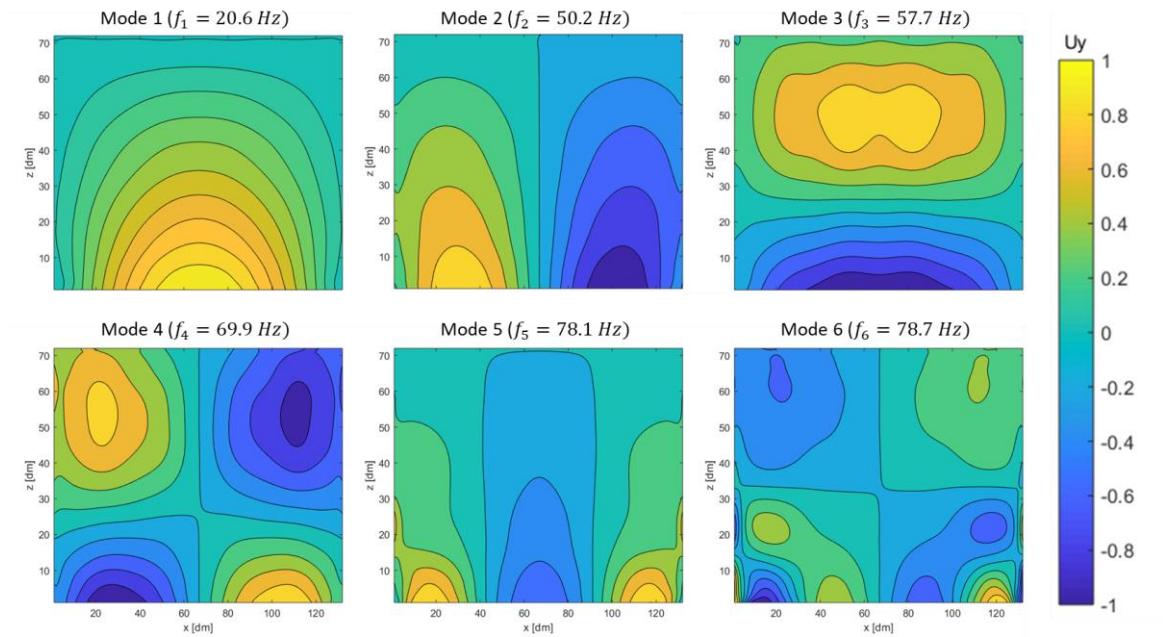
Figure 70. The first 6 modal shapes of the gate designed by Levvel.

The normalized modal shapes fitted to a homogeneous grid based on orthogonal functions, see Figure 70, allows for the calculation in the FSI-model. The model produces a deflection of each node for a specific frequency. When applying an inverse Fourier transform the deflection of each node in time can be found. Finally, the deflected shape of the model is then returned to SCIA with the same nodal spacing of 0.1 m in order to impose the shape unto the design and find the stresses in the model at each location including the stiffeners at the back of the plate.

6.3   Results of Semi-analytical model

Combining all the modal shapes produced by SCIA, a total of 16, together with the design load shown in Figure 63 an analysis by the semi-analytical model is completed. One of the results is a deflected shape of the virtual plate with the maximum amplitude as seen in Figure 71. The shape resembles the first modal shape, as can be confirmed by the contribution shown in the same figure on the right side. However, higher modes also contribute to this maximum deflected shape, which can be related to the fact that the constraints of the gate are not at the edge and are also modeled as a single point, see Figure 21.
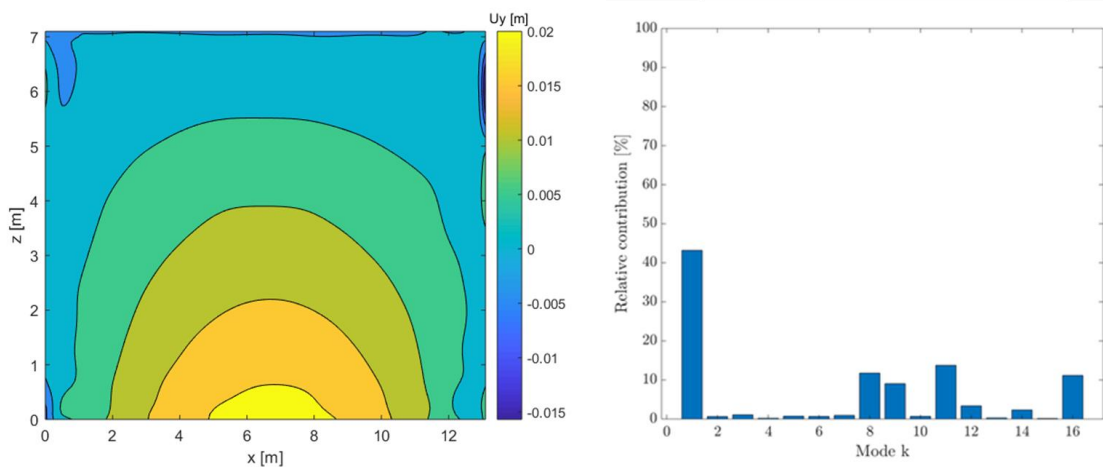
Figure 71. Maximum deflected shape (left) of the case calculated by the semi-analytical model with the contributing modes (right).

	f_1 [Hz]	f_2 [Hz]	f_3 [Hz]	f_4 [Hz]	f_5 [Hz]	f_6 [Hz]	f_7 [Hz]	f_8 [Hz]	f_9 [Hz]	f_{10} [Hz]
In-vacuo	20.6	50.2	57.7	69.9	78.1	78.7	81.0	91.1	91.2	105.1
Immersed	1.1	21.3	48.9	56.7	66.0	71.8	78.5	80.7	82.3	95.1
Without Surface Waves	1.0	21.0	47.3	55.8	63.1	71.1	78.4	80.6	81.9	91.3
With Compressibility	1.1	21.3	48.2	55.9	62.4	71.0	78.5	80.6	81.7	90.9
Both	1.1	21.3	48.2	55.9	62.4	71.0	78.5	80.6	81.7	90.9

Table 5 shows the difference between the found immersed and in-vacuo resonance frequencies, where Figure 72 shows how the plate responds to those immersed resonance frequencies. The first three resonance shapes and their contributing modes are shown in Figure 73. Due to the nature of the force, which is equally distributed in x-direction, the shapes should show symmetry. This is the case; however, some deviations are visible, but can be related to the minor inaccurate depiction of the found resonance frequency.
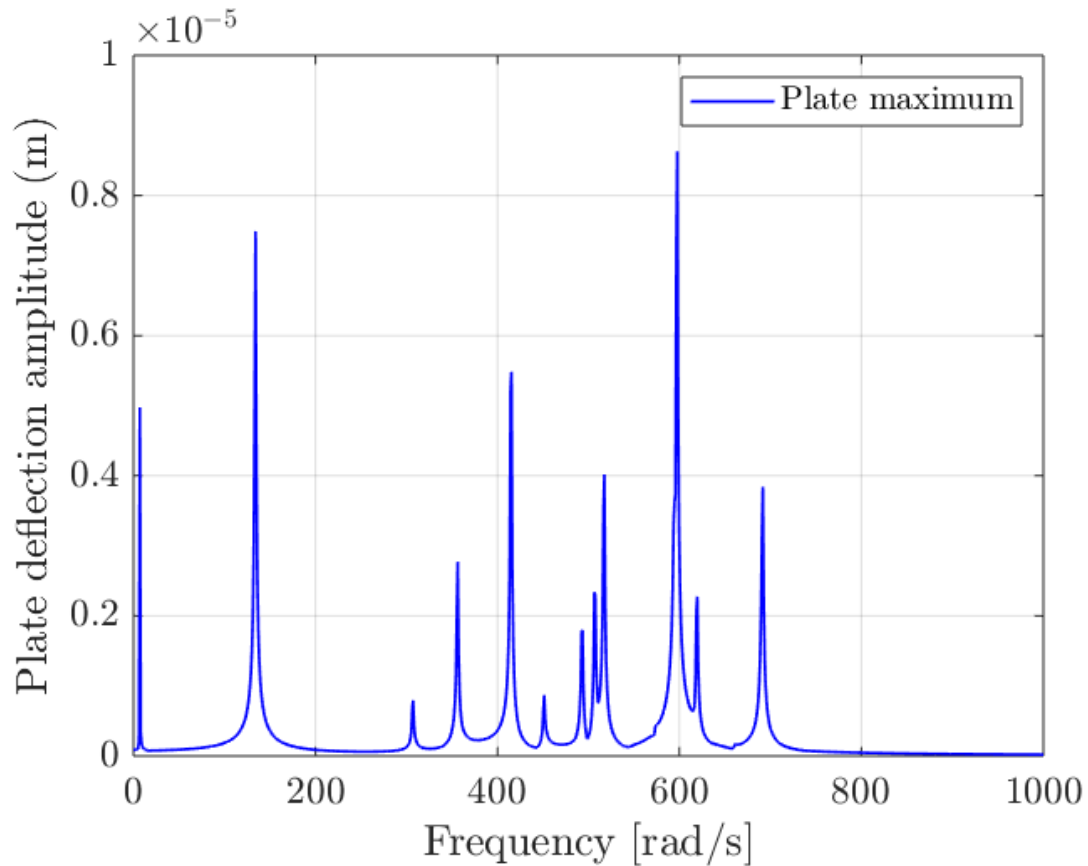
Figure 72. Peak amplitudes at first 11 immersed resonances.

65
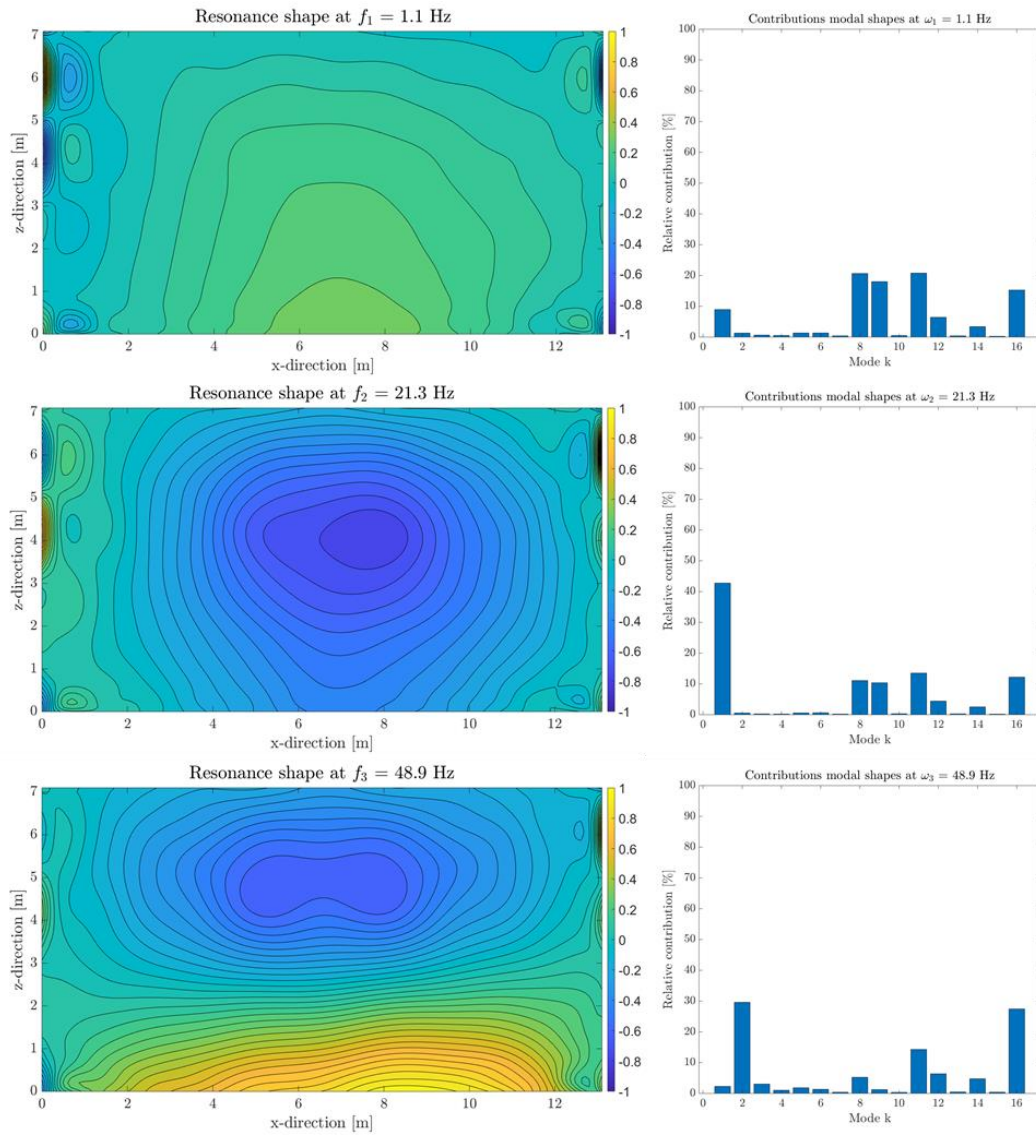
Figure 73. Relative contribution of modes and shapes for the first three resonances.

This deflected shape is then retransferred to the SCIA-model with the established link to see how the actual design responds to this imposed deflection of the virtual plate, see Figure 74. The results of stresses and forces in the structure are shown in the next section, where they are compared with the quasi-static method.
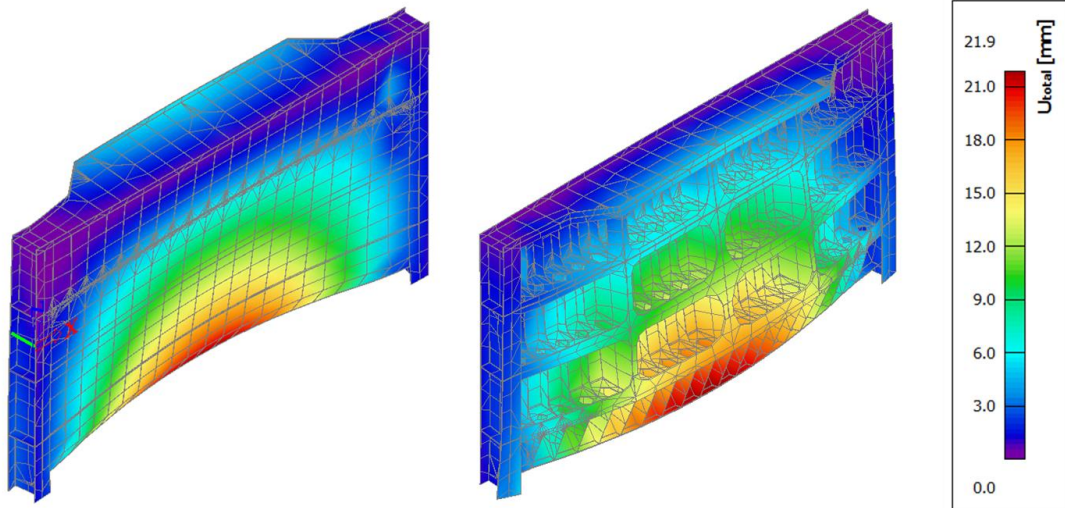
Figure 74. Shape of deflection imposed unto the 3D model in SCIA.

Applying the 2 per cent of structural damping that was shown in Chapter 3 to be a conservative approach, to the system. The damping is equally enforced to every frequency. Using 4.1 allows for the transformation of the 2 per cent structural damping to be used in the model, resulting in an c of 54 $Ns/m \cdot m^{-2}$. Figure 75 shows the response in time of three locations on the gate. Even with damping it can be seen in the top figure that the signal is still continuing after the wave impact has occurred. For a correct application of the Fourier transform the signal has to finish with no vibration. This can be reached by increasing the timescale of the analysis, however this will enlarge the computation time and is not found interesting as it shows the signal slowly decrease in amplitude. The important section of the analysis has been captured, which is the maximum amplitude at the moment of the impact at 0.5 seconds.
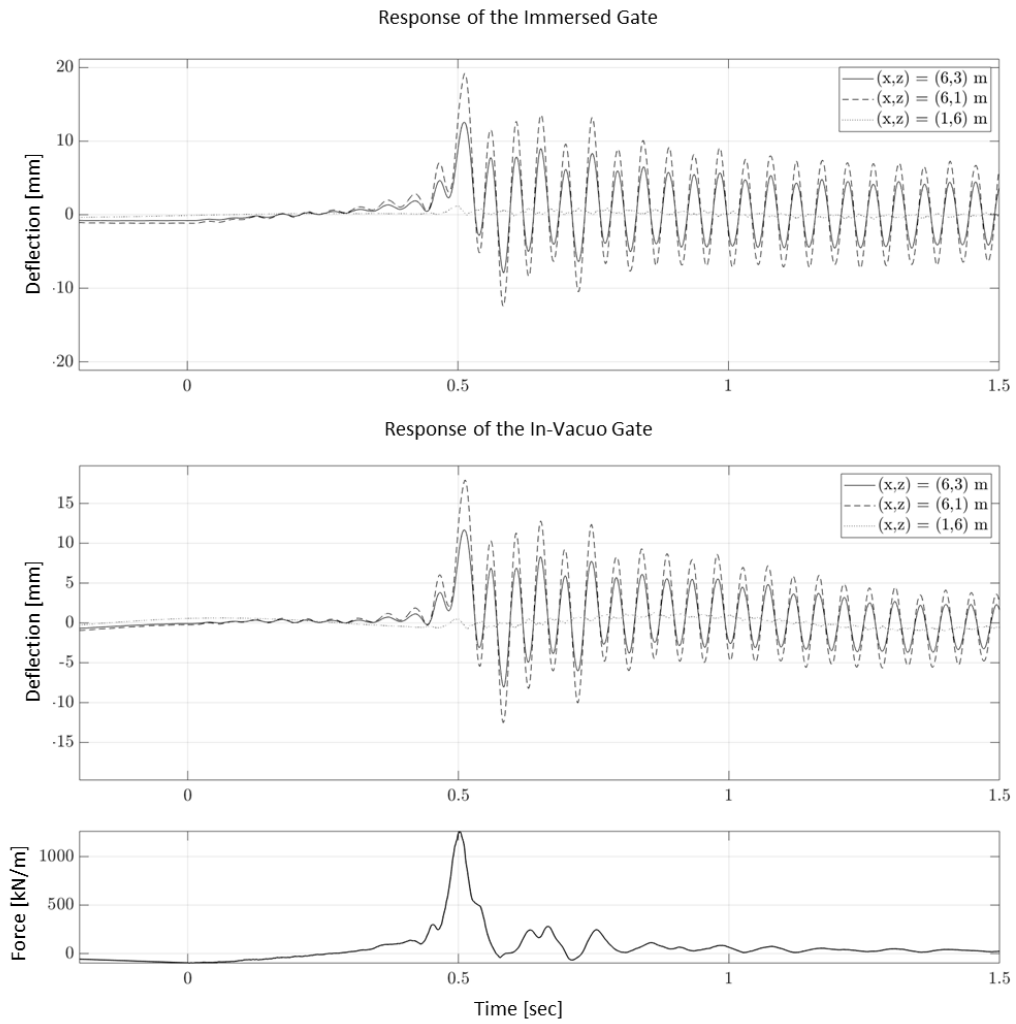
Figure 75. Deflection response of the gate in time with damping.

6.4   Comparison of Kolkman and Semi-analytical Methods

To compare the quasi-static method from Chapter 3 and semi-analytical method combined with the FE-model, the deflection and stress in the structure is analyzed. The quasi-static model is calculated with a Dynamic Amplification Factor (DAF) of 1.39, which resulted from the analysis in Chapter 3. The overall maximum deflected shape shows a lot of similarities, see Figure 76. Even though the semi-analytical method is based on the first 16 modal shapes, it resembles the quasi-static shape, which is only based on the first mode. The maximum deflection is less in the semi-analytical method, which can be due to the fact that the extra contributing modes also take away some energy.
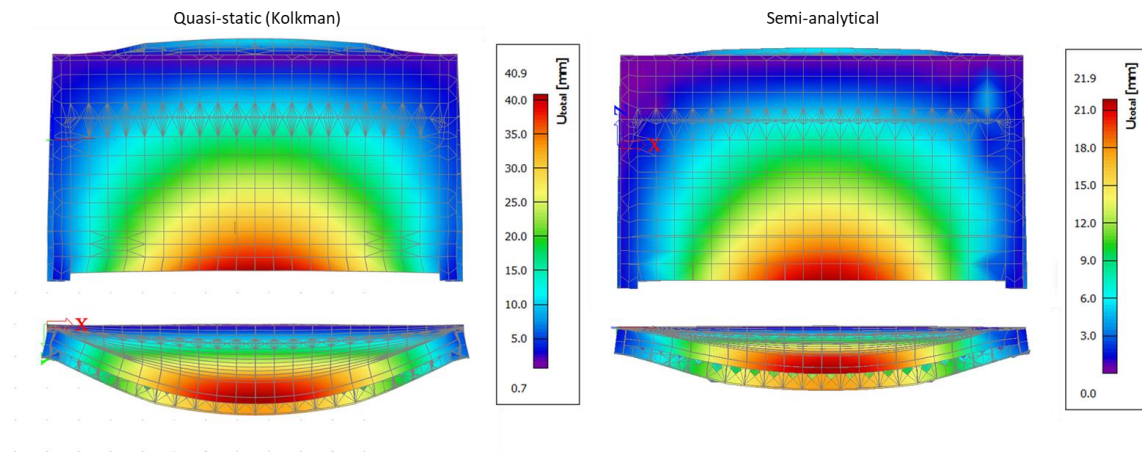
Figure 76. Maximum deflected shapes of quasi-static (right) and semi-analytical method (left).

The same comparison is done with the maximum equivalent stress based on the Huber-Hencky-Von Mises criterion, see Figure 77. The range of both figures is set to a maximum of 355 N/mm^2, which is the yield stress of the material. Both methods show a similar pattern and stress level, but the quasi-static method has its maxima more on the edge where the constraints are located.
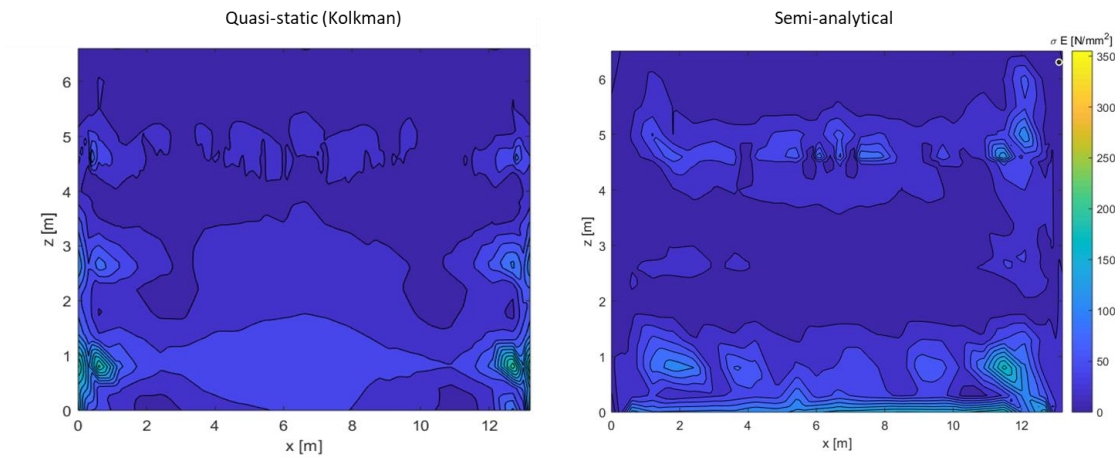
Figure 77. Stress distribution based on the maximum deflected shape of quasi-static (left) and semi-analytical method (right).

The equivalent stress levels are overall rather similar and appear to be lower in the semi-analytical method, which makes sense as the displacement is less. However, the local maximum in the semi-analytical method are higher and more concentrated in the middle of the plate, see Table 6. This can be explained by how the deflected shape is returned to the FE-model. This is done by an evenly spaced grid with a finite spacing. This discrete method can cause a relative rough displacement field resulting in larger stress levels. The spacing can be minimized by applying a finer grid.

Table 6. Maximum local stresses of both methods.

Method	Maximum stress in single node [N/mm^2]
Quasi-static	720.0
Semi-analytical	882.7

7 Parametric Model and Optimization

Linking the FSI-model to a Finite Element Method (FEM) such as SCIA Engineer has two benefits. First the structure is not bounded to a simple rectangular, homogenous and isotropic system with constraints that can be solved analytically but can be as complex as a FEM has to offer. This also means that a fully designed three-dimensional structure can be calculated by the FSI-model, see Figure 78 on the right and in the previous chapter. Secondly it gives the opportunity to develop a parametric model that can optimize the design of a structure to fit the criteria in such a dynamic environment, see Figure 78 on the left. 7.1 gives a description of the parametric model, while 7.2 shows a method in the optimization of such a model using machine learning. The optimization scheme has been developed from the ground-up based on accepted ideas in the world of machine learning.

7.1 Parametric model
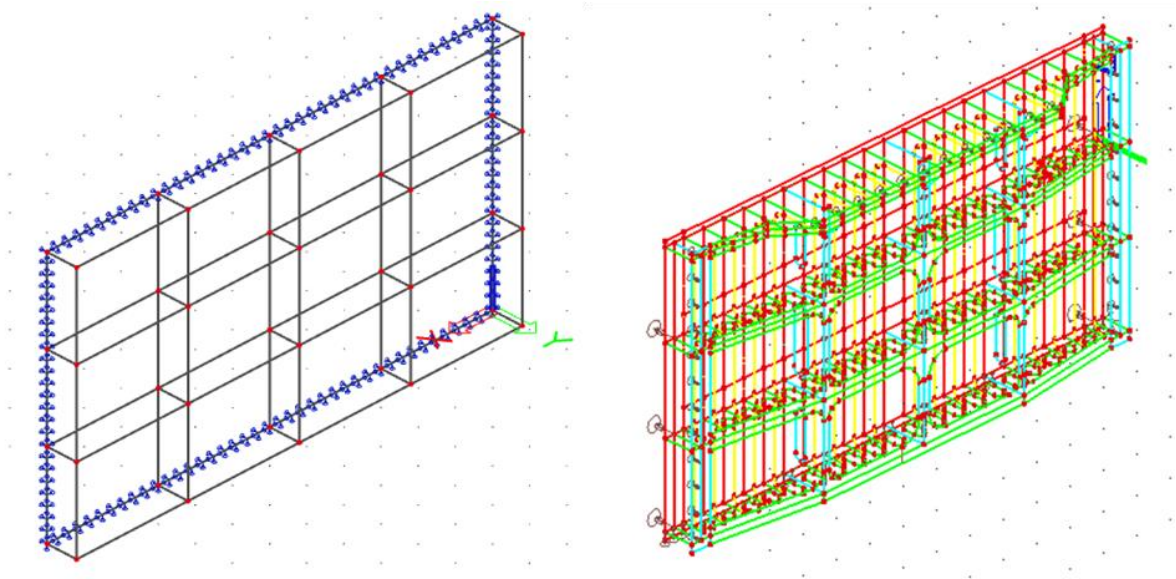
Figure 78. 3D visualisation of the parametric design in SCIA Engineer (left) and of the actual design by Levvel (right).

The parametric design based on the actual design created by Levvel. The basic layout is therefore chosen as a plate with 9 stiffeners in total (4 horizontal and 5 vertical), see Figure 79.
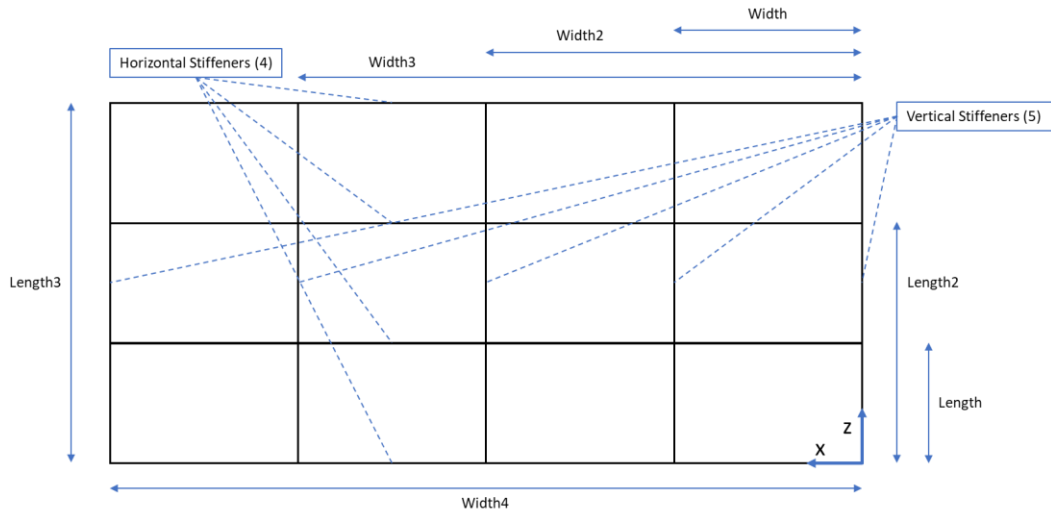
Figure 79. Basic layout of the parameters of the parametric design of the gate.

The location and thickness of each individual stiffener can be changed. The length in y-direction however is for each stiffener equal. The reason is that the stiffeners will only influence the system with their EI (stiffness) and as the thickness is already a variable, length of the rib or flange does not need to be. Furthermore, the translation stiffness of each line constraint at the edges is also variable. This allows each edge to vary between no support (translation stiffness equal to 0) and a simple hinge support with a high translation stiffness. The rotational stiffness cannot become a variable parameter, which is an oversight of SCIA Engineer. This is not a large problem as in all cases the constraints are known and can be simply set permanently in SCIA, however for a sensitivity analysis it could have been helpful. The same logic applies to the total length (Length3) and width (Width4). The total amount of parameters that need to be variable for this case reduces back to 15 with the plate thickness included, see Figure 80. A few parameters have been coupled to lower the number of variable parameters even further to 11, see the numbers in the figure. This improves the calculation time significantly compared to a maximum of 17 variable parameters.
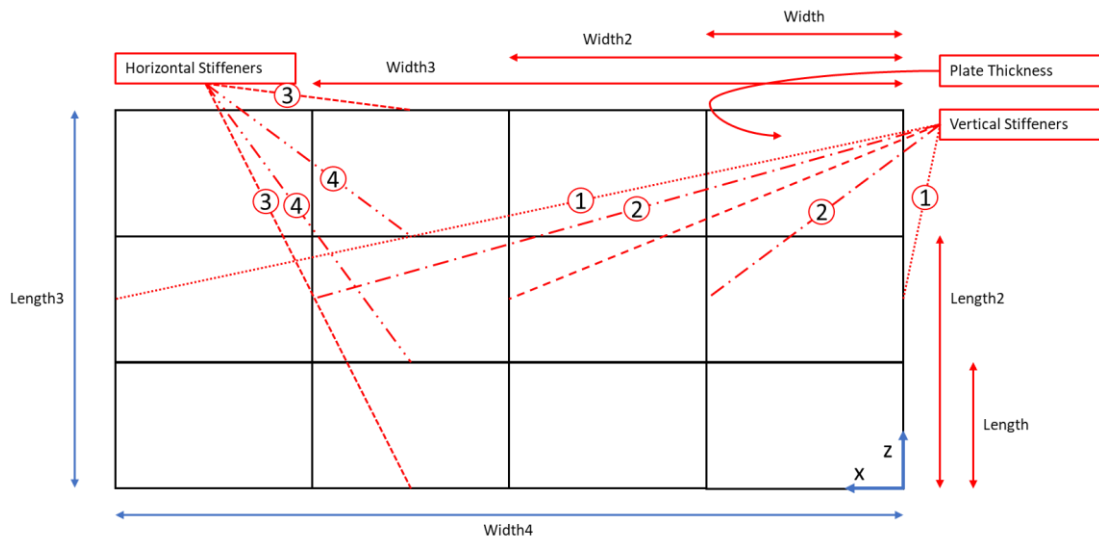
Figure 80. Basic layout of the parametric design showing the variable parameters in red.

The response of the parametric model has been tested with loads that suggest and expected optimal design in Appendix G. This basic test has only been executed on a limited set of the parameters and also concludes that all parameters can have significant importance, especially when the loading

becomes more complex. The next section shows an optimization scheme that allows all parameters to be variable and can result in an actual optimization for this case.

7.2   Optimization

The parametric model has 11 parameters that all contain numerous variants. This large number of variants can no longer be calculated in an efficient manner. Even if each parameter only has five variants each, the total number of possibilities will be equal to 5^{11} or 48.828.125, therefore an optimization scheme is required that can find an optimal design for the case without calculating all these possible variants.
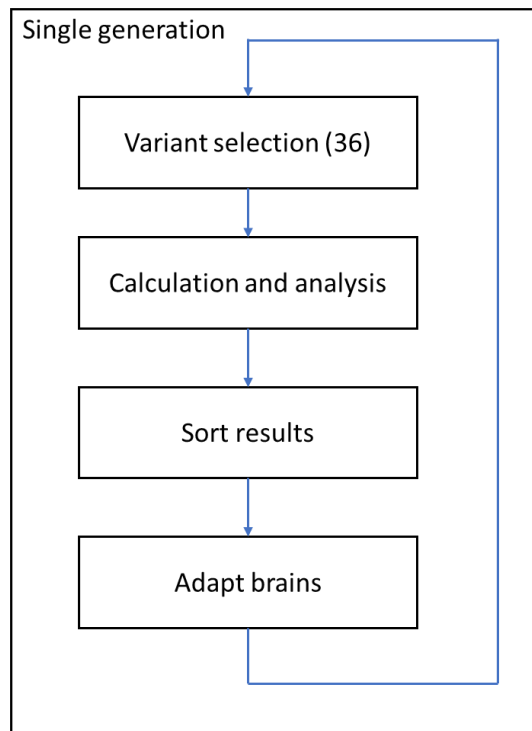
Figure 81. The main process of the optimization scheme.

The method used to overcome this problem is an AI (Artificial Intelligence) based on a combination of neural networks (Rojas, 1996) with a genetic algorithm (Gen & Cheng, 2000). This method is used for machine learning in order to create a faster understanding of a problem. It will not find one single best solution, but it will teach itself how to better understand the problem in order to find acceptable solutions in only a fraction of the time considering the amount of possibilities. The idea is that the variants of each parameter are linked by a probability, see Figure 82. All these probabilities from one parameter to another are grouped in a matrix referred to as 'brains'. The brains in fact represent the synapses or connection between parameters or neurons just like in an actual brain. These brains will adapt by the process shown in Figure 81. The box with 'calculation and analysis' contains the complete semi-analytical model shown in Figure 66.
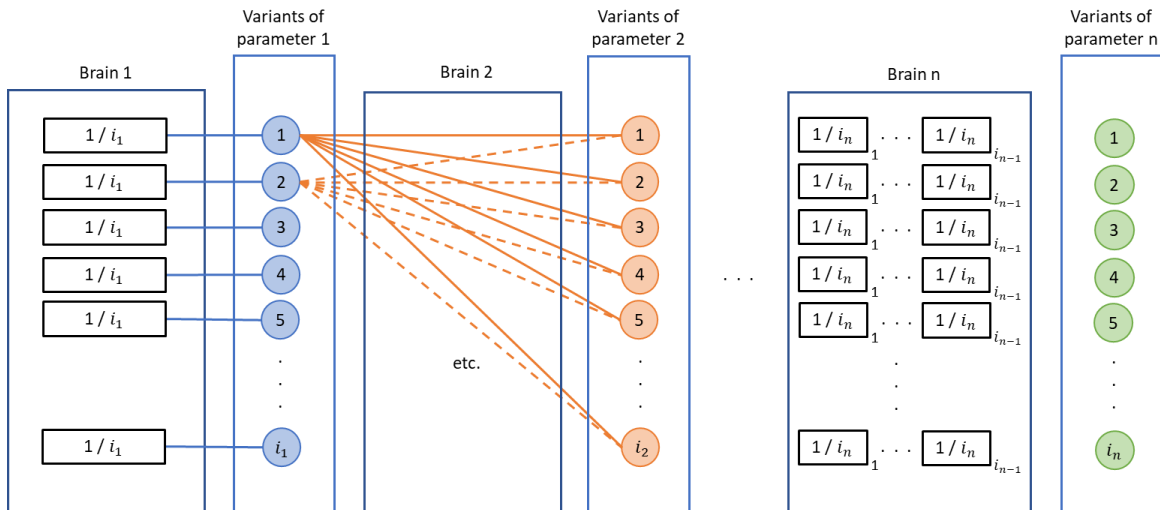
Figure 82. Basic layout of the neural network at the start of the AI scheme.

The process starts at the selection of variants, which is based on the probability of each link. Starting at the first parameter, it will select a variant based on a uniform distribution and will continue from that variant to the next parameter also based on a uniform distribution until the very last one, see Figure 82. The selection of all these variants combined create a unique design that can be analyzed by the FSI-model. However, this procedure will be repeated 36 times before continuing to the calculation and analysis phase. These 36 designs form a single generation and have been created by the same set of brains. 36 designs are needed to ensure that most variants are chosen four times in order to have a fair sorting after analysis. After analysis of the FSI-model the 36 variants will be sorted from best to worst based on a demand. In the case of the gates, the demand is a maximum stress, but could be anything the designer prefers such as a deflection or stress at a certain location. When the designs have been sorted, parts of each brain will be adapted. This is done by increasing the probability of a link between variants of parameters that have produced a good result and decreasing the probability of links that have concluded a relative bad result. These newly adapted brains, which deviate from the uniformly distributed starting position, will then be used in the second generation, where 36 new designs are selected and are more likely to be better suited for the case than the previous generation. The claim for this method is that it only needs to process about 1% of the total variants to reach a satisfactory optimal design. The next section shows a simplified example that provides a positive argument for that claim.

7.2.1   AI example

This section uses a simplified example to establish the quality of the optimization method. The problem in the example is to design a cube with a certain requirement based on volume. The cube is dependent on 3 parameters that determine the volume, see Figure 83.
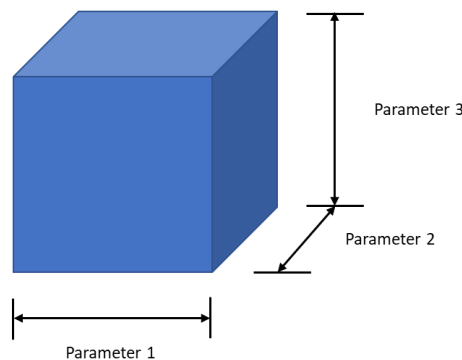
Figure 83. Visualization of the example used for AI.

The previous section explains that after calculation and analysis, which in this example is just simply calculating the volume, the results will be sorted according to the demand. Figure 84 shows how these results are sorted and it also shows that a design is referred to as an 'optimal' design when its result is within 1 % below the demand.
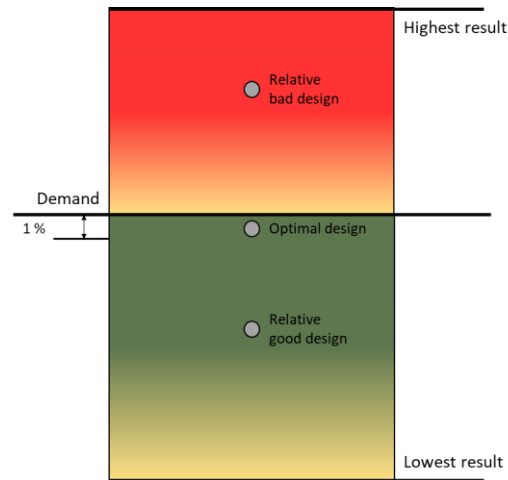
Figure 84. Visualization of how the results are sorted compared to the demand.
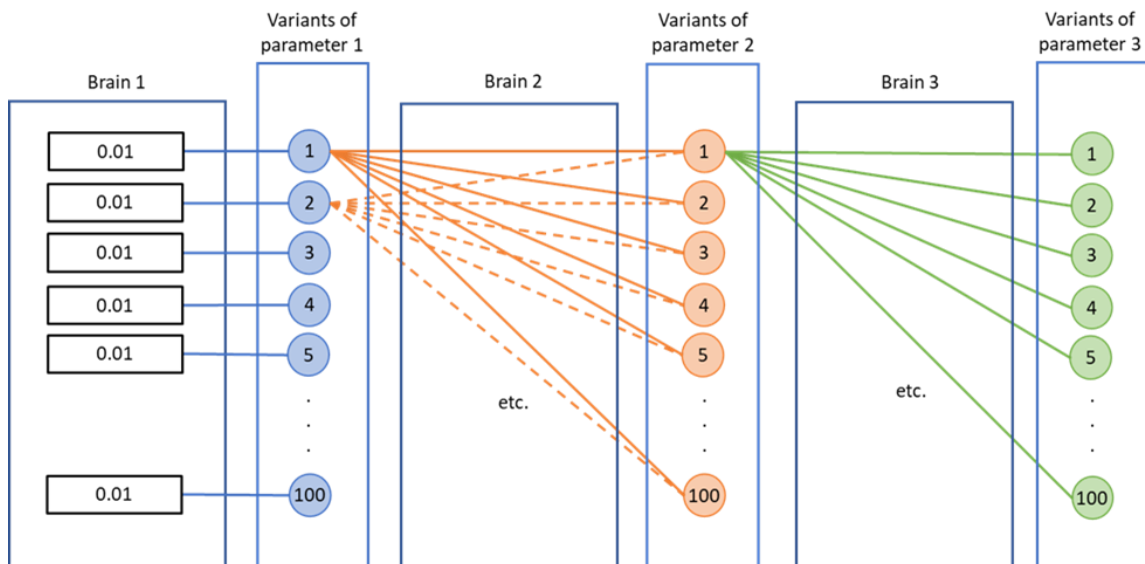
Figure 85. Basic layout of the neural network within the AI example.

In the example each parameter has 100 variants going from 1 to 100, see Figure 85. Together this creates a total of 1 million possible variants. The goal, as mentioned earlier, is to be able to find an optimal solution in 1 % of the total, which in this example would be 10.000. Figure 85 shows the starting point of the analysis of the example, consisting of 3 brains for each parameter and starting with a uniform distribution where each link is equal to 1 over the number of variants per parameter, in this example 100.
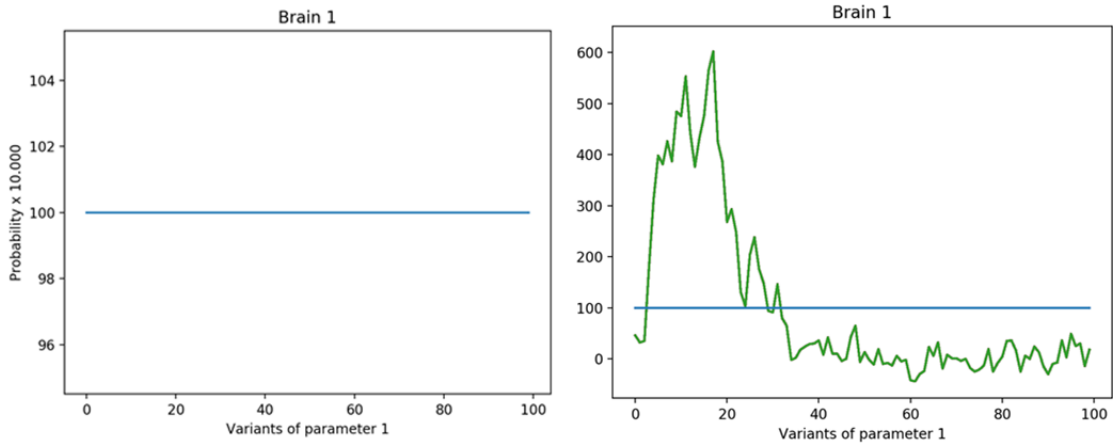
Figure 86. Distribution of the probabilities of the first brain at the start (left & blue) and after 313 generations (1 %, right & green).

At the start of the process each brain is uniformly distributed, see Figure 86 (left). The y-axis shows the probability times 10.000, which makes it possible to add and subtract integers in the software instead of percentiles. The AI selects each variant with the use of the neural network, see Figure 85as explained in the previous section. For this example, a generation consists of 32 designs. The example uses a randomly chosen demand of 81216.373 (43.4 * 42.1 * 44.45). To run 1 % of the total possibilities, 313 generations have to be completed. After these 313 generations the brains will respond accordingly, see Figure 86 (right). The development of the AI is tracked by a success rate. A design is successful as the analysis results in a value below the demand. The success rate is calculated after each completed generation, see Figure 87. The AI functions as expected and can actually increase the success rate from 50 to almost 90 with only 1 % of the total amount of possibilities.
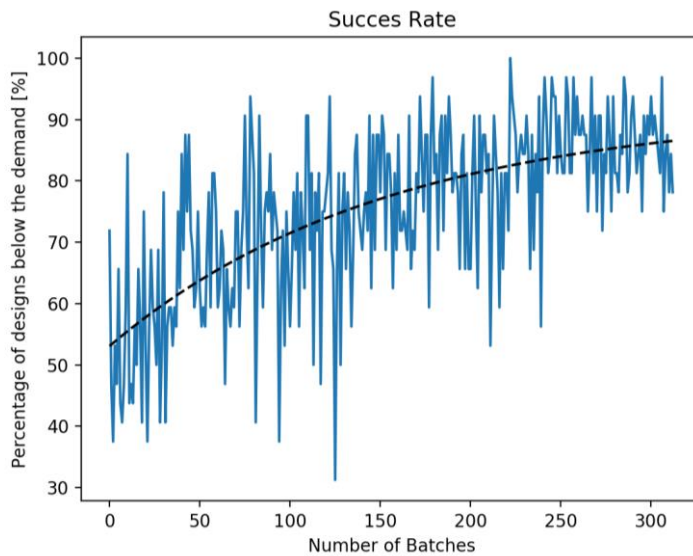
Figure 87. Success rate of example with 313 generations.

Figure 88 shows that indeed between 300 and 400 generations the system convergence and will not improve itself as quickly as before. The reason that it will not reach a success rate of 100 is that the system still contains random variables that can result in a less satisfied scenario.
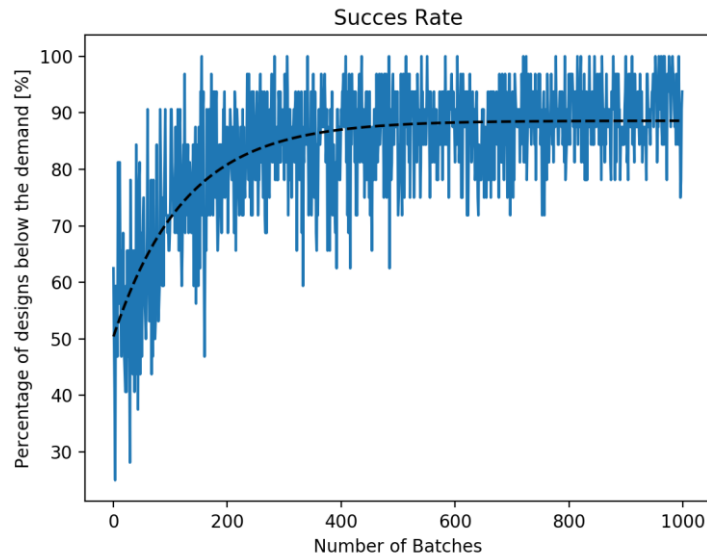
Figure 88. Success rate of an example using 1000 generations (3.2 %)

To test the reliability of this AI based on a neural network, it has been tested with the same input for 20 times, see Figure 89. The output that was used to test the reliability are the optimal designs. The optimal designs are formulated as the designs that have a unity check between 0.99 and 1.0. Meaning that they are within 1 % of the demand, also see Figure 84. The average is about 26 optimal designs in each run. Each run represents the same example and calculates 313 generations. The bandwidth is between 20 and 30 optimal designs. With a consistent average of 26 designs and a relatively small bandwidth, this method can be considered reliable for design purposes.
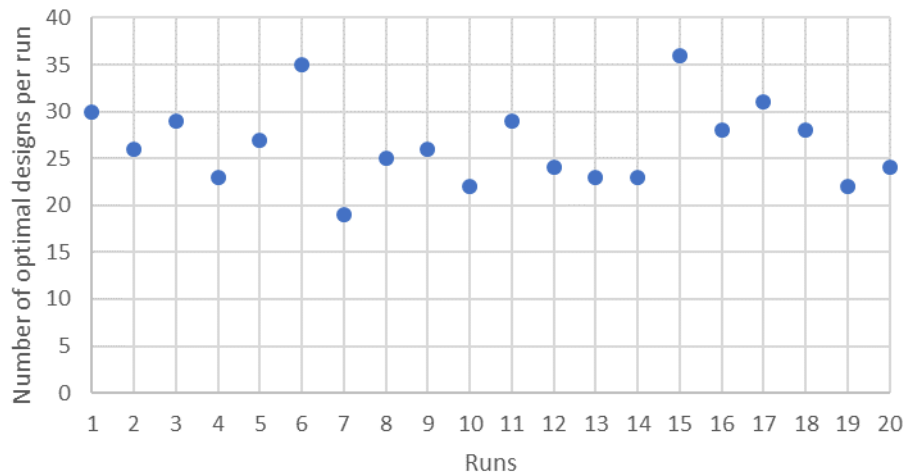
Figure 89. Optimal designs using 313 generations.

7.3   Parametric Model Set Up

Before the parametric model with the optimization scheme can function the values and the number of variants per parameter has to be chosen. Also, the ground rules for the optimization have to established in order to converge to a more optimal design. 5 possible variants per parameter are chosen, see Table 7, making a total of 11^5 different designs. However, designs that have overlapping stiffeners are discarded reducing the total number.

Table 7. Values of all the variants per parameter of the parametric model.

Parameter	Variant 1	Variant 2	Variant 3	Variant 4	Variant 5
Plate thickness	10 [mm]	15 [mm]	20 [mm]	25 [mm]	30 [mm]
Length	1 [m]	2 [m]	3 [m]	4 [m]	4.5 [m]
Length2	3 [m]	4 [m]	4.5 [m]	5.5 [m]	6.5 [m]
Width	1 [m]	3 [m]	5 [m]	6.5 [m]	8 [m]
Width2	3 [m]	5 [m]	6.5 [m]	8 [m]	10 [m]
Width3	5 [m]	6.5 [m]	8 [m]	10 [m]	12 [m]
Vert. Stiff1	5 [mm]	10 [mm]	15 [mm]	20 [mm]	25 [mm]
Vert. Stiff2	5 [mm]	10 [mm]	15 [mm]	20 [mm]	25 [mm]
Vert. Stiff3	5 [mm]	10 [mm]	15 [mm]	20 [mm]	25 [mm]
Hor. Stiff1	5 [mm]	10 [mm]	15 [mm]	20 [mm]	25 [mm]
Hor. Stiff2	5 [mm]	10 [mm]	15 [mm]	20 [mm]	25 [mm]

As seen in the AI example of the previous section 7.2.1, the optimization needs to be controlled by some ground rules. For the example a maximum allowed volume controlled the design, but for the gate design that is more complex. Chapter 2.4 shows three failure mechanism that govern such a gate design, namely yield strength, fatigue and stability. Applying those mechanisms together with the incentive of a design with the least amount of material will most likely result in a realistic and optimal design.

The output of the stress is given at cross-sections made in SCIA. The locations of these cross-sections are at the edges and every meter in both x and z direction for the front plate and at 1 thickness length from the end of every stiffener. Together this results in 386 output points. The equivalent stress, as prescribed in 2.4.1, is given and is sorted according to Figure 90. The demand is determined by the yield strength of the type of steel. Smallest volume is preferred given that the demand is met. When the demand is not met, the design with the stress level closest to the demand is considered better and volume is not considered anymore.
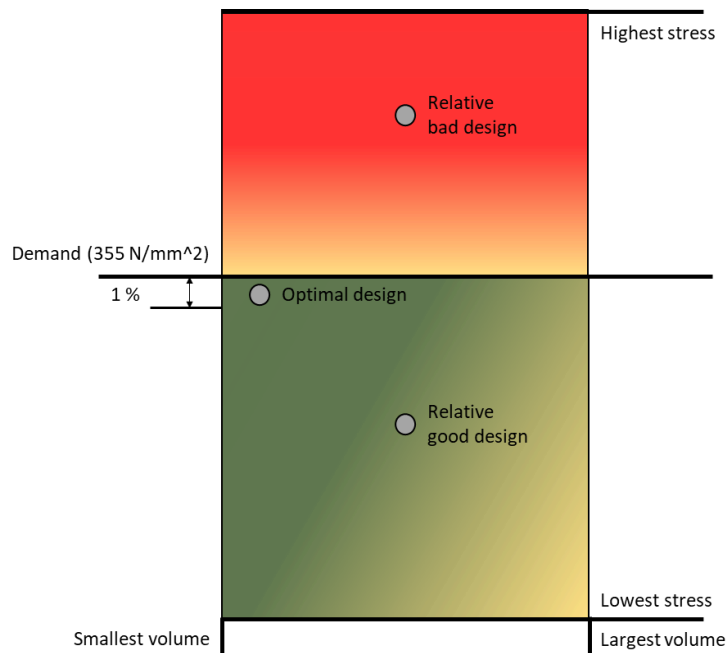
Figure 90. Visualization of how the results are sorted compared to the demand.

This method does not allow for a plastic calculation of the material, which would probably allow a little bit more strength than the yield strength prescribes. This is dealt by not only analyzing the

maximum stress, but also the amount of output locations that show a higher stress level than the demand. If the amount is less than 5%, the maximum stress locations are considered local and could be redistributed by plastic deformation in the surrounding material. 5% is chosen as the output locations are considered to be at locations were those peak stresses would most likely occur as was established in 6.4 by analyzing the resulting stress distribution.

A stability check is performed by analyzing the maximum normal stresses at the locations were the stiffeners are attached to the front plate. The stability check is executed as explained in 2.4.3. The outcome of that analysis is then sorted in the same manner as the stress.

Fatigue can also be checked by analyzing the stress levels at the locations of the welds, however the input for a fatigue calculation requires cyclic loading of various conditions as shown in 2.4.2. This case only contains a single wave impact over a short period. The same set up can be used, but the input should be a representative storm or at least more than one condition.

The optimization is ruled by smallest volume, considering that the stability check and stress demand are met or that the stress demand is only exceeded at certain hotspots. Fatigue can be calculated using this method but requires a different setup which is not part of the scope of this thesis.

7.4 Results

The post-analysis of two generations (first and last) is visualized in Figure 91. The figure shows how the 36 separate designs of a single generation are sorted by the ground rules established in the previous section. The same is done for the stability and together the progress of the network is shaped. The red line symbolizes the yield strength of the material. Clearly visible is that the first generation has a random distribution of designs spread throughout the domain, while the last generation has more designs with similar results. This suggests that system is slowly showing its preference.
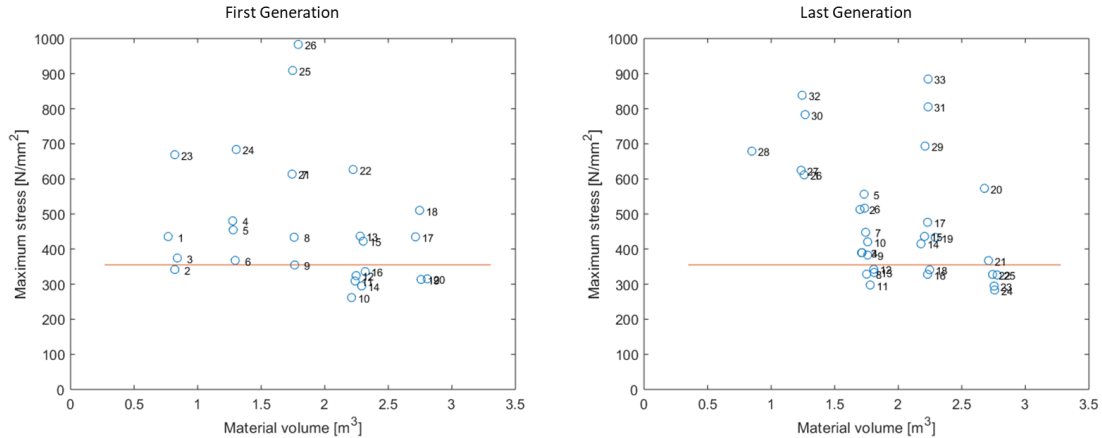
Figure 91. Volume versus maximum stress for first (left) and last (right) generation with numbering sorted from best to worst design.

The network of the brains as shown schematized in Figure 82 is visualized for the first two parameters in Figure 92. The connectivity or link between two variants changes over time as the model progresses. This is envisioned by the thickness of the connecting line, which directly represents the probability of the link. The total probability coming out of a single variant of a parameter always adds up to one. A similar pattern can be distinguished in Figure 92 as is noticed in Figure 91. The tendency of the system in the first parameter is towards the higher end which directly relates to the thickness of the main plate resulting in a larger total volume and overall safer structure.
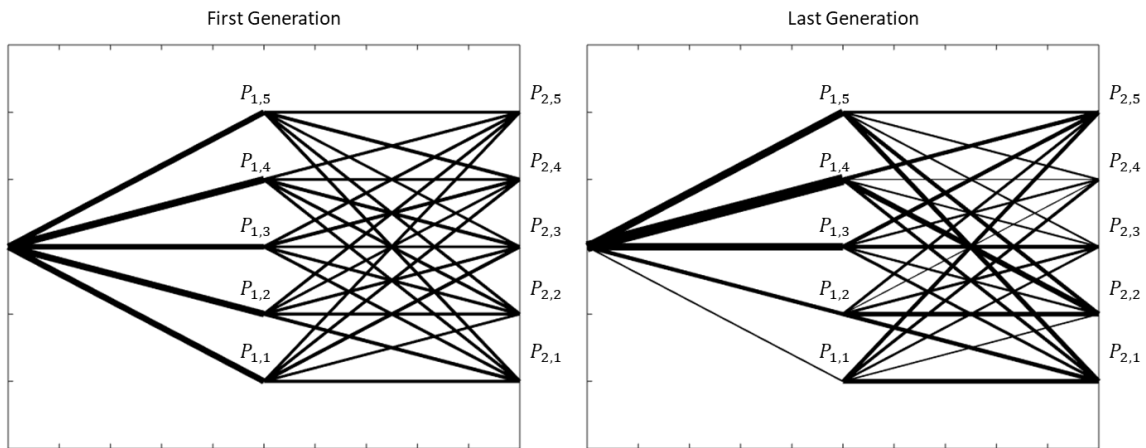
Figure 92. Brain activity visualized for the first two parameters showing the progression of the model.

The final generation, which for this thesis is number 50 adds up to 1800 possible variants analyzed. This does not result in one per cent of the total amount, even with the reduced factor because the design does not allow overlapping elements. This can conclude that the refinement of the brain has not been tuned to perfection but can still give interesting results. Figure 93 already shows the effect of the optimization. The best and worst designs are placed side-by-side with the lowest material volume at the top. The designs are shown with the placement of the stiffeners and thickness of each stiffener. The color and thickness in the figure relate to the thickness in the design, where thick stiffeners are shown in the red spectrum and thin stiffeners towards the blue. The has visual cue system is applied for the thickness of the entire plate by visualizing it in a colored dot that changes in color and size according to the thickness of the plate.
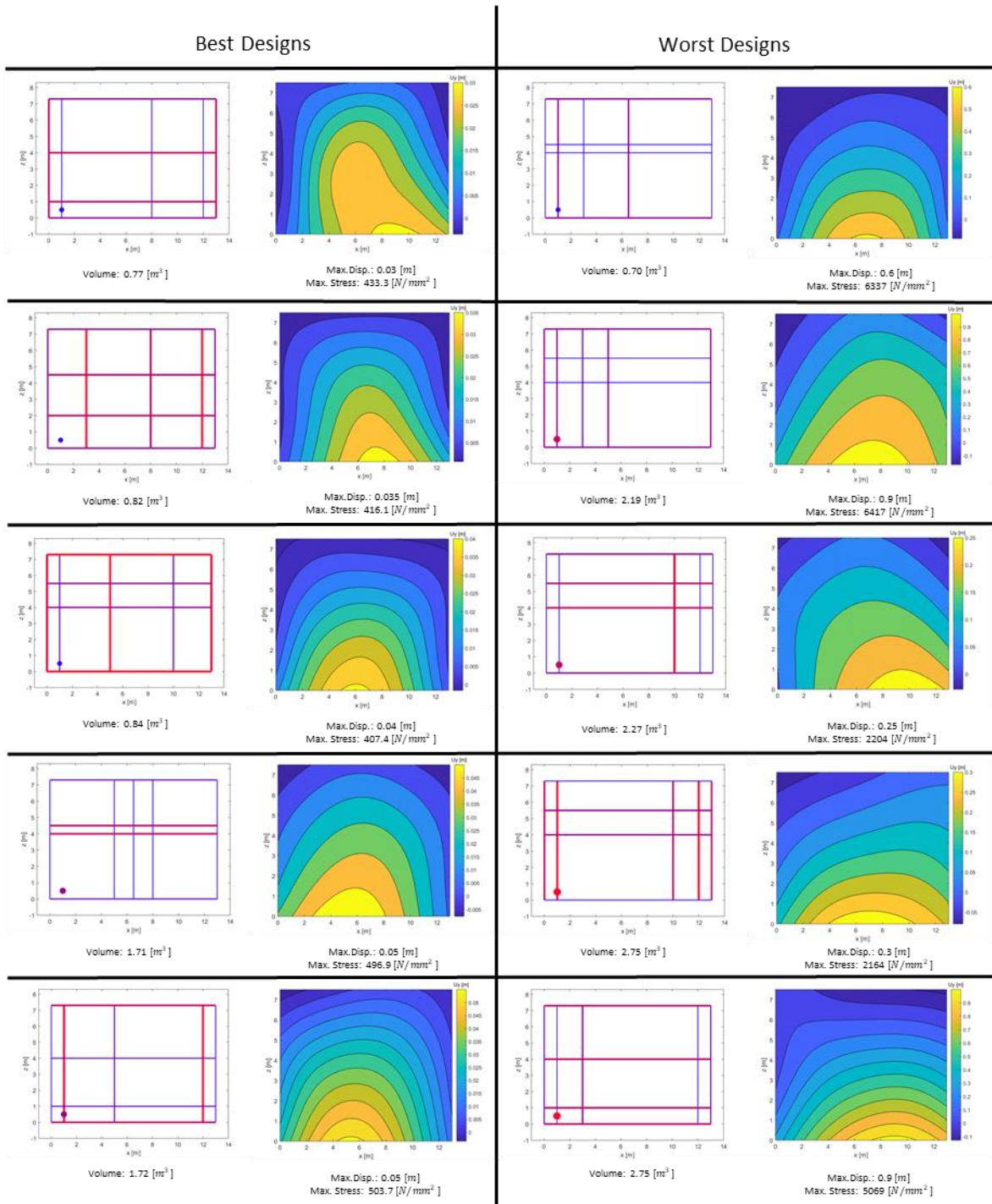
Figure 93. Best (left) and worst (right) designs produced by final generation with displacement field, volume, maximum displacement and equivalent stress.

A good indication that the model functions as expected is that the best designs have more or less evenly spaced vertical stiffeners instead of the irregularity of the worst designs. This is anticipated as the force applied to the system is assumed to be spatially similar in the x-direction. If the force would have a spatially variable in the x-direction as it has in the vertical y-direction, the system would probably respond as shown in the example of Appendix G.

Table 8. Average of modal contributions comparted between best and worst designs.

Type	Mode 1 [%]	Mode 2 [%]
Best 5 Designs per Gen.	69.06	6.26
Worst 5 Designs per Gen.	59.78	10.81

The modal contributions of each design have also been calculated and interestingly it was found that the first mode contributes significantly more to the better designs, see Table 8. This can be related to the fact the first mode requires the least energy to produce for a specific design.
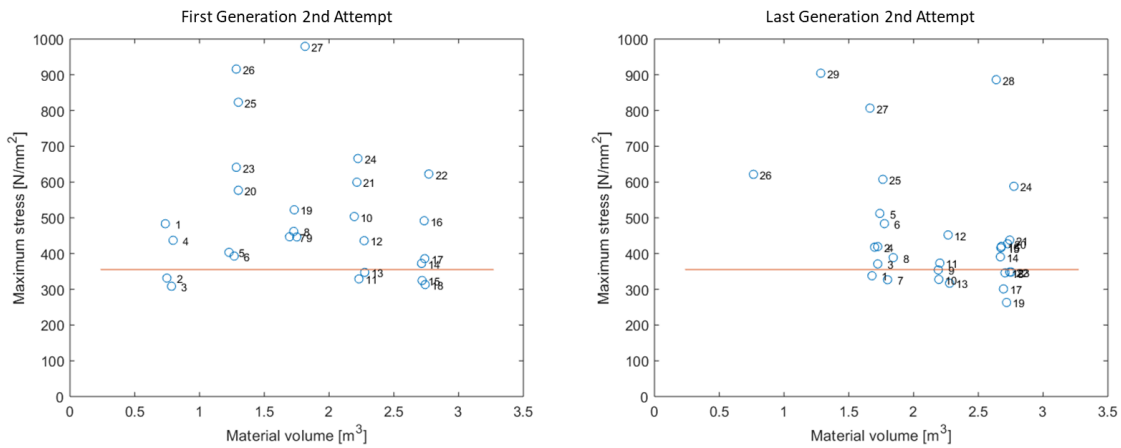
Figure 94. Volume versus maximum stress for first (left) and last (right) generation of second attempt with numbering sorted from best to worst design.

The optimization scheme is executed twice with the exact same set up, to see how robust the system is and actually finds similar results in two different attempts. Figure 94 and Figure 95 show the progress of this second attempt. The figures show the same tendencies as were noticed in the first attempt.
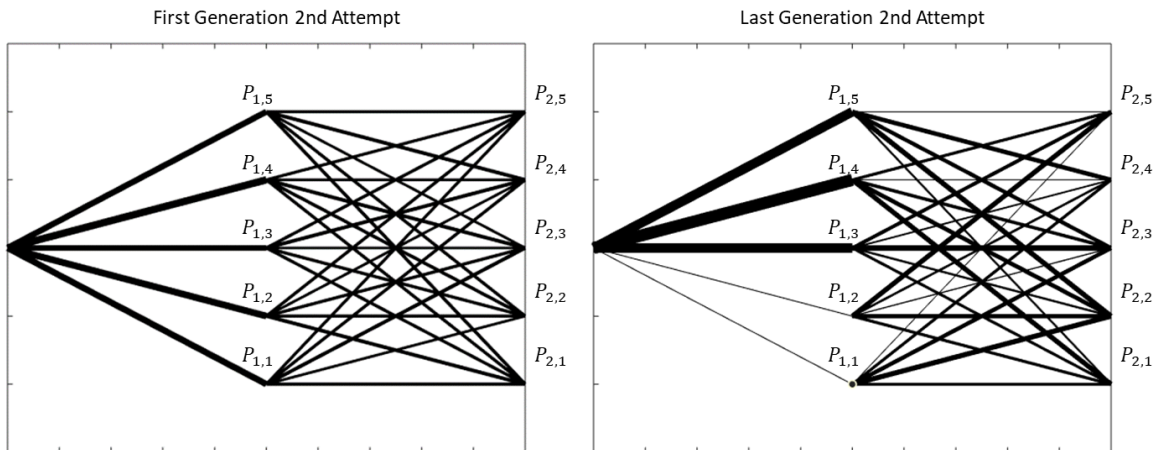
Figure 95. Brain activity of the second attempt visualized for the first two parameters showing the progression of the model.

In Figure 93, the top left design is supposed to be the best design having the lowest material volume and also fulfilling the design criteria. However, it can be easily spotted that the middle stiffener is not centered. As engineer, knowing that the force is equally spaced over the width, centering that stiffener would lead to a more efficient design, see Figure 96.
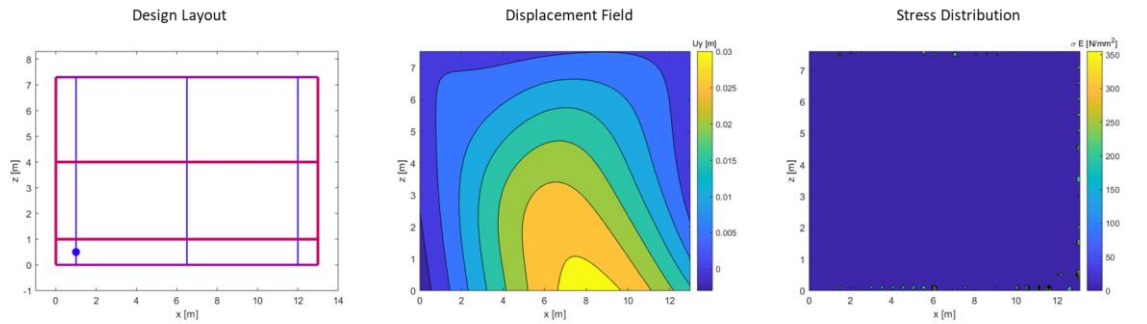
Figure 96. Improved design with displacement field and stress distribution.

The improved design lowers the stress distribution further making it a better design, Table 9. The comparison has also been made with the design by Levvel analyzed with the semi-analytical and quasi-static method. Although, it should be said that the material volume is not a fair comparison as the real design by Levvel also includes fatigue as a failure mechanism.

Table 9. Comparison of analyses.

	Best Design	Improved Design	Semi-analytical	Quasi-static
Maximum Displacement [m]	0.03	0.03	0.02	0.04
Max. Stress [N/mm^2]	433.3	356.7	882.7	720.0
Material Volume [m^3]	0.77	0.77	4.68	4.68

8   Conclusions and Recommendations

This chapter discusses the conclusions found in this research and thereby answering the research questions stated in 1.3. The three main research questions are discussed in the same order as were given in chapter 1.3. The second part of this chapter contains recommendations for model tests that give more insight in methods used in this thesis and also the more general application of generative artificial intelligence in engineering design processes.

8.1   Conclusions

As mentioned in the previous segment, the conclusions are constructed by answering the research questions in order.

8.1.1   Wave Impact Pressures

In Chapter 5, a numerical alternative based on a notion from theoretical research done by Wood and Peregrine (1996) is developed and analyzed. Their notion was to find the pressures by directly calculating the pressure impulse field. The motivation came from how the hydraulic boundary conditions were established for the new Afsluitdijk project. A relative expensive model test was executed (Hofland, 2015) to find the design conditions, because an overhanging structure caused relative low water levels and waves to be governing. The numerical method developed in this thesis seems to capture the physical properties measured by the model test but is only verified on that single test, however it looks promising compared to the current alternative. The numerical method can also be applied to predict the pressures when gaps are introduced also in three dimensions. These gaps are actually recommended when using the numerical method as it eliminates the interference of air pockets as much as possible. For better understanding and verification, a new model test is recommended, see 8.2.2. Chen et al. (2019) elaborates on this subject by splitting the quasi-steady and impulsive components of the impact force. This allows for statistical analysis and can be used to predict the total load much more accurate. This is very important as was shown in 3.3 and 5.4 that the effect of the duration ('Ts') of the impulsive component is significant and poorly understood.

8.1.2   Method Comparison

Chapter 6 shows clearly that the two methods (quasi-static and semi-analytical) create similar results. The fact that the semi-analytical approach is based on a full dynamic calculation also considering the dependency of each analyzed frequency should reveal that the other method renders obsolete. It can be said that the semi-analytical approach is closer to reality in this case. However, it is still difficult to apply such a complex analysis to an intricate three-dimensional design. This thesis utilizes a FE-model to overcome this problem, by linking it to the semi-analytical model. This brings interesting possibilities in the application of the method and does not conform to the complexity of the structure or its boundaries anymore. Appendix I shows that when calculating the equivalent thickness of the gate in order to apply the semi-analytical method with a homogeneous isotropic plate it cannot be considered thin anymore. This also interferes with the further calculations of the deflection and stress, resulting in an unrealistic representation. The use of a FE-model in combination with the semi-analytical method results in an adequate system that is not bounded by simplistic geometry and is therefore most suitable for such dynamic problems.

8.1.3   Parametric Model

The combination of the relative quick analysis of the semi-analytical model and the incorporation of the FE-model rendered the possibility of creating a parametric model. The parametric model is coupled with an optimization scheme based on neural network combined with a genetic algorithm. With predefined rules and boundaries, set by the user, the model will optimize to find the best designs. Chapter 7 explains the reasoning behind the model. The model can be used for preliminary designs and should give engineers more understanding in the behaviour of their dynamic problem. It

can be used to access possibilities in an early stage that as of today is not reasonable due to time constraints. The model cannot yet be used for a final design as the complexity in the design is fairly low as well as some failure mechanisms are still left out.

8.2   Recommendations

The recommendations that have come from this thesis are divided into three main sections. First adaptations to the semi-analytical model to take away more limitations, then some model tests are recommended to verify the applied models in this thesis. Finally, the applications of adaptive structural design algorithms are given showing the possibilities when designing such complex structures.

8.2.1   Extra Fluid Domains

The addition of using a FE-model to find the modal shapes of a structure such as the discharge sluice gates at the Afsluitdijk greatly enhanced the complexity of the structural part of the semi-analytical method. To increase the complexity of the fluid part as well, different domains can be added. As shown in Chapter 5 the boundaries have great influence in the pressure distribution in the water column. By applying extra fluid domains containing those boundaries, these effects can also be implemented in the semi-analytical method. An example of the application of such an extra fluid domain is shown in Figure 97. Top boundary of the added domain is similar to the bottom boundary and the domain needs a fluid-fluid interface condition, resulting in two extra waves in the system.
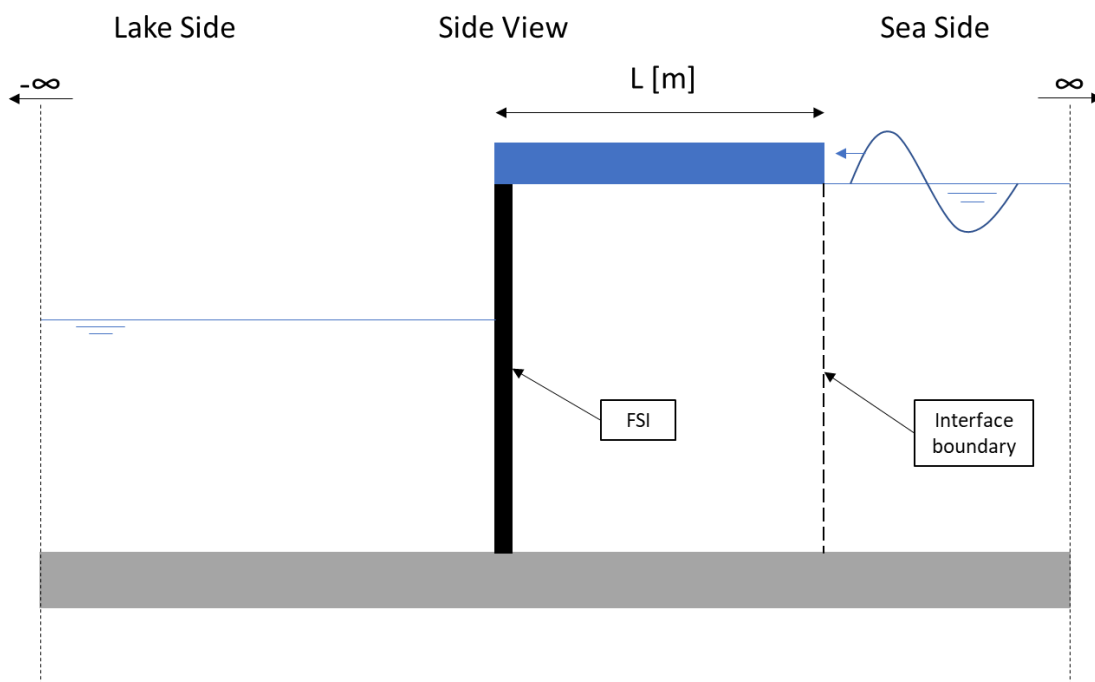
Figure 97. Model schematization of fluid system with partial overhang.

Earlier studies (Versluis, 2010) found that the hydrodynamic pressures are not significantly affected by a second structure with L > 4 * h, where L is the length of the sluice or lock and h is the water level. This means that for larger lock chambers the length can be considered infinite in the model. This is also the case for a lock head, where the sluice opens out to the sea or lake. The effect of this relative infinite space is considered negligible when the length is less than 4 times the water level. However, the effect can be included with the addition of an extra fluid domain as seen in Figure 98.
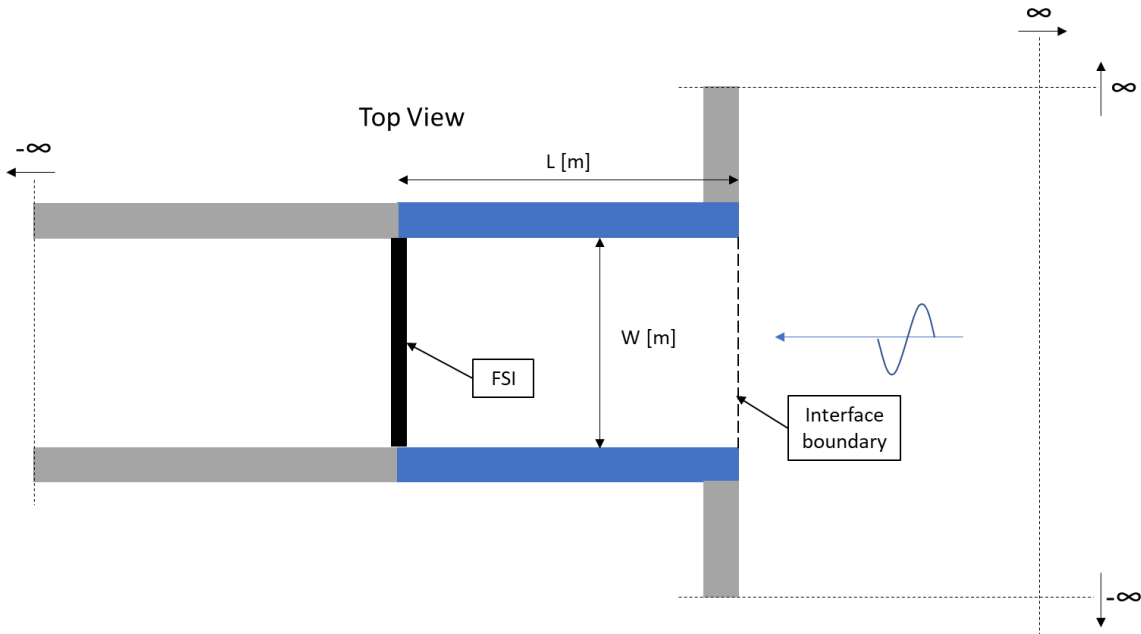
Figure 98. Model schematization of a sluice with a limited length.

8.2.2 Model Test

As a result of the numerical method prescribed in Chapter 5, a model test should be recommended. This method is only verified by a single test that was executed with a different goal. It would be interesting to see the effect of the gap length in the overhanging structure as well as a gap between the gate and the overhang in the vertical direction. As mentioned in Chapter 5, to verify the numerical method, it is advised to always apply some gap to avoid air pockets as much as possible.

To see the effect of the dynamic response of partially submerged plates in water, another test is recommended. A thin plated structure with some stiffeners as shown in this thesis that is able to respond to wave impacts in a controlled environment. The response should be measurable as it would be interesting to see if the expected modes are actually visible in the measurements. The parametric model described in this thesis can be used to find designs that will vibrate significantly in higher modes due to the wave impact, which would be known in a controlled environment.

8.2.3 Artificial Intelligence in Structural Design

The application of using AI in structural design is probably difficult to grasp as many parameters and mechanism play a role. This has been proven in this thesis by showing the complexity of such a problem. However, this might also be the reason to apply such automotive systems into the equation. Especially in designs were a dynamic problem is governing. Most of times it is unknown to find the leading parameters that produce an efficient design, which results in many attempts by different engineers without knowing the exact source of the problem. Computers can aid in these situations by analyzing a larger quantity of designs in a more efficient way. As well as analyzing the choices that affect the efficiency. The final adaptation of the best design according to the parametric model in 7.4 is a good example. The computer found relatively fast a design better suited than the engineers, however with a quick glance this design could be improved even further as the algorithm is designed to coexist with the current engineering intellect.
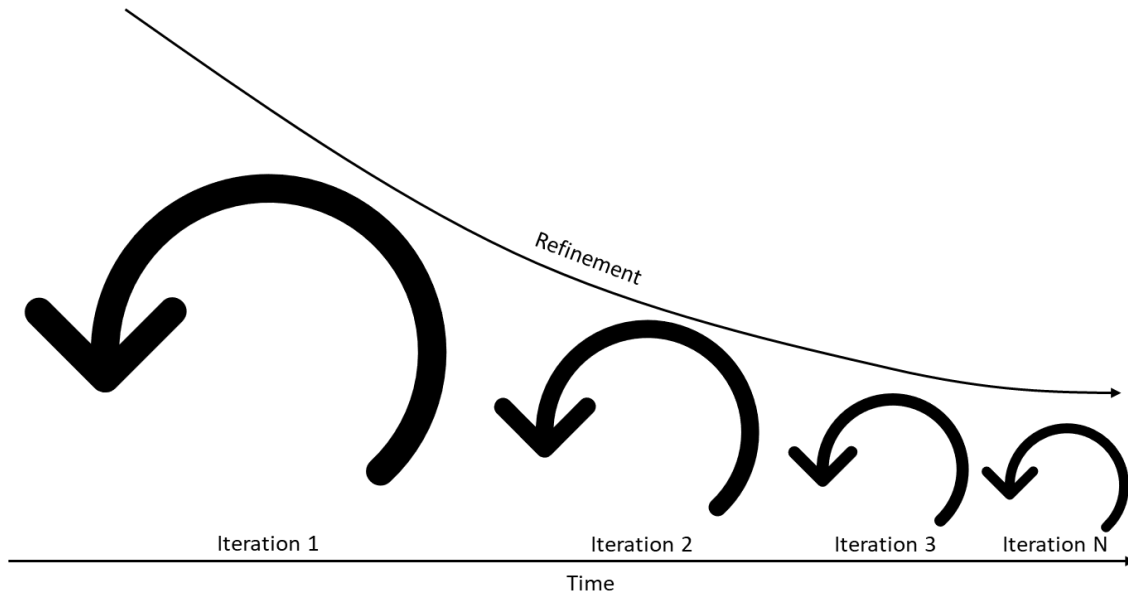
Figure 99. Simplification of the design process.

The reason the AI in this thesis was based upon a neural network with a genetic algorithm is that it simulates the design process. Figure 99 represents a simplistic model of the design process where with every iteration the design is more refined but will never reach perfection. The engineer simply starts at a certain assumption, where the AI starts at a parameter. To recreate this iterative process creates a highly intelligent and quick assistant that can guide the engineer to a more efficient design. The AI is in a generative state. Meaning that it can reshape information within a preset domain. A passive AI only does what its user selects, but a generative AI can find its own solution from a set of generic ground rules. One step further would be an intuitive AI which can reshape its own ground rules.
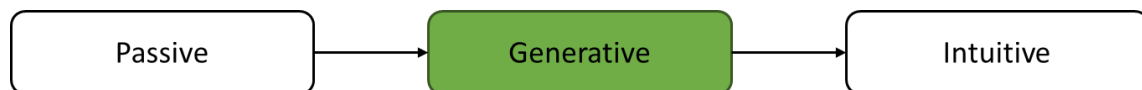
Figure 100. State of artificial intelligence.

For this thesis the boundaries were partially determined by towers containing the lifting mechanisms, however when eliminating these boundaries and allowing the AI to determine the width and height of the gate itself. Also factoring in the costs of the concrete towers and upkeep. In a preliminary phase, this could result in a completely alternative design that could possibly be much more cost efficient, see Figure 101 for possible alternatives. The coupling with a FE-model provides these possibilities and should be investigated in future research.
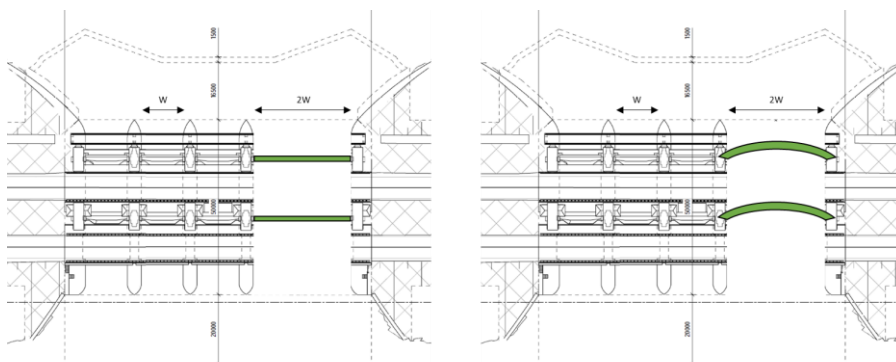
Figure 101. Alternative designs for the lifting gates at the Afsluitdijk.

When allowing different shapes to be generated, it could even be taken a step further, which would never be possible with people and passive software. For example, Airbus in collaboration with Autodesk used generative AI to design a panel in one of the plane models to have the same strength but with less weight, see Figure 102. This design is very complicated to produce and does not fit the current manufacturing process, which makes the method very difficult to implement in civil engineering applications. However, when given the correct design restrictions as shown in this thesis, it could very well be applied in many situations.
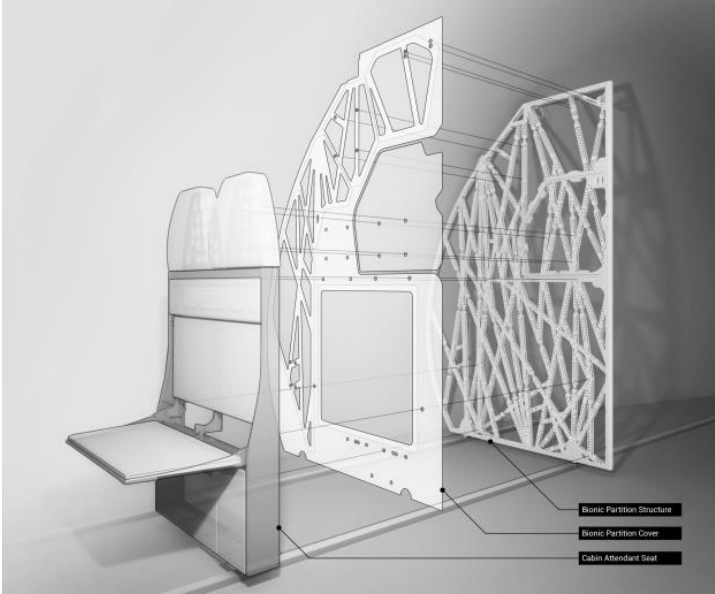
Figure 102. Example of a design by generative artificial intelligence (Schaefer, 2019)

The application of the model introduced in this thesis can be exported to any type of plate or shell structure in a dynamic load environment. Examples of such structures are bridges, where the traffic is the main dynamic load, or a roof, where the wind or earthquakes play a role.

9 Bibliography

Bagnold, R. A. (1939). Interim report on wave pressure research.

Belfroid, S. (2017). *Literature search on screening for flow-induced vibrations on hydraulic gates.*

Canny, K. A. (2018). Seismic response of liquid storage tank in a semi analytical method. *TU Delft*.

Chen, X. (2019). *Use of impulses to determine the reaction force of hydraulic structures with an overhang due to wave impact.*

Cichanski, A., & Sempruch, J. (2005). Experimiental method of defining biaxial fatigue properties of elastic-plastic construction materials. *Journal of Theoretical and Applied Mechanics*.

Cooker, M. J., & Peregrine, D. H. (1995). Pressure-impulse theory for liquid impact problems. *University of Bristol*.

Eurocode 3: Design of steel structures (EN 1993). (2005). Brussels.

Gen, M., & Cheng, R. (2000). *Genetic Algorithms and Engineering Optimization.* New York: John Wiley & Sons.

Gomez, C. P. (2014). Dynamic behaviour of large hydraulic structures in FRP. *TU Delft*.

Groeneweg, J. (2013). Hydraulische randvoorwaarden voor het ontwerp van de versterking van de afsluitdijk. *HKV & Deltares*.

Hofland, B. (2015). *Modeltesten golfkrachten spuisluizen Afsluitdijk.* Deltares.

Hofste, G. M. (2012). Stevin Outlet Sluices, Wave impact under a beam. *TU Delft*.

Howison, Ockendon, & Wilson. (1991). Droplet impact on a thin fluid layer. *Mathematical Institute*.

Kisacik, D. (2014). Investigation of uplift impact forces on a vertical wall with an overhanging horizontal cantilever slab.

Kolkman, P. A., & Jongeling, T. H. (2007). *Dynamic behaviour of hydraulic structures part A.* Delft: Delft hydraulics.

Kolkman, P. A., & Jongeling, T. H. (2007). *Dynamic behaviour of hydraulic structures part B.* Delft: Delft hydraulics.

Kolkman, P. A., & Jongeling, T. H. (2007). *Dynamic behaviour of hydraulic structures part C.* Delft: Delft hydraulics.

Kortenhaus, A., & Oumeraci, H. (1998). Classification of wave loading on monolithic coastal structures. *TU Braunschweig*.

Leon, S., Bjorck, A., & Gander, W. (2013). Gram-Schmidt Orthogonalization: 100 years and more.

Lundgren, H. (sd). Wave shock forces: an analysis of deformations and forces in the wave and in the foundation. *Technical University Denmark*.

Naudascher, E., & Rockwell, D. (1994). *Flow-induced vibrations.*

O'Leary, P., & Harker, M. (2010). Discrete Polynomial moments and Savitzky-Golay Smoothing. *Waset Special Journal*.

Rojas, R. (1996). *Neural Networks, A Systematic Introduction.* Berlin: Springer-Verlag.

Schaefer, B. (2019, February 10). *Airbus*. Retrieved from Autodesk: https://www.autodesk.com/customer-stories/airbus

Shankar, S. (2012, September). *2D Laplace equation.* Retrieved from mathworks: https://nl.mathworks.com/matlabcentral/fileexchange/38091-2d-laplace-equation?s_tid=prof_contriblnk

Soedel, W. (2005). *Vibrations of Shells and Plates.* Purdue University.

Standard Practices for Cycle Counting in Fatigue Analysis. (1997). *American Society for Testing and Materials*.

Thijsse, J. T. (1972). *Een Halve Eeuw Zuiderzeewerken.*

Tieleman, O. C. (2015). The dynamic behaviour of pump gates in the Afsluitdijk. *TU Delft*.

Tieleman, O., Tsouvalas, A., Hofland, B., Peng, Y., & Jonkman, S. (2018). *A three dimensional semi-analytical model for the prediction of gate vibrations immersed in fluid.* Marine Structures.

Tsouvalas, A., & Metrikine, A. V. (2016). Structure-borne wave radiation by impact and vibratory piling in offshore installation: from sound prediction to auditory damage. *TU Delft*.

Tsouvalas, A., Dalen, K. N., & Metrikine, A. V. (2015). The significance of the evanescent spectrum in structure-waveguide interaction problems. *TU Delft*.

Tsouvalas, A., Dalen, K. v., & Metrikine, A. (2015). *The signigicance of the evanescent spectrum in structure waveguide interaction problems.* Journal of the Acoustic Society of America.

Tsouvalas, A., Metrikine, A. V., & Jung, B. (2012). A semi-analytical model for predicting the levels of underwater noise from offshore pile driving. *TU Delft*.

Veldhuizen, J. C. (2017). Flow-induced vibrations of fibre-reinforced polymer hydraulic gates. *TU Delft*.

Versluis, M. (2010). Hydrodynamic pressures on large lock structures. *TU Delft*.

What-percentage-of-the-Netherlands-population-actually-lives-above-sea-level. (2018, August 10). Opgehaald van quora: quora.com/What-percentage-of-the-Netherlands-population-actually-lives-above-sea-level

Witteveen+Bos. (2013). *Startdocument planuitwerking Afsluitdijk.* Rijkswaterstaat.

Wood, D. J., & Peregrine, D. H. (1996). Wave impact beneath a horizontal surface. *University of Bristol*.

A The Afsluitdijk

A.1 History

As known by many, the Netherlands is a low-lying country that has been battling through the ages with the water to survive. Each flood has left a scar on the land and on its people. These disasters made them inventive to create defensive structures. No wonder that the plan to close off the Zuiderzee has been around from as early as the 17th century. The large inlet was the largest threat to the coast of the surrounding low lands, which were so important for the nation's prosperity. Hendric Stevin, who was the son of famous physicist and mathematician Simon Stevin, suggested in 1667 that the danger of flooding could be avoided if the Zuiderzee is closed off from the Noordzee by a manmade barrier. The plan was taken seriously, however the available resources and technology of the time made it unrealizable. The hydraulic engineer who was finally able to succeed is named Cornelis Lely and did it almost 300 years later.

A.1.1 Zuiderzeewerken

Cornelis Lely and Hendric Stevin were not the only ones to come with plans for the closure of the Zuiderzee. Many more had similar or even more outrageous plans for the defensive structure of the nation. The reason that so many engineers had created a plan was that their plans did not only contain a defensive motive against flooding, but also a motive to expand and boost the nation's economy. The Zuiderzee was in in most areas no deeper than 2 to 5 meters with rich soils containing peat and clay as top layers. This is suitable for land reclamation as it is relatively easy to drain and has a good surface for agriculture once it is dry. The first figure of Figure 103, designed by Van Diggelen, shows one of the more outrageous plans to maximize the land reclamation of the Zuiderzee.
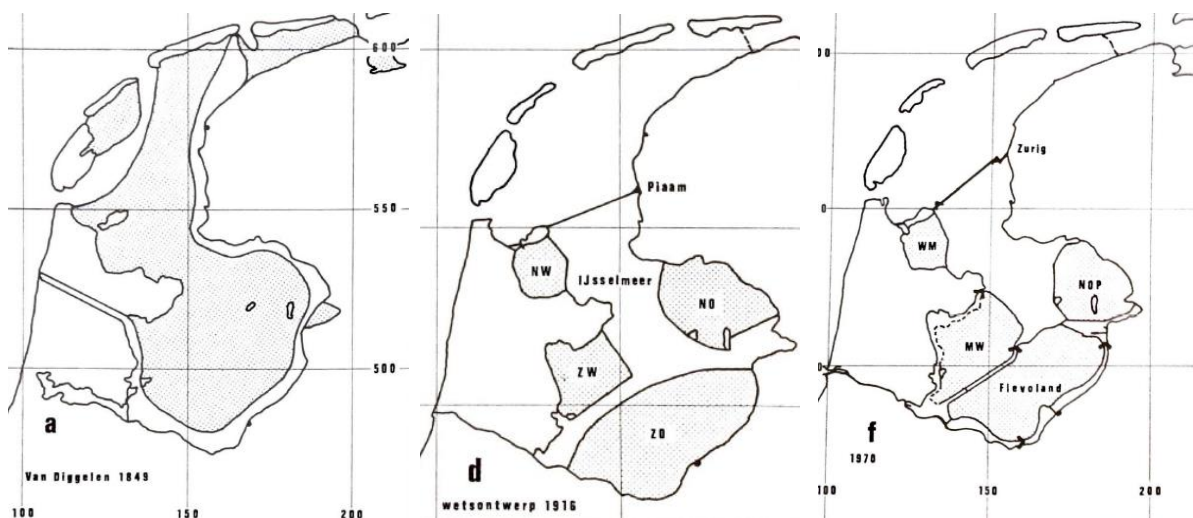
Figure 103. From left to right. Plan Van Diggelen from 1849, Plan Lely from 1916 and the final plan at start of construction [18].

Van Diggelen's plan has two major flaws. First the outflow of the rivers IJssel and Vecht are blocked, which means they have to be diverted in order for the plan to function. Secondly the amount of land reclamation. The area is so large and although it does not cut through the deepest areas of the Waddenzee it is still extremely expensive. The land reclamation in the Waddenzee is in later plans discarded as more land equals to more expenses. The soil of the Waddenzee is also mainly sand, which means that agriculture would not be productive in this area. Nowadays we would not dare to reclaim the Waddenzee, but in those days the priorities were somewhat different.

It took Cornelis Lely almost his entire professional career, with multiple times appointed as minister of water, to get the project started. The main catalysators for the start of the project were the food

shortage during WWI and a large flood of the Zuiderzee area in 1916. Both indicating separately the two problems that could be solved with the Zuiderzeewerken. July the fifth of 1918 marks the official start of the closure and land reclamation of the Zuiderzee. On this day Queen Wilhelmina signed the law, making the closure a top priority in the nation.

As can be seen in the comparison between the middle and right figure of Figure 103, some design changes were made before the actual start of construction, which took place in 1920. There were a lot of uncertainties with the engineers that needed to be clarified. At first it was believed that the sediment arriving with the river IJssel would fill up the newly formed lake. It was measured and calculated that it would take some generations before some problems might occur. Now we know that the discharged water at Den Oever and Kornwerderzand have an equal sediment percentage as the water flowing into the IJsselmeer. Also, it was believed that the because of the closure of the Zuiderzee, the water of a flood would flow towards the dikes of Friesland and Noord-Holland making them unsafe. All these uncertainties gave rise to a technical committee, who would be charged of tackling these problems. The famous physicist Lorentz had made himself available for the position of chairman, which is why the committee is referred to as 'Staatscommissie Lorentz'. One of the most important acts of the committee is to relocate the Afsluitdijk more North to Zurich instead of Piaam in order to reduce the resonance effect of the tidal wave, which could increase flow velocities at the Texelse Zeegat. They also established the newly expected water levels during a storm at many locations around the Waddenzee, so that these dikes could be strengthened in relation to the new situation.

Figure 104. From left to right. Situation of the Zuiderzee in the 19th century. Situation of the Zuiderzee after construction in 1970 (Thijsse, 1972).

Figure 104 shows all the works done during the entire project minus the Houtribdijk, which was completed after this map was created. The reason that the Afsluitdijk has a small kink at its Eastern end at Kornwerderzand is because there was a natural tidal channel called Middelgronden. It was thought to be easier to construct the Afsluitdijk perpendicular to this deep natural channel in order to

travel the smallest distance across it. At this location, Kornwerderzand, shipping locks and discharge sluices were built. The same was done at the Western end at Den Oever. Two of each construction was thought to be necessary for military motives. If one complex would be destroyed during a war, the other one would still be functional without crippling operations too much.

A.2　　　　Discharge Sluices

Two discharge sluice complexes are located at either end of the Afsluitdijk. These are needed to drain the water from the IJsselmeer into the Waddenzee. This can only take place at low tide when the water in the Waddenzee is much lower than in the IJsselmeer. The IJsselmeer is filled by water flowing in from the river IJssel. The gates at the discharge sluices will simply open by vertical lift and the water naturally flows out to the Waddenzee due to a head difference.

A.2.1　　　　Design of Discharge Sluice Complex at Den Oever

There are five complexes like the one shown in Figure 105, two at Kornwerderzand and three at Den Oever. Each discharge complex works similarly and will open mostly two times a day. As can be seen in the figure below the heart-to-heart distance of the pillars is 16 m while the width of the opening is 12 m. The shape of the inlet has effect on the flow and waves coming into the structure and should be considered with further analysis.
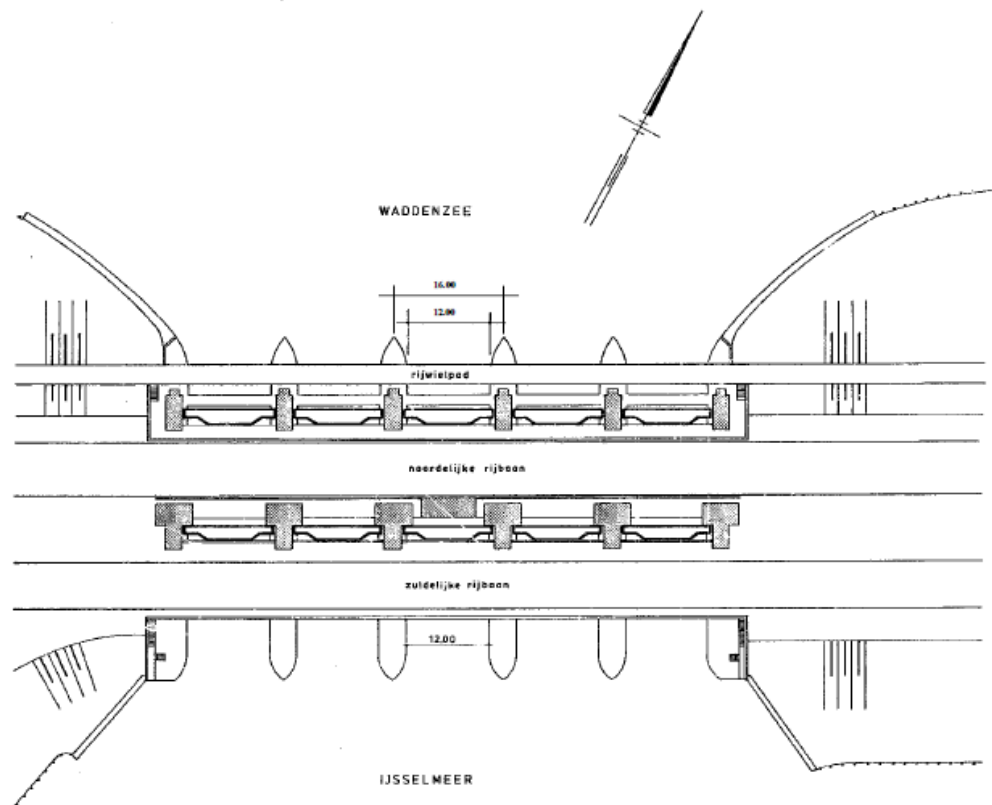
Figure 105. Top view of discharge sluice complex (Thijsse, 1972).

Each discharge sluice has two gates, a northern one and a southern one. Figure 106 shows the northern gate in an open position and the southern gate in a closed position. The gates are housed in towers that rest upon the pillars, which can be seen in Figure 105. Other functions but retaining and discharging of water also take place on the structure. In the North at the Waddenzee-side, there is an elevated bicycle road, and in between the towers and on the IJsselmeer-side a road deck is located. Just in front of the northern gate an extra beam can be seen in the cross-section. This beam is referred to as the defense beam and was needed as the structure was of strategic importance for the country.

The defense beam is designed to protect the discharge sluice for impact of a low-flying missile fired from an enemy vessel.
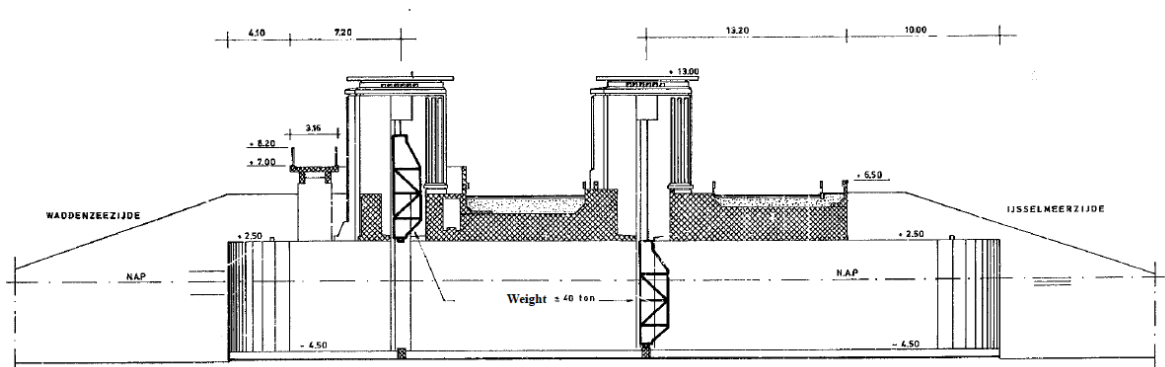
Figure 106. Cross-section of discharge sluice (Thijsse, 1972).

A.2.2 Differences at Kornwerderzand

The main difference between Kornwerderzand and Den Oever is the location and orientation of the breakwaters surrounding the sluice complexes. Figure 107 shows the locations of the breakwaters at each location respectively. The breakwaters have influence at the hydraulic boundary conditions of the area.

Figure 107. Den Oever (left) and Kornwerderzand (right) with their breakwaters highlighted in red.

Another difference is that the discharge sluices at Kornwerderzand, the Lorentzsluizen, are not founded on piles like the ones at Den Oever. They have shallow foundation, meaning that the structure sits on the bottom of the sea. This has however no influence on the scope of this research.

A.2.3 Technical Problems at the Discharge Sluice

Many technical problems were faced during the construction of the Zuiderzeewerken. However, the following two are of particular interest as they concern the discharge gates.
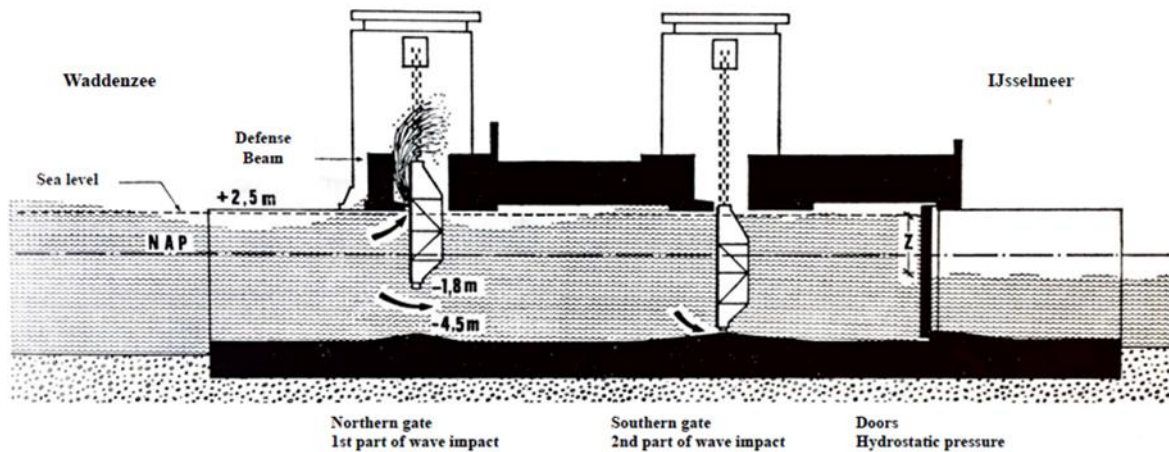
Figure 108. Position of gates during a storm (Thijsse, 1972).

As mentioned earlier in this chapter, a defense beam is located in front of the northern gate to withstand missile fire during a war. This defense beam, unfortunately, also has a negative effect. During a storm, where the water level is around the bottom of the defense beam (NAP + 2.50 m), the pressure of the wave impact amplifies due to the close location of the beam to the gate. This results in extreme stresses in the gate, which it was not designed for. To relief the pressure on the northern gate without replacing or redesigning structural parts of the complex, the engineers came up with a solution. As seen in Figure 108, The northern and southern gate are not fully closed, each taking a part of the wave load, while the hydrostatic pressure is taken by the wooden doors at the end of the sluice. Eventually the wooden doors have been removed from the complex and now they completely close the southern gate during a storm and still leave the northern gate partly open.

One of the most severe incidents of the Afsluitdijk did not even happen during a storm. Due to the flowing water, a downward force acts upon the gate when opening or closing partly submerged. This downward force became too large one day and pulled the entire 40 ton weighing gate down to its sill. This process was so aggressive that the counterweights hanging in the towers were pulled over their high point. The chains snapped on return dropping to the bottom of the tower. The counterweights were destroyed, while the floor and gate were still intact. The reason for this incident was perhaps the lubricant on the chains or the large head difference, but it resulted in new regulations. If discharging with partly opened gates, they have to be locked in position. Also, the gates are not allowed to be moved if the head difference is more than 1.25 m, which is a strange demand as the gates will have to be closed if an emergency occurs.

A.3 Reasons for Measures

Beside the fact that the Afsluitdijk is more than 80 years old, there are two main topics that dominate the reasons for strengthening and renewing the icon of the Dutch civil works. Those topics are water safety and discharge capacity. Two subtopics that also determine the course of the project, but are not a leading cause, are the road and ship traffic. The Afsluitdijk has become an important crossing for both ships and road vehicles. They need to be maintained during construction and improved after.

A.3.1 Water Safety

The Afsluitdijk has protected a large part of the Netherlands against flooding from the North Sea since the beginning of the last century. However, during a safety inspection in 2006, it was concluded that the dike does not satisfy the current safety standard. This was not only the case for the dike itself, but also for the discharge sluices and shipping locks at Den Oever and Kornwerderzand. Several issues with the dike resulted in a negative conclusion of the safety inspection. The dike is not high enough, but also the grass cover on top and on the inner slope of the dike is not sufficiently strong to withstand erosion in extreme weather conditions. In similar extreme conditions are the sluice complexes at Den Oever and Kornwerderzand not high and stable enough to endure the loading.

A.3.2 Discharge Capacity

In addition to protecting the country against flooding, the other main function of the Afsluitdijk is to discharge water from the IJsselmeer to the Waddenzee. This is done at two discharge complexes at Den Oever and Kornwerderzand. These complexes have large vertical gates, which will open when the water is low in the Waddenzee allowing the fresh water from the IJsselmeer to naturally out to the Waddenzee. When the water in the Waddenzee rises again, due to the naturally occurring tide, the gates at the discharge complexes close again to protect the inland against flooding. The tide is therefore the governing factor in the capabilities of discharging the fresh water out to the Waddenzee. In combination with wind, the water in the Waddenzee can be high enough that during low tide natural discharging of water is not possible. This happened only incidentally in 1998 when discharging was not possible for a couple of days causing a record water level in the IJsselmeer.
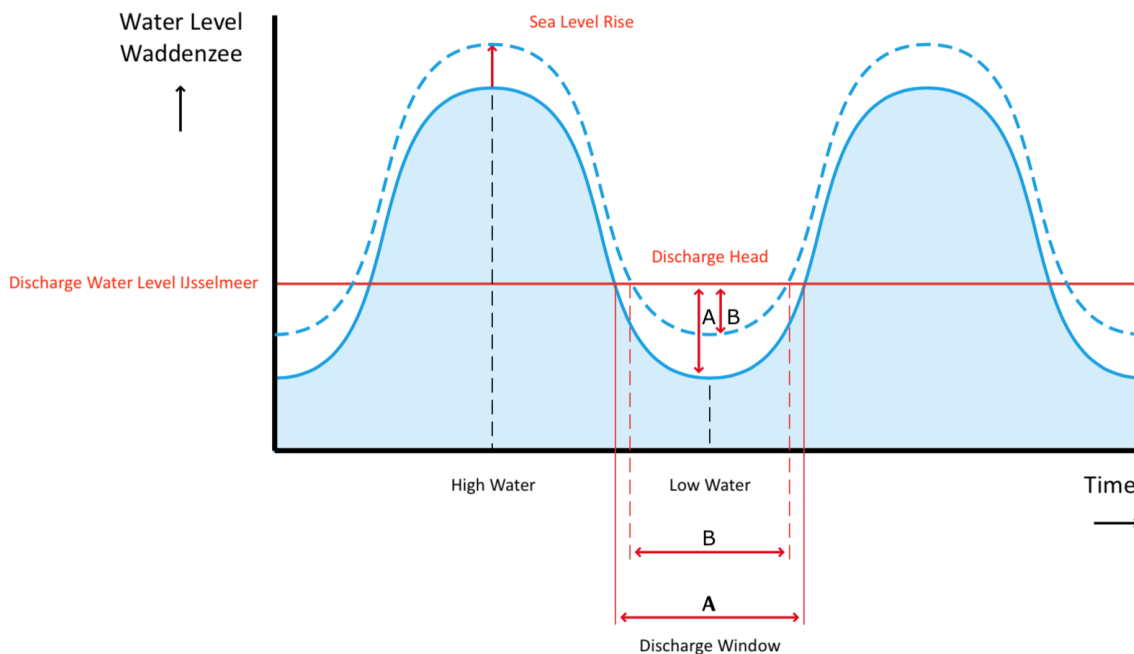
Figure 109. Problem situation of the discharge capacity at the Afsluitdijk (Witteveen+Bos, 2013).

Sea level rise will slowly reduce the time gap when natural discharging is possible, as can be seen in Figure 109. This is also seen in the amount of days the gates have to opened during the winter period when it is most needed. In the 70's of the last century about 120 to 130 days of the total 180 days of winter the gates were opened, while nowadays the gates are opened 150 to 160 days. Not only the time will be reduced, but also the head difference will decrease. Less head difference results in a lower flow velocity, which results in a lower discharge volume, increasing the problem even further. This will potentially cause major issues for the area in the future, arriving in the notion that the discharge capacity of the Afsluitdijk should be increased and should also be more resilient for extreme conditions.

A.4   Future

In 2016, the tender to strengthen and modernize the Afsluitdijk was made available for corporations to apply. The complete scope of the project contains strengthening of the dike, strengthening of the discharge complexes at Den Oever and Kornwerderzand, construction of two new locks, construction of a pumping station at Den Oever, the highway and a migration river for fish. The complete demands and reasoning of the scope will not be discussed in this report. The focus will be on the discharge complexes and pumping station at Den Oever and Kornwerderzand.

The entire Afsluitdijk will have to comply with the 1/10.000 per year safety standard. This standard is based on the probabilistic approach that a storm strong enough with a return period of 10.000 years should be resisted by the hydraulic structure. The hydraulic conditions that match such a storm can be found in the report 'Hydraulische Randvoorwaarden voor het ontwerp van de versterking van de Afsluitdijk' and will be discussed and analyzed in the main report when needed.

As explained in the previous chapter the discharge capacity will have to increase for future situations. Not only by natural head difference but also via a pumping station. This allows more volume to be discharged into the Waddenzee at low head differences. The reason this pumping station is needed is due to the expected sea level rise in the Waddenzee. 'Spuien als het kan, pompen als het moet' reads the slogan for the new pumping stations, which translates to 'Natural draining if possible, pumping if needed'. This ensures that the protocol of using the pumping station is as environment-friendly as possible. Two climate scenarios are used to establish the water levels for the coming years. Climate scenario W+ for water safety and G for water discharge, which are both established by the KNMI, who is the national meteorogical institute. Using W+ means that 35 cm has to be added to the water level in 2050 relative to the year 1990 and 85 cm for 2100. Climate scenario G only requires 25 cm to be added to the water level in 2050 with respect to 1990, meaning that this approach is less conservative. The reason for the difference in approach has a lot to do with social risk. Safety of civilians is much more important than some inundation. Flexibility also plays a large role, where strengthening the entire Afsluitdijk is not easily done, while increasing some discharge capacity is generally believed easier accomplished.

Table 10. Target water levels of the IJsselmeer for the summer and winter months.

Period	Months	Target Water Level [NAP +]
Summer	April - September	-0.20
Winter	October - March	-0.25

Table 10 shows the target water levels in the IJsselmeer for each month in the year. These targets should be seen as an average over a longer period as they cannot be maintained on a daily basis due to the impact of the river discharge and weather. The lowest allowable value is NAP - 0.40 m, because at that level the water depth is still sufficient for ships to travel across the lake without any disturbance. The highest acceptable water level is NAP + 0.55 m as it is the limit before flooding problems occur around the lake.

The project to strengthen the Afsluitdijk for the first time after its initial construction was granted to Consortium Levvel at the start of 2018. Engineering consultant Witteveen+Bos is part of this consortium and gave insight in their designs for the use of this report. Their designs will be discussed and analyzed in the following chapter. The focus will be on the discharge sluice complex at Den Oever as it is part of the scope of this research.

B   Hydraulic Boundary Conditions

This Appendix holds the derivation of the hydraulic boundary conditions of the case that is used in this research. The Afsluitdijk and therefore also the gates in the discharge sluice complexes need to withstand a storm that statistically occurs once every 10.000 years. This safety standard has been determined by the Dutch government (RWS). However, it was believed and proven by Hofland (2015) that the water level corresponding to the most severe storm with a return period of 10.000 years is not the governing situation for the gates. Lower water levels around NAP + 2.50 m actually produce higher loads for the gates. In order to still comply with the prescribed safety standard, the hydraulic conditions from a 1 in 10.000 storm were taken at the moment the water levels reached the desired height. Figure 110 shows how this works. These conditions were derived using the model Hydra-K.
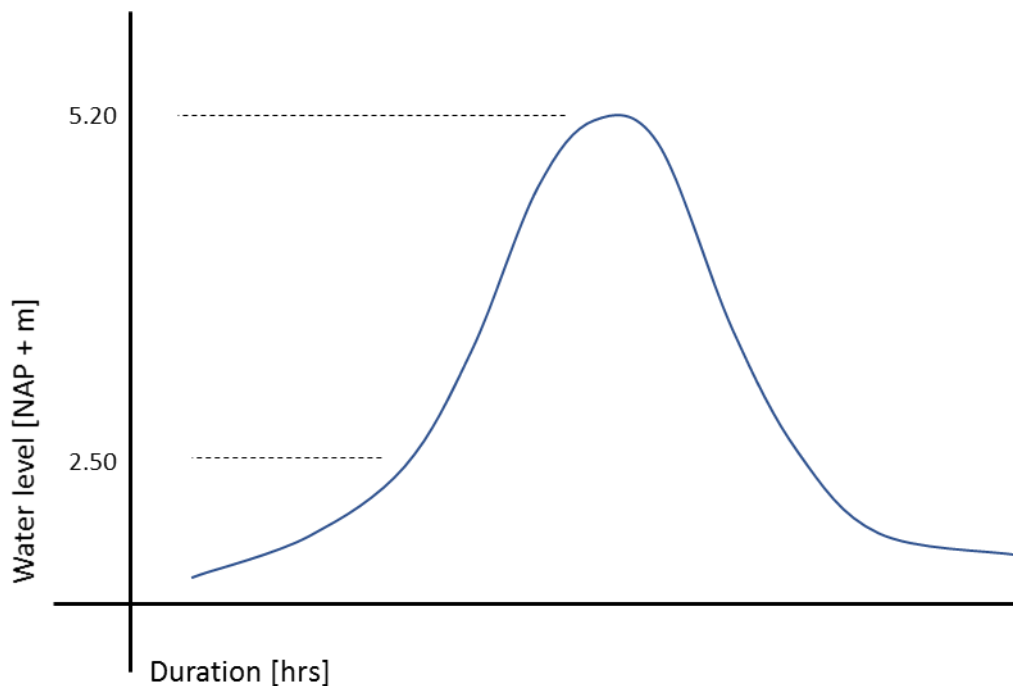
Figure 110. Development of a storm with a 10.000-year return period.

For the use of this research, the values derived from these model calculations, were used. It is convenient to use these values as they have also been used for the physical model test of Hofland (2015). The boundaries of the case have been derived in this manner as can be seen in Table 11.

Table 11. Governing wave conditions for the case.

ID	Location	Gate	H_s [m]	$T_{m-1.0}$ [s]	T_p [s]	h [m + NAP]
O3	Den Oever	North	2.08	3.88	4.55	2.6

The reason that the used water levels are 2.6 m above NAP and not 2.5 m is because of uncertainties in the approach. These uncertainties are covered by implementing robustness, which in the case of this situation is equal to 0.1 m. Furthermore, sea level rise has already been enforced within the model. However due to fact that the governing case for the gates is actually a low water level, it is not taken into the hydraulic conditions. Table 12 shows the effect of the sea level rise for the years of interest as they are applied for the project. The conditions for the gates and therefore the situations regarding this research will be applied for the year 2020.

Table 12. Chosen values of sea or lake level rise for both sides of the Afsluitdijk using most recent boundary conditions.

Year	Waddenzee	IJsselmeer
2020	0 m	0 m
2050	0.28 m	0 m
2100	0.78 m	0.60 m

Besides the wave conditions, also hydrostatic pressure is present in the situation of the case. The case focusses on the ultimate limit state, which provides certain water levels according to the demands of RWS. The direction of the wind in the governing condition causes the water level at the Waddenzee-side to be pushed up, while the IJsselmeer-side is lowered, see Figure 111. The water levels of the hydrostatic pressure are different from the wave condition, but both are part of the ultimate limit state of the gates and should therefore be upheld.
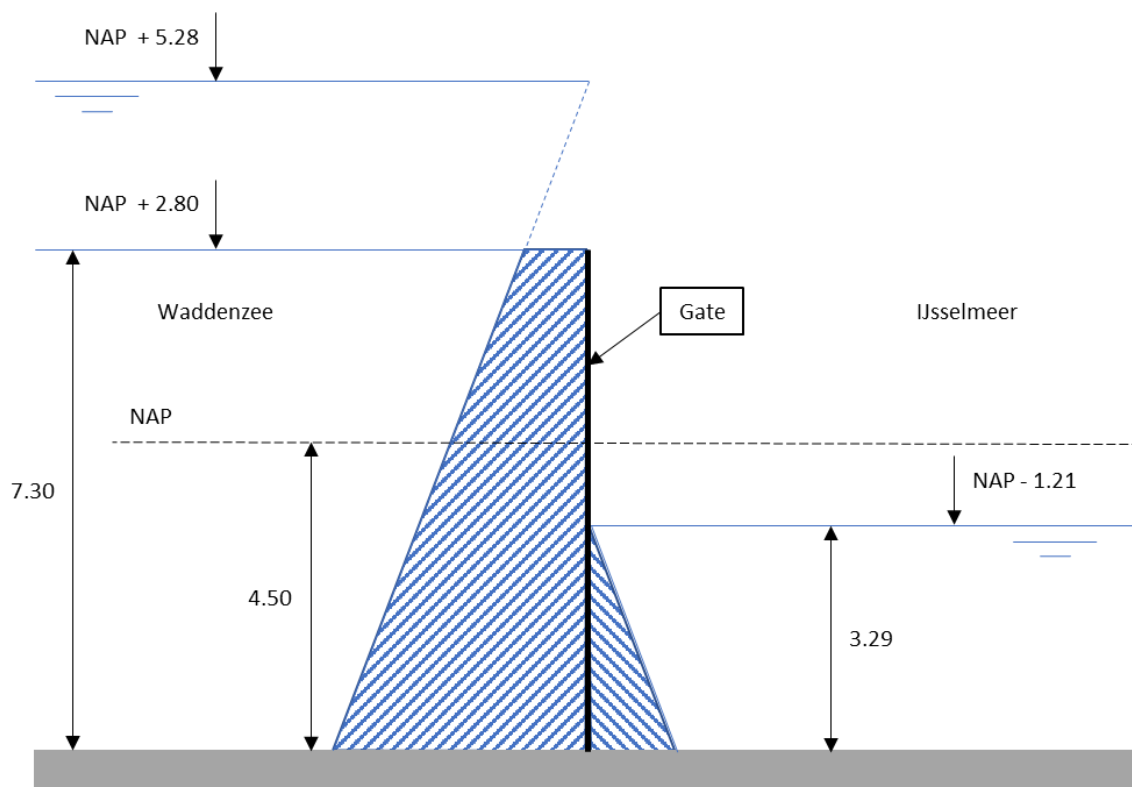
Figure 111. Schematization of the hydrostatic pressures on the gate for the 1:10.000 storm condition.

C   Solution of SDOF system for triangular pulse load

This appendix contains the analytical solution of a single degree of freedom (SDOF) system subjected to a triangular shaped impulse. Three different triangles are analysed, namely falling, symmetrical and rising. These solutions are used in the quasi-static method composed by Kolkman as the triangular shape represents the shape of a wave impact.
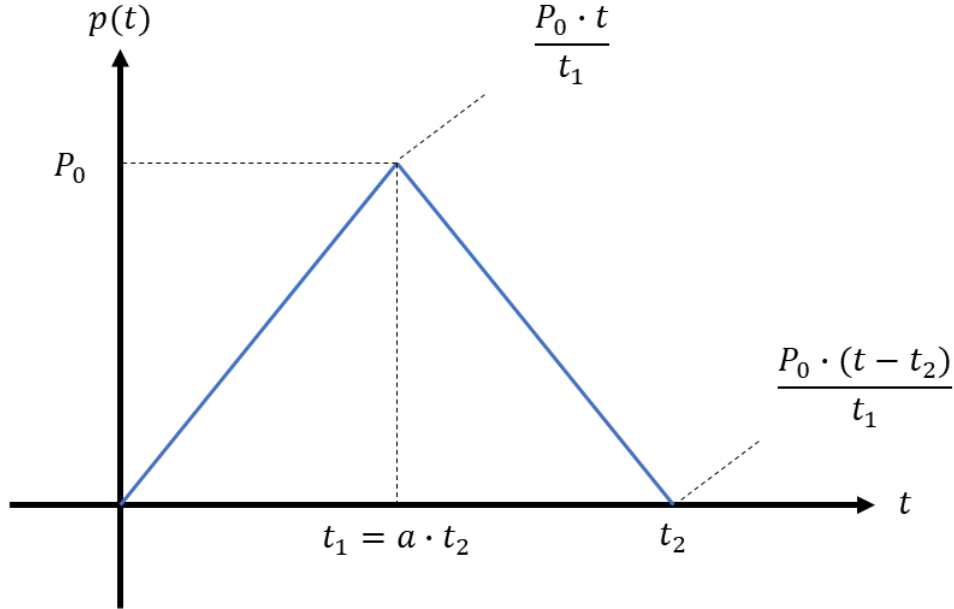
Figure 112. Representation of a triangular impulse as the superposition of three ramp functions.

The triangular shaped impulse can be represented as the superposition of three ramp functions, see Figure 112. These each are separated by their own domain; the first is $t \leq t_1$; the second is $t_1 < t \leq t_2$; The third and last is $t > t_3$. Each ramp function combined with its domain will result in a solution of the SDOF system to this specific pulse load, see Equation 9.1.

$$u(t) = \begin{cases} \dfrac{P_0}{k} \cdot \left(\dfrac{t}{t_2} - \dfrac{\sin \omega t}{\omega t_2} \right) & t \leq t_1 \\[2ex] \dfrac{P_0}{k} \cdot \left(1 - \dfrac{t}{t_2} - \dfrac{\sin \omega t}{\omega t_2} + \dfrac{\sin \omega (t - t_1)}{\omega t_2} \right) & t_1 < t \leq t_2 \\[2ex] \dfrac{P_0}{k} \cdot \left(-\dfrac{\sin \omega t}{\omega t_2} + \dfrac{\sin \omega (t - t_1)}{\omega t_2} - \dfrac{\sin \omega (t - t_2)}{\omega t_2} \right) & t > t_2 \end{cases} \qquad 9.1$$

Solving the functions for a time domain with a specific length of the triangular pulse and a specific angular frequency will create a response as shown in Figure 113. The figure also shows a damped signal. This damped signal can be applied using Equation 9.2, where ζ represents the percentage of damping. Meaning that ζ equals 0.02 when 2 % of damping is enforced.

$$u(t) \cdot e^{-\zeta \omega t} \qquad 9.2$$
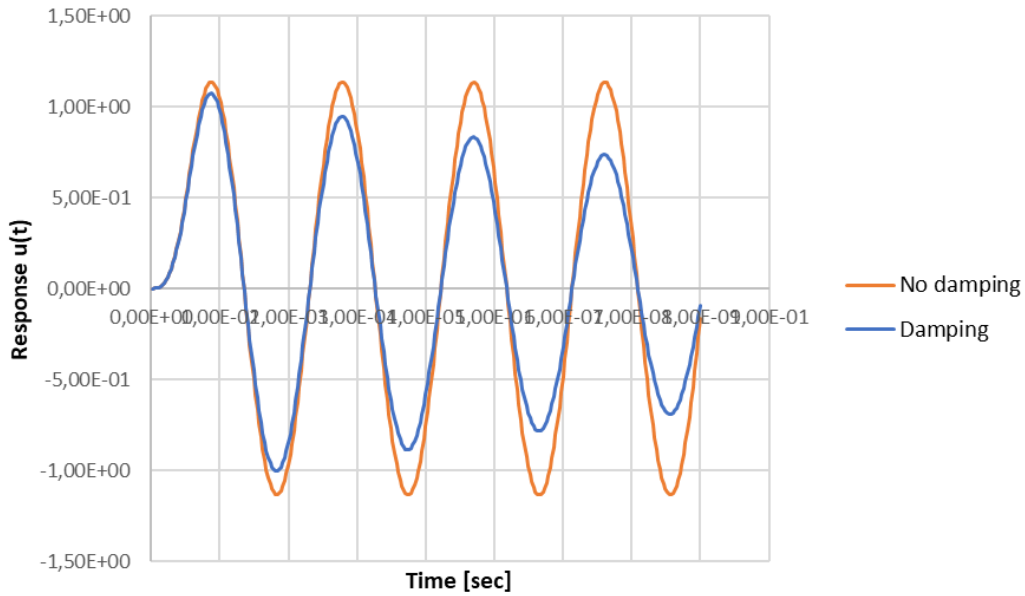
Figure 113. Response of a triangular shaped pulse.

When all the maxima of the different response functions are summed up, the dynamic amplification factor (DAF) is found, see Figure 114. In the figure the DAF is shown versus the period of the load 'τ' over the period of the structure 'T', which is how it often is portrayed. The figure also clearly shows the effect of different shaped triangles by altering the length of the t_1.
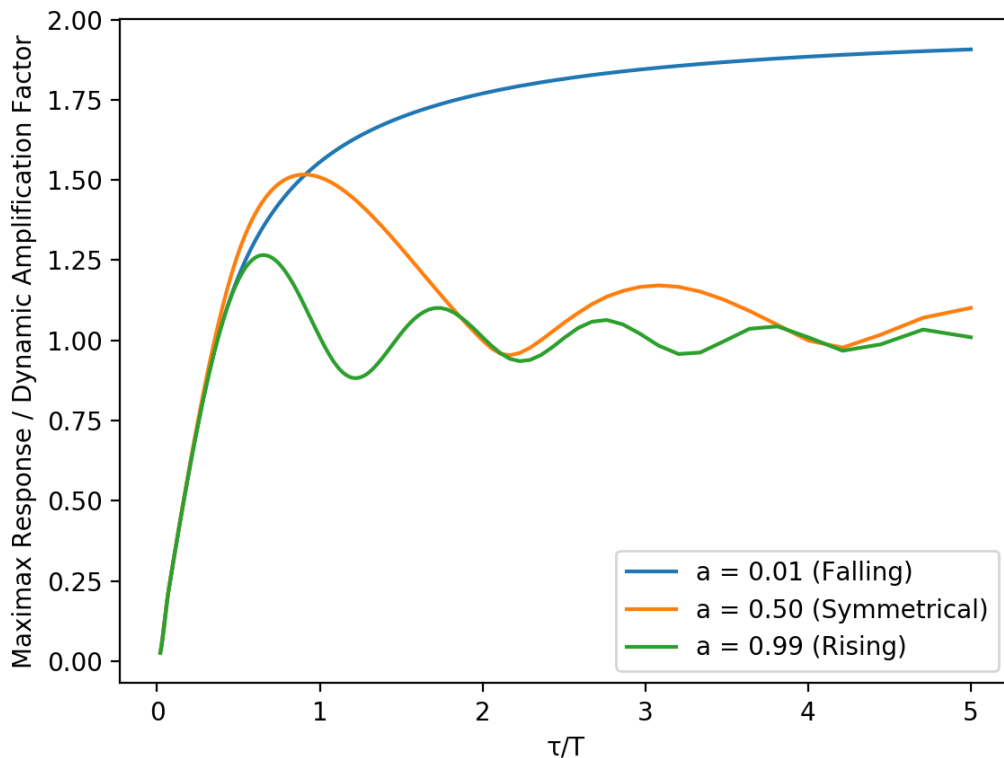
Figure 114. Dynamic amplification factor for three different shaped triangular pulses.

D   Hydrodynamic Mass

This Appendix contains several methods of calculating hydrodynamic mass or added water mass. This is useful as the natural period of the system is influenced by the oscillating water body attached to it. The different methods are explained with their assumptions and what that means for the limitations. The methods are compared by the use of an example calculation.

D.1   Engineering Practice

The method used in the engineering practice is described in the book of Kolkman and Jongeling from 2007, 'Dynamic Behaviour of Hydraulic Structures'. The method allows for the calculation of the average dynamic pressure across the height of a wall with a horizontally vibrating bottom section. This bottom section has a component that is proportional to the vibration acceleration, which generates the hydrodynamic mass.
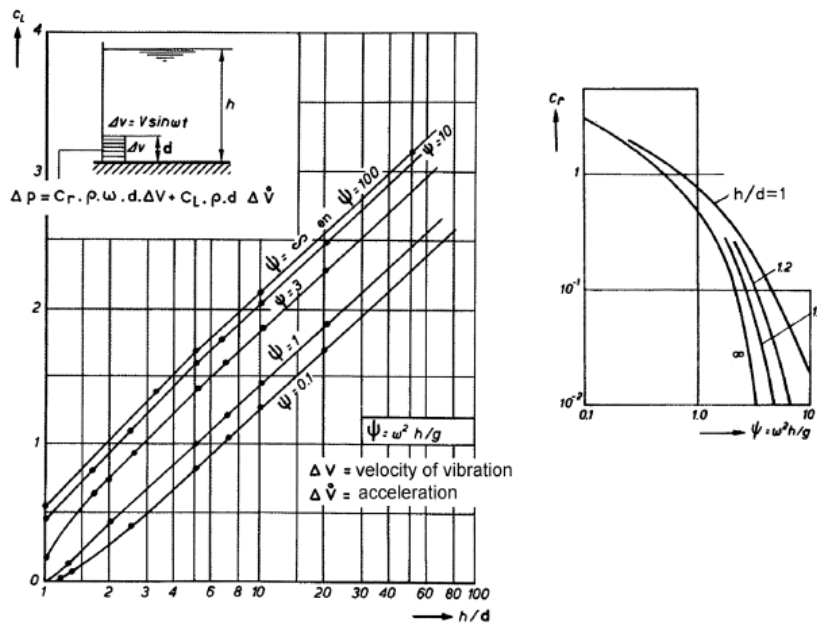
Figure 115. Coefficient C_L and C_r used for the added mass (Kolkman & Jongeling, Dynamic behaviour of hydraulic structures part B, 2007).

Figure 115 contains the results of the two-dimensional calculation of the added water mass and damping. The coefficient C_L and C_r are used to determine the added water mass and damping respectively. Equation 9.3 shows the method of calculating the added water mass.

$$m_{am} = C_L \cdot \rho \cdot d^2 \qquad\qquad 9.3$$

When h/d is equal to 1, which is the case for the gates at the Afsluitdijk as they can vibrate over the full length, then Ψ will most likely be larger than 100. This will not be the case for structure that have a natural frequency below 2 Hz. Meaning that the added water mass is independent of the frequency with larger values of frequency. For comparison an example calculation is made with the variables from Table 13.

Table 13. Variables for the example calculation.

Variable	Value	Unit
ρ	10.10	kN/m^3
d	7	m
h	7	m
f	10	Hz
g	9.81	m/s^2
C_L	0.55	-

The result of this example is an added water mass equal to 272.195 kN/m.

D.2   Westergaard

Westergaard was the first to provide a solution for the hydrodynamic pressures under influence of vibration. The vibration he was interested in was caused by earthquakes. The solution Westergaard (1939) presented was based on the two-dimensional wave equation for compressible fluids. For his derivation a few assumptions are made.

- Pressure at the water level is zero
- No surface waves present
- Structure itself is rigid and vertical
- The water body is infinitely long

With these assumptions Westergaard developed a simplified formula to calculate the hydrodynamic pressure on a structure. This formula is shown in Equation 9.4 in an adapted form in order to make it use it for the example calculation.

$$m_{am\_W} = \int_0^z \frac{7}{8} \cdot \rho_w \sqrt{d} \, dz \qquad\qquad 9.4$$

Using the same variables from Table 13, Westergaard's solution gives an added water mass of 288.617 kN/m.

D.3   Housner

Housner (1954) developed a method to calculate the hydrodynamic pressures for containers filled with fluid under earthquake loading. Housner did so by making a distinction between the impulsive and convective pressures, where the convective component relates to the sloshing and the impulsive component to the fluid that moves in coherence with the structure, which can be seen as the added water mass. The difference between the solution of the Housner and Westergaard is that Housner takes the effect of the length of the water body into account. Equation 9.5 shows the formula of Housner adapted in order to calculate the hydrodynamic mass directly.

$$m_{am\_H} = \frac{\rho_w \cdot d^2}{\sqrt{3}} \tanh\left(\frac{\sqrt{3} \cdot L}{d}\right) \qquad\qquad 9.5$$

Using the variables from Table 13 with the addition of a length equal to 20 m, the added water mass becomes 285.702 kN/m. However, Table 14 shows the length effect of the water body. It should be noted that the effect will play a role when the body of water is smaller than 4 times the height of the structure.

Length water body [m]	Height over length (h/L)	Hydrodynamic mass (Housner) [kN/m]
1	7	69.291
2	3.5	130.886
5	1.4	241.342
10	0.7	281.706
20	0.35	285.702
40	0.175	285.731

D.4 Numerical

In order to account for all the possibilities of the shape of the water body and different type of boundaries a numerical method is the best option. This method allows for complex shapes of the water body. It also makes it possible to see the effect of higher order modes of the gate. The Laplace equation is solved for a predetermined domain and by implementing the correct boundary conditions the hydrodynamic mass can be calculated. This has been done using a PDE solver in Matlab with the same values for the variables as described in Table 13. A two-dimensional or three-dimensional version can be applied. Table 15 contains the results of these calculations also including the differences of the length of the water body.

Table 15. Results of hydrodynamic mass calculation using numerical method.

Length water body [m]	Height over length (h/L)	Hydrodynamic mass (2D) [kN/m]	Hydrodynamic mass (3D) [kN/m]
1	7	65.432	72.198
2	3.5	119.934	132.418
5	1.4	220.626	243.762
10	0.7	264.178	291.931
20	0.35	269.824	298.179
40	0.175	269.889	298.250

A plate under loading will vibrate in many different shapes. In order to simulate these higher modes, the numerical method can be adapted. The boundary where the gate is located can be subject to a sinusoidal movement instead of a complete rigid movement. Figure 116 shows some examples of how the hydrodynamic mass responds to these higher modes.
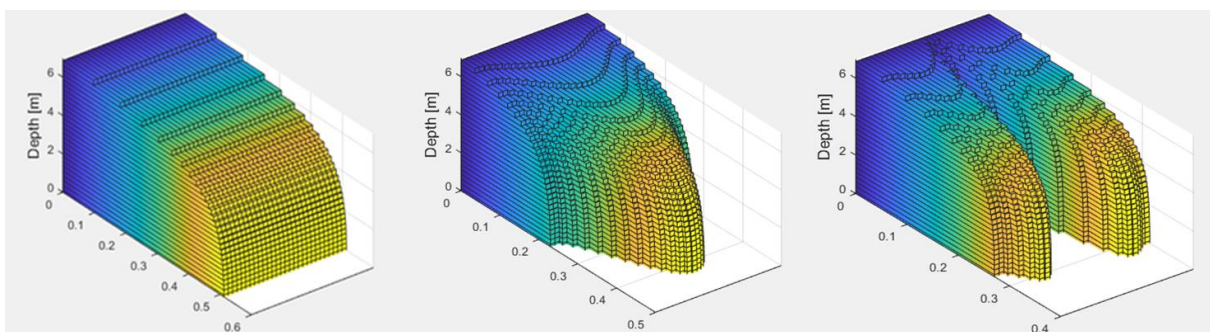
Figure 116. The distribution of the hydrodynamic mass for a rigid movement of the gate and the first and second mode of a sine movement in the horizontal direction (from left to right)

Finally, it is possible to implement all types of boundaries and shapes into the domain of interest to best fit the problem at hand. An example of a lock head is seen in the following figures.
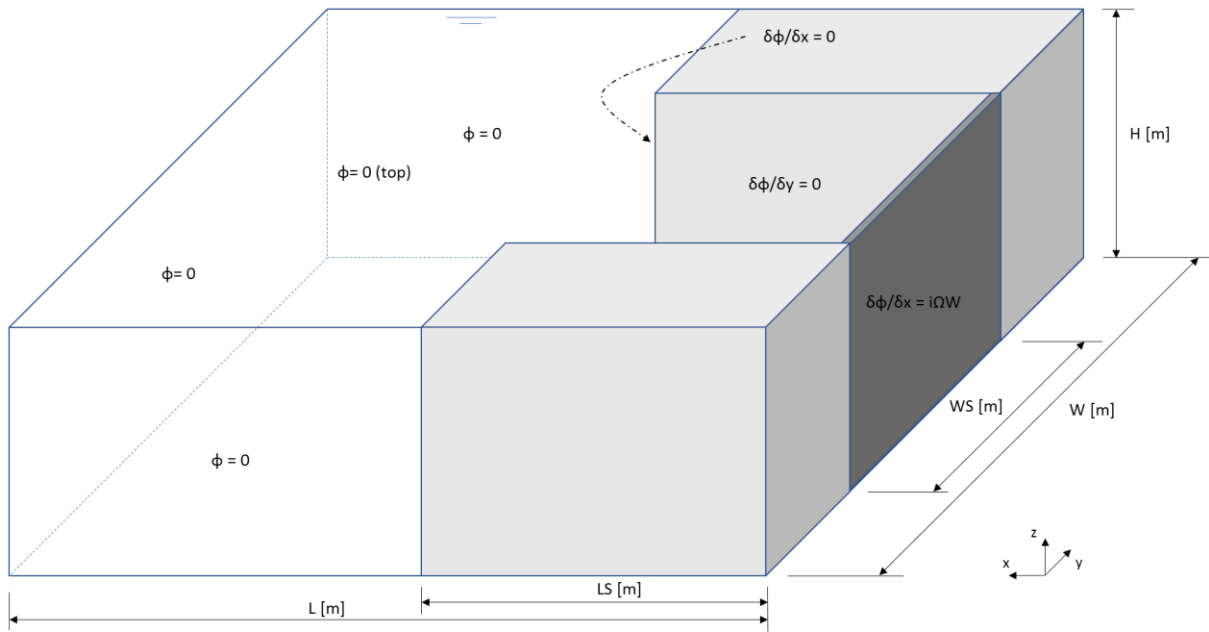
Figure 117. 3D overview of the boundary conditions and dimensions to calculate the hydrodynamic mass.
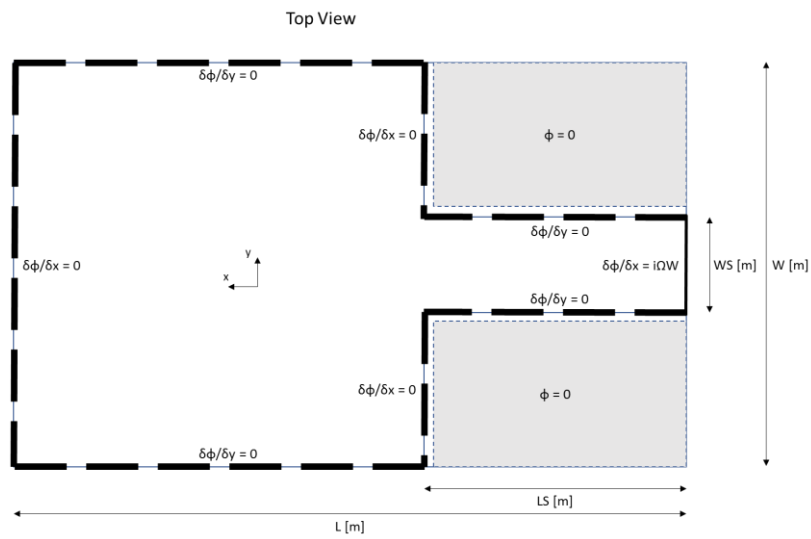
Figure 118. Top view of the boundary conditions and dimensions to calculate the hydrodynamic mass.
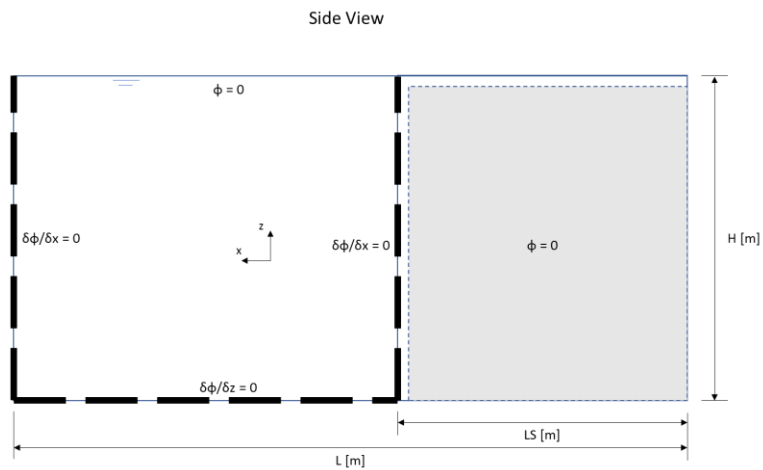
Figure 119. Side view of the boundary conditions and dimensions to calculate the hydrodynamic mass.

105

E   Numerical Scheme for Calculation of Potential

In order to solve Laplace's equation a numerical scheme is applied (Shankar, 2012). A scheme for a two-dimensional situation and also a three-dimensional is found. The two-dimensional scheme is based an explicit second order central difference in space and uses the five-point stencil, see Figure 120.
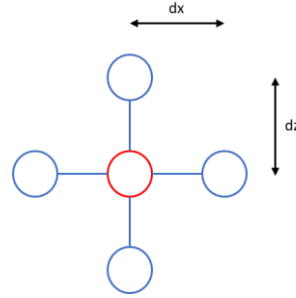
Figure 120. 2D five-point stencil.

The two-dimensional five-point stencil solves the solution for the center node (shown in red) at every iteration. The four surrounding nodes have influence at the development of the center node and is calculated according to the scheme from Equation 9.6.

$$P(z,x) = \frac{dz^2 \cdot \big(P(z+dz,x) + P(z-dz,x)\big) + dx^2 \cdot \big(P(z,x+dx) + P(z,x-dx)\big)}{2 \cdot (dx^2 + dz^2)} \quad 9.6$$

The boundary conditions that can be applied in such a numerical scheme are Neuman and Dirichlet type of conditions. A Neuman boundary condition is applied for the derivative of the solution, while the Dirichlet boundary condition is not. In the discharge sluice complex the Neuman boundary represents the wall and the Dirichlet will represent the free water surface.
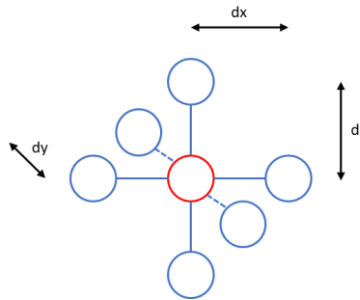
Figure 121. 3D seven-point stencil.

For the three-dimensional situation a seven-point stencil has been used, see Figure 121. the method operates very similar as with 2D, but with an extra dimension, see Equation 9.7.

$$P(z,x,y) = \frac{dx^2 \cdot dy^2 \cdot \big(P(z+dz,x,y) + P(z-dz,x,y)\big)}{2 \cdot (dx^2 \cdot dy^2 + dz^2 \cdot dy^2 + dz^2 \cdot dx^2)} \; +$$

$$\frac{dz^2 \cdot dy^2 \cdot \big(P(z,x+dx,y) + P(z,x-dx,y)\big)}{2 \cdot (dx^2 \cdot dy^2 + dz^2 \cdot dy^2 + dz^2 \cdot dx^2)} \; + \qquad 9.7$$

$$\frac{dz^2 \cdot dx^2 \cdot \big(P(z,x,y+dy) + P(z,x,y-dy)\big)}{2 \cdot (dx^2 \cdot dy^2 + dz^2 \cdot dy^2 + dz^2 \cdot dx^2)}$$

F   Peregrine Numerical Validation

The analytical solutions described in the paper of Cooker & Peregrine (1995) and Wood & Peregrine (1996) use complex mathematical schemes involving conformal mapping to ensue correct application of the vertical and upper horizontal boundaries, however such methods are not required anymore. The computational strength of computers results in accurate numerical finite difference methods. The analytical approach is more exact and faster when known, but with enough iterations a numerical approach is just as accurate. A numerical approach has more flexibility as it can easily be changed to fit any shape of the domain with any type of boundary. This appendix shows how a numerical scheme can approach the solution of Wood & Peregrine (1996) based upon the schemes from Appendix E.
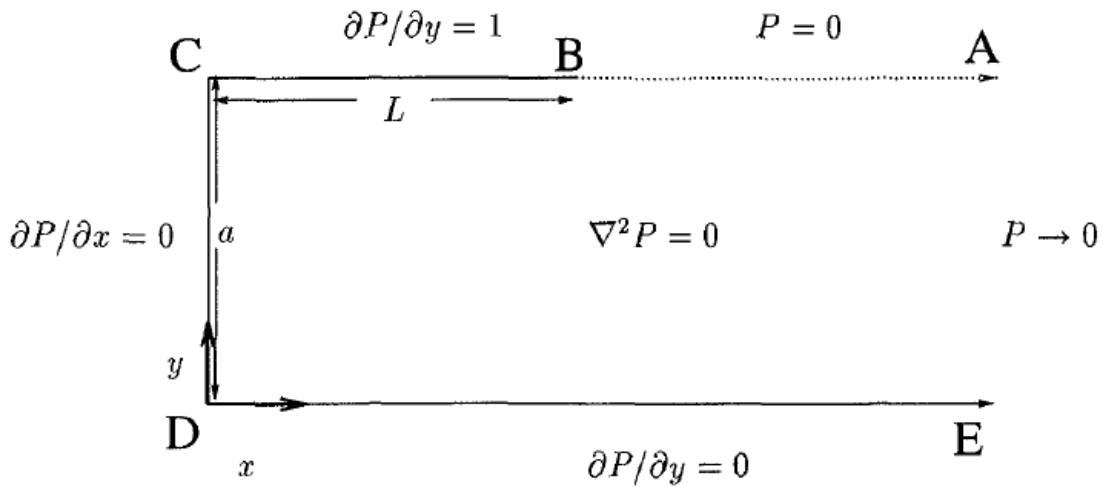
Figure 122. The schematic representation of the mathematical problem of Wood and Peregrine. Showing the height of the wall a and width of the deck L (Wood & Peregrine, 1996).

Figure 122 shows the problem visualized by Wood & Peregrine. The important aspects are the boundary conditions and the ratio between the horizontal upper deck L and the vertical wall a. For simplification Wood & Peregrine assumed L equal to 1 leaving only the variable a as input for this problem (a = H/L). For easy comparison this assumption will also be made in this report.
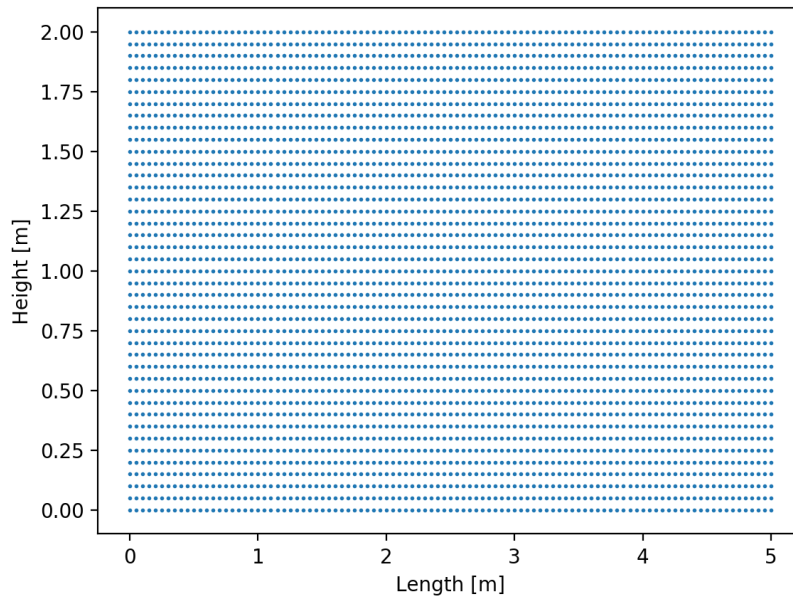
Figure 123. Location of nodes for numerical calculation with equal spacing of 0.05.

The numerical method is set up with a specific grid size. A small grid spacing results in a higher resolution of the solution, see Figure 123 for an example of a set up. After deciding the grid size, the boundaries are determined. The boundaries are based upon the analytical approach of Wood & Peregrine, see Figure 124. The black dotted lines represent walls and are Neumann boundaries, while the green dotted lines are Dirichlet boundaries. Only the red dotted line is somewhat different as it represents the cantilever beam and according to the idea of Wood & Peregrine (1996) it can be considered as a structure dropping onto the domain. Therefore, the derivative of the red boundary will be equal to 1, which can later be substituted for the vertical velocity of the incoming wave.
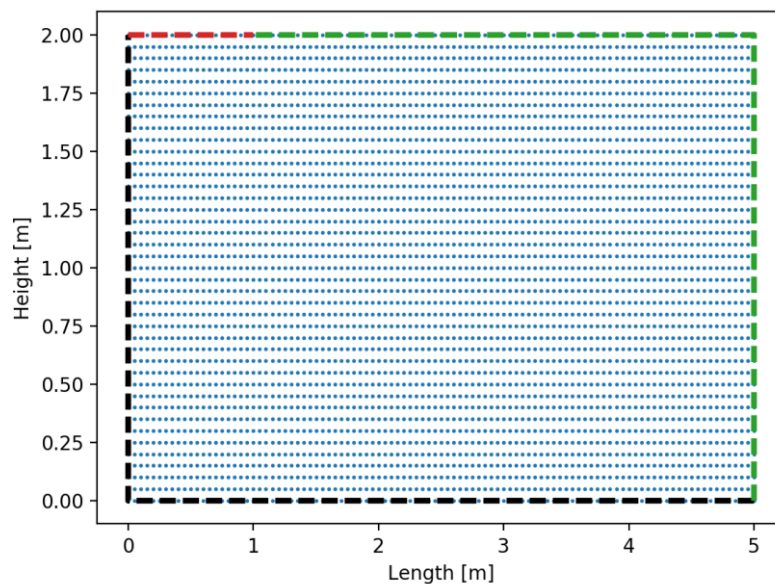
Figure 124. Location of nodes with addition of the boundaries.

To find the numerical solution, the algorithm from the Appendix E will go through all the nodes inside the boundaries, as the boundaries are pre-allocated. The algorithm repeats the scheme for every node until a convergence is met. Figure 49, Figure 125 and Figure 126 show comparisons of the analytical, from Wood & Peregrine (1996), and numerical solutions.
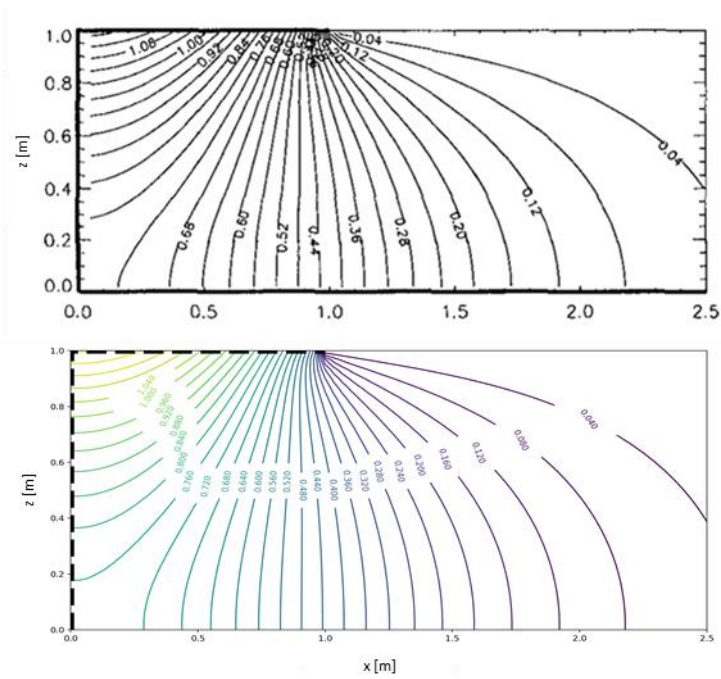
Figure 125. Analytical (top, from: (Wood & Peregrine, 1996)) and numerical (bottom) solutions with a = 1.
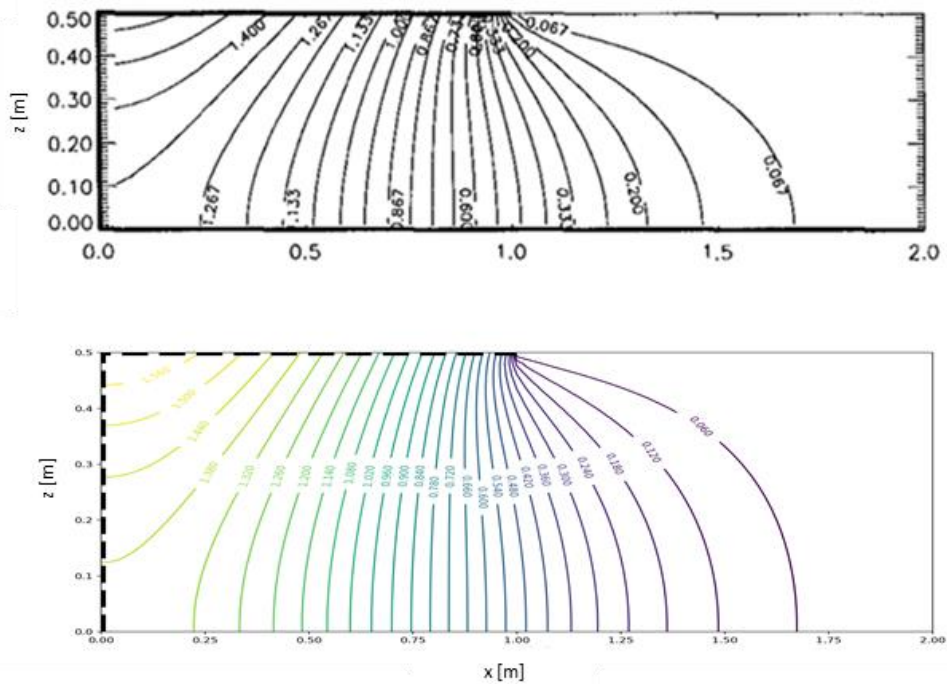
Figure 126. Analytical (top, from: (Wood & Peregrine, 1996)) and numerical (bottom) solutions with a = 0.5.

The figures all show a clear correspondence, allowing the continuation of the numerical method. The only problem with the numerical method is the number of iterations required for convergence. A stop criterion is introduced, see Figure 127. For each node the difference of the pressure-impulse between 100 iterations is calculated. The criterion is met if that difference is smaller than 10^{-5}. This has to be the case for all nodes in the grid before enough iterations have reached convergence. The convergence is therefore dependent of the number of elements in the domain.
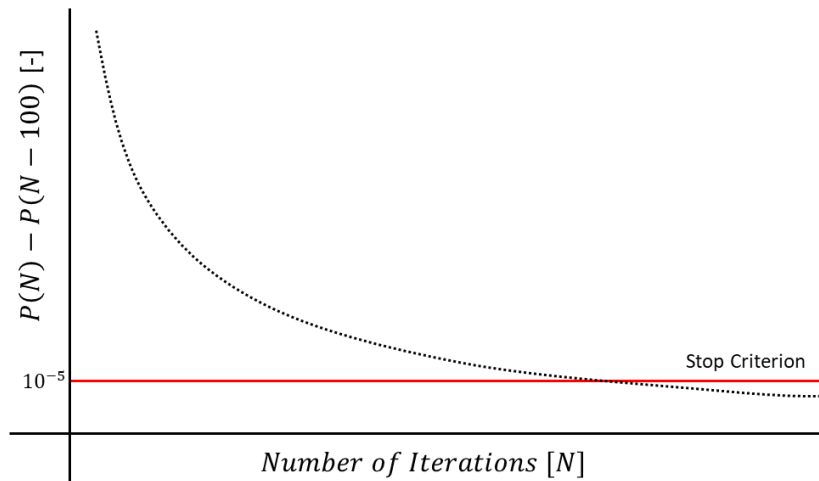
Figure 127. Stop criterion of algorithm to find pressure-impulse.

Finally, Figure 128 shows that domains with a large overhang compared to the depth need more iterations than others. A large overhang will also have increased three-dimensional effects, which are not incorporated in this numerical method. Small values for 'a' are for both these reasons not ideal for the use of this method.
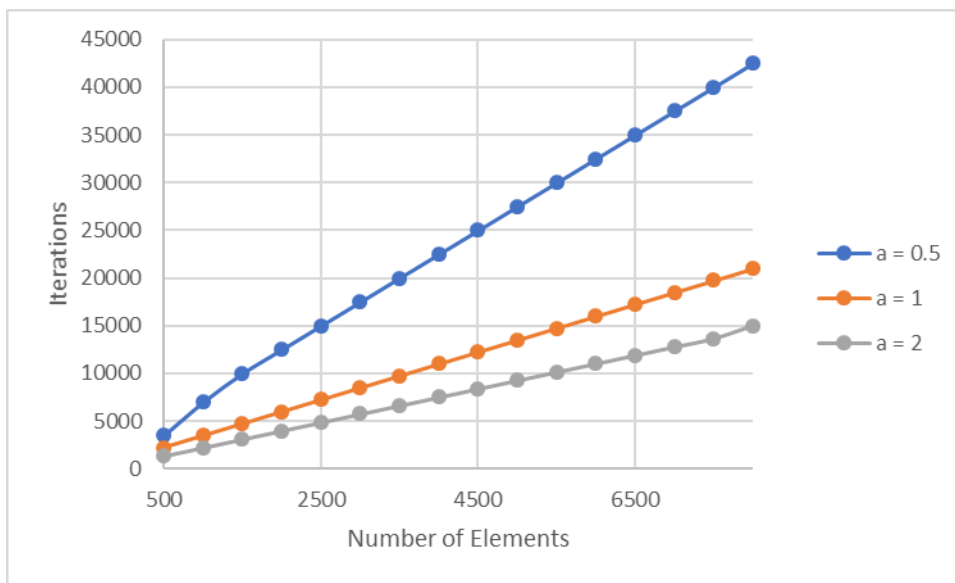
Figure 128. Conversion rates of different values for a [-].

G   Parametric Model Responsive Test

To show the response of the parametric model to different loading, an example has been applied. Figure 129 shows two forces that have been enforced on a parametric gate design. The placement of the stiffeners are the only parameters that are variable in this example, see Figure 130. The figure shows that the vertical and horizontal stiffeners both have 5 different locations of possible placement. The other parameters are shown in Table 16. In total 90 variants were calculated (overlapping variants are excluded) with the use of a scheme given in Appendix H, that makes sure every appropriate variant is calculated. The calculation was done in the frequency-domain.
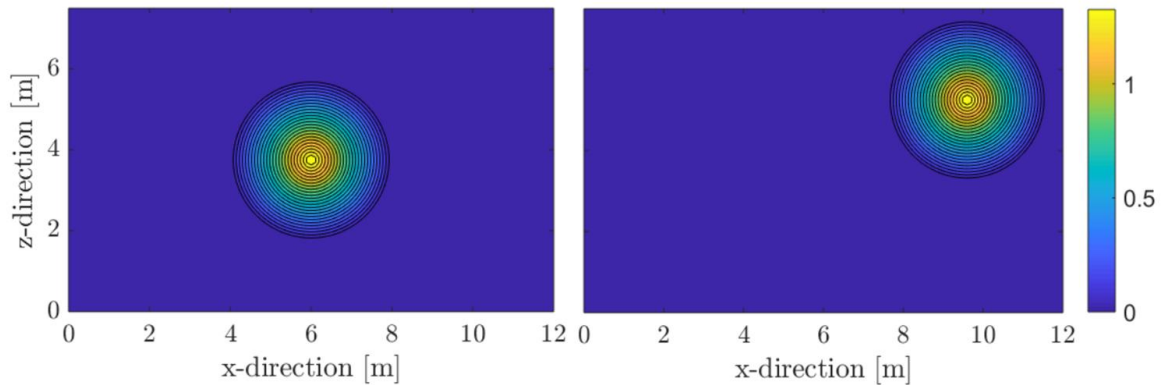
Figure 129. Circular force in center (left) and corner (right) of the gate.
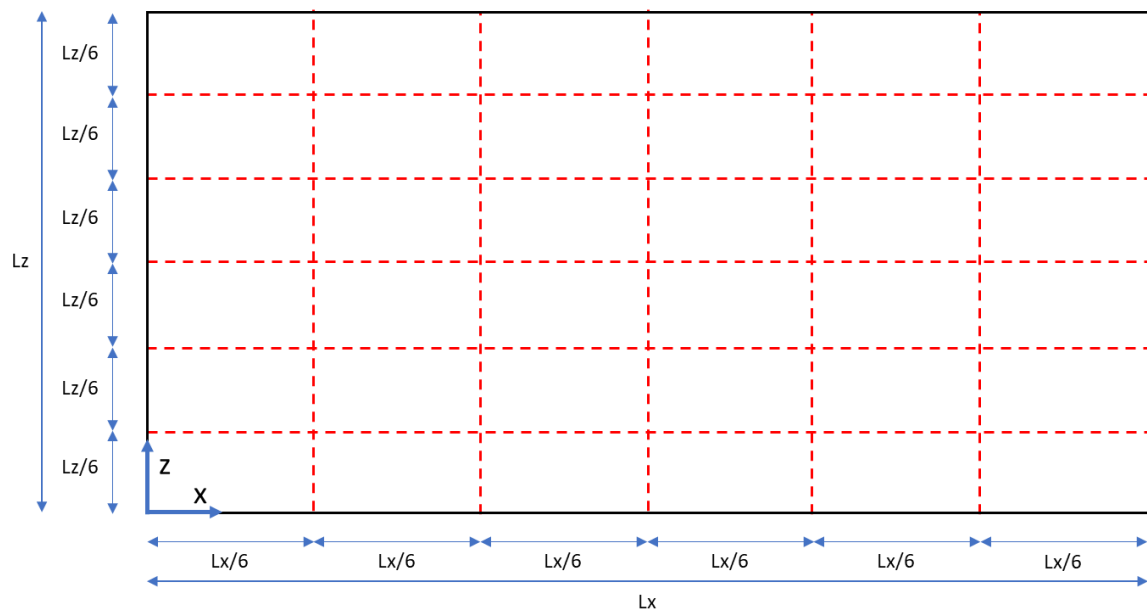
Figure 130. Variation of the placement of the stiffeners in vertical and horizontal direction of the example.

This test is done to see if the most optimal design for each load has an expected placement for the stiffeners. The parametric model will find the most optimal design by selecting the design with the least amount of material that still complies with the demand, which can be a maximum deflection or stress. Maximum deflection is used in this example as design reference. However, in this particular example all the variants have the same volume of material, so the best solution is chosen by lowest maximum deflection.

Table 16. Fixed parameters of the parametric model of the example.

Parameter	Value	Unit
Width (Lx)	12	m
Length (Lz)	7.5	m
Plate thickness	5	mm
Thickness vertical stiffeners	15	mm
Thickness horizontal stiffeners	15	mm
Length vertical stiffeners	0.8	m
Length horizontal stiffeners	0.8	m
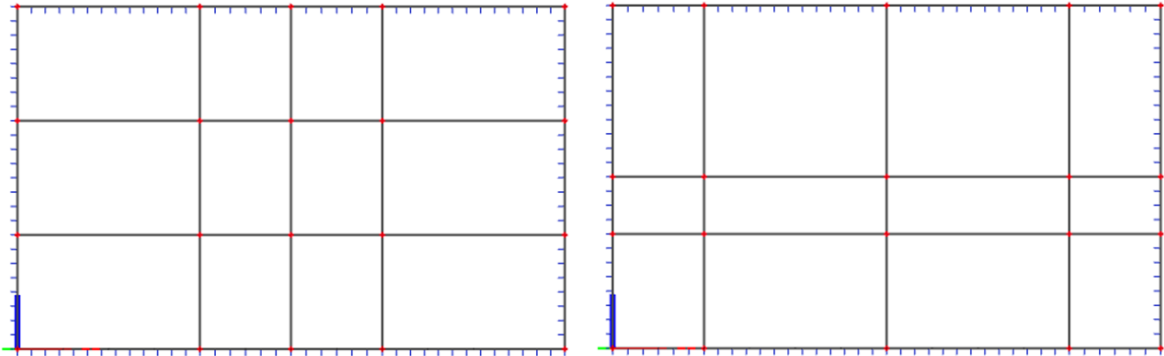
Figure 131. Best (left) and second best (right) designs with the force in the center.

The results of the calculations are then automatically remodeled into SCIA to see how the stiffeners have been placed, see Figure 131 and Figure 132. It is clearly visible that the force has an effect on the way the design is optimized.
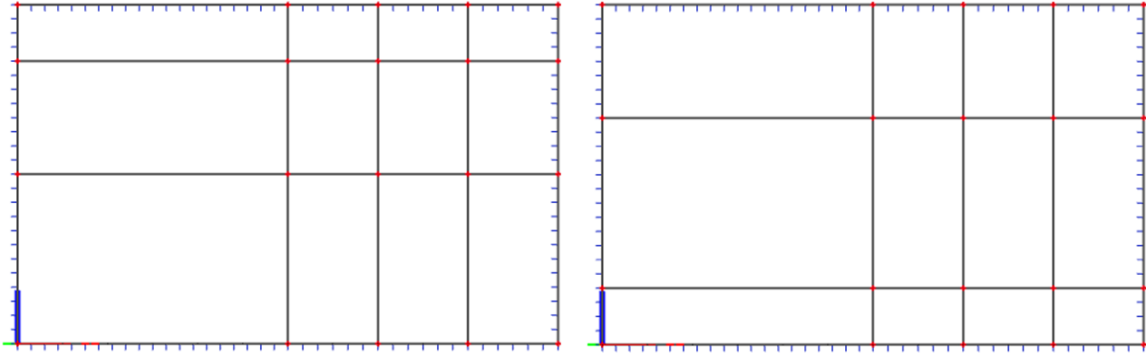
Figure 132. Best (left) and second best (right) designs with the force in the corner.

This first example was created with relative thick stiffeners compared to the plate thickness, which gives the stiffeners a lot of influence. Figure 133 shows the situation with a relative thick plate (50 mm) compared to the stiffeners and the resulting designs of both forces are exactly the same. This contributes to the notion that all parameters have significant influence in the design and should all be considered before any judgement can take place. Therefore, a smart optimization scheme has to be applied in order to find the optimal design without having to calculate all the possible variants. A sophisticated Artificial Intelligence (AI) based upon a neural network will be applied, see 7.2.1.
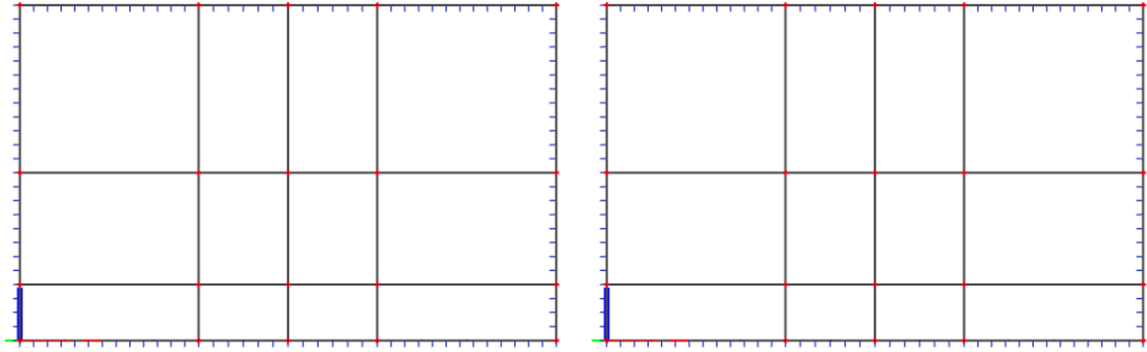
Figure 133. Best designs with a relative thick plate with force in the center (left) and corner (right).

H   Numerical Scheme for Optimization

This appendix shows different schemes that have been used to make sure the FSI model finds an optimal design for each specific case. These schemes only hold for the parametric model as it can be used in a design phase. First a scheme is explained that allows for the calculation of all variants that have been created by the number of variables of each parameter. The problem can be clarified by an example. For instance, a system that requires 6 parameters, as shown in each row in Figure 134, can have any number of variants per parameter. In the example the first and fifth parameter each contain 3 variants, the second has 2, and the third, fourth and sixth only have 1. The reason that this variety in length may occur is that not always the same parameter will be examined at the same time.

$$
Par = \begin{bmatrix}
P1\,(1) & P1\,(2) & P1\,(3) \\
P2\,(1) & P2\,(2) & 0 \\
P3\,(1) & 0 & 0 \\
P4\,(1) & 0 & 0 \\
P5\,(1) & P5\,(2) & P5\,(3) \\
P6\,(1) & 0 & 0
\end{bmatrix}
$$

Figure 134. Matrix showing the number of variants per parameter as example.

A quick calculation shows that a maximum of 18 variants are possible. The goal is to calculate only those 18 variants and no more. It has been decided that these 18 variants have to be calculated in an order that can be easily written in a numerical scheme without having to alter everything when the number of variants per parameters differs, see Figure 135.

J	P1	P2	P3	P4	P5	P6	
1	P1 (1)	P2 (1)	P3 (1)	P4 (1)	P5 (1)	P6 (1)	
2	P1 (2)	P2 (1)	P3 (1)	P4 (1)	P5 (1)	P6 (1)	
3	P1 (3)	P2 (1)	P3 (1)	P4 (1)	P5 (1)	P6 (1)	(1)
4	P1 (1)	P2 (2)	P3 (1)	P4 (1)	P5 (1)	P6 (1)	
5	P1 (2)	P2 (2)	P3 (1)	P4 (1)	P5 (1)	P6 (1)	
6	P1 (3)	P2 (2)	P3 (1)	P4 (1)	P5 (1)	P6 (1)	(2)
7	P1 (1)	P2 (1)	P3 (1)	P4 (1)	P5 (2)	P6 (1)	
8	P1 (2)	P2 (1)	P3 (1)	P4 (1)	P5 (2)	P6 (1)	
9	P1 (3)	P2 (1)	P3 (1)	P4 (1)	P5 (2)	P6 (1)	
10	P1 (1)	P2 (2)	P3 (1)	P4 (1)	P5 (2)	P6 (1)	
11	P1 (2)	P2 (2)	P3 (1)	P4 (1)	P5 (2)	P6 (1)	
12	P1 (3)	P2 (2)	P3 (1)	P4 (1)	P5 (2)	P6 (1)	
13	P1 (1)	P2 (1)	P3 (1)	P4 (1)	P5 (3)	P6 (1)	
14	P1 (2)	P2 (1)	P3 (1)	P4 (1)	P5 (3)	P6 (1)	
15	P1 (3)	P2 (1)	P3 (1)	P4 (1)	P5 (3)	P6 (1)	
16	P1 (1)	P2 (2)	P3 (1)	P4 (1)	P5 (3)	P6 (1)	
17	P1 (2)	P2 (2)	P3 (1)	P4 (1)	P5 (3)	P6 (1)	
18	P1 (3)	P2 (2)	P3 (1)	P4 (1)	P5 (3)	P6 (1)	(5)

Figure 135. Visualization of the calculation order for the variants.

The green dotted lines in the figure indicate when each of the parameters with multiple variants have completed a full cycle. This is also how the scheme operates as it will only continue with the next variant of a parameter if the cycle of all the previous parameters has been completed once. After that the parameter will repeat itself in the same trend. In the example parameter 1 repeats itself after 3 loops, while the parameter 2 repeats itself after 6 loops. Equation 9.8 shows how this calculation order is created for each loop (J). It shows which column from the 'Var'-matrix should be taken when going through all the parameters (k).

$$1 + floor\left(\frac{J-1}{Mlength(k-1)}\right) - length(k) * floor\left(\frac{J-1}{Mlength(k)}\right) \qquad 9.8$$

Where,

k	=	1 : 6 (ranges from 1 to the amount of parameters)
J	=	1 : 18 (ranges from 1 to the maximum amount of variants)
floor	=	rounds down to closest integer
Mlength (k-1)	=	Multiplication of the amount of variants of all previous parameters
Mlength (k)	=	Multiplication of the amount of variants of all previous parameters including the one processed at that moment
length (k)	=	The amount of variants of the parameter that is processed at that moment

There are multiple ways to solve such a problem, however this one was found to be very efficient and gave the possibility to simply add or remove parameters from the model.

I   Equivalent Plate Thickness

For an extra comparison with the semi-analytical model and the engineering practice, a homogeneous isotropic plate with a thickness resulting in an equivalent stiffness of the gate design by Levvel, see Chapter 2, is applied. This appendix contains the calculation method to arrive at a thickness that results in an equivalent stiffness.
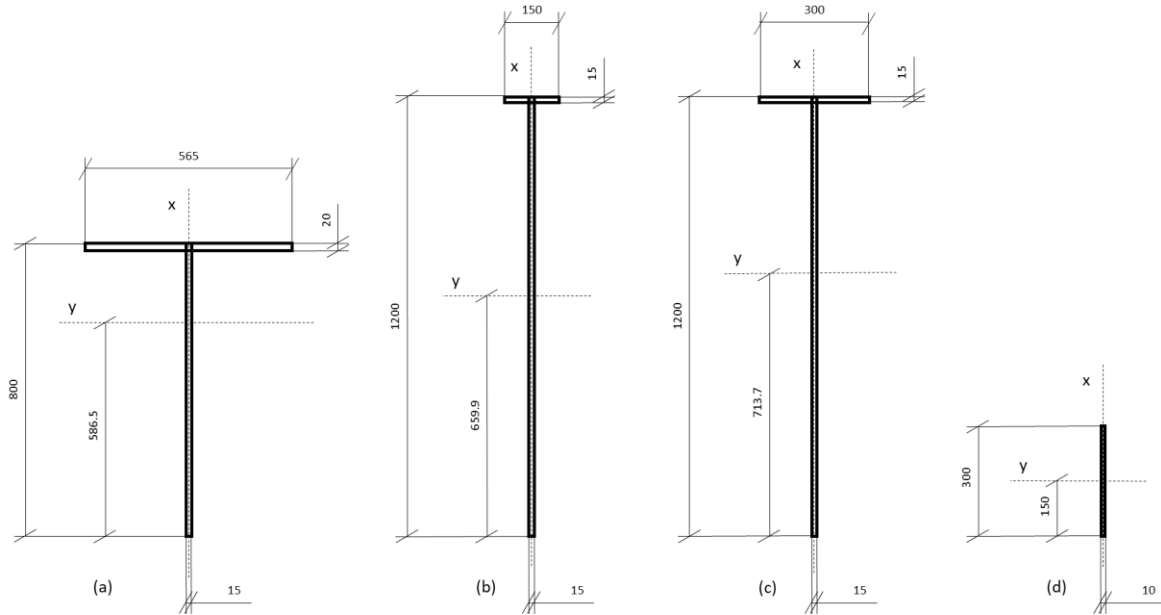
Figure 136. Vertical stiffeners of the northern gate at Den Oever. From left to right, edge (a), secondary (b), middle (c) and tertiary (d) stiffeners [mm].

The equivalent stiffness is calculated by separating the entire gate design in distinctive elements, such as the stiffeners in Figure 136 and Figure 137 and the main plate at the front. Each of these elements have their own moment of inertia (I, Equation 9.11) and center of gravity (cog, Equation 9.9).

$$cog = \frac{A_{web} \cdot \frac{h - t_{flange}}{2} + A_{flange} \cdot (h - \frac{t_{flange}}{2})}{A_{tot}} \quad [mm] \qquad 9.9$$

$$I_{steiner} = A * cog^2 \quad [mm^4] \qquad 9.10$$

$$I = \frac{1}{12} t_{web} h^3 + I_{steiner,web} + \frac{1}{12} t_{flange}^3 h + I_{steiner,flange} \quad [mm^4] \qquad 9.11$$

The results of these calculations are shown in Table 17 for the vertical stiffeners and Table 18 for the horizontal stiffeners. The same method has also been applied for the plate in both directions, which has the dimensions as shown in Chapter 2.3. The results of that calculation are shown in the last row of the for mentioned tables.

Table 17. Parameters of vertical directed elements.

Element	Area [mm^2]	I_{zz} [mm^4]	cog_z [mm]	Number in gate [-]
Edge (a)	23000	1513288406	586.5	2
Secondary (b)	20025	2799039233	659.9	2
Middle (c)	22275	3372819929	713.7	1
Tertiary (d)	3000	22500000	150.0	18
Plate	95849000	3692812	226.3	1

Combining all these elements, the center of gravity and moment of inertia can be calculated for the entire structure or gate in this case. The real calculations of these two parameters are shown in Equation 9.12 and 9.13.

$$cog_{z,total} = \frac{2 \cdot (586.5 + 15) \cdot 20250 + 2 \cdot (659.9 + 15) \cdot 20025}{2 \cdot 23000 + 2 \cdot 20025 + 22275 + 18 \cdot 3000 + 13130 \cdot 15} \cdot$$

$$\frac{20025 + (713.7 + 15) \cdot 22275 + 18 \cdot (150 + 15) \cdot 3000 + 13130 \cdot 15^2 \cdot 0.5}{2 \cdot 23000 + 2 \cdot 20025 + 22275 + 18 \cdot 3000 + 13130 \cdot 15} \qquad 9.12$$

$$= 226.3 \quad [mm]$$

$$I_{zz,total} = 2 * 1513288406 + 2 * (586.5 + 15 - 217.5)^2 * 23000$$

$$+ 2 * 2799039233 + 2 * (659.9 + 15 - 217.5)^2 * 20025$$

$$+ 3372819929 + (713.7 + 15 - 217.5)^2 * 22275 \qquad 9.13$$

$$+ 18 * 22500000 + 18 * (150 + 15 - 217.5)^2 * 3000$$

$$+ 3692812 + (217.5 + 15 * 0.5)^2 * 7300 * 15 = 42197074216 \ [mm^4]$$
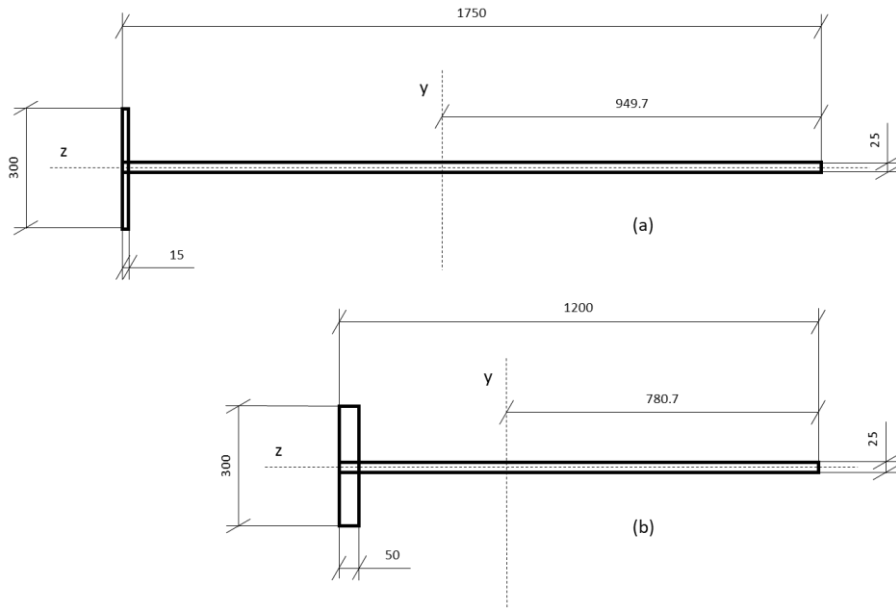
Figure 137. Horizontal stiffeners of the northern gate at Den Oever. Top stiffener (a), middle and bottom stiffener (b) [mm].

The same calculations made for the vertical stiffeners and direction has been done for the horizontal stiffeners and direction. Equations 9.14 and 9.15 show the fitting calculations.

$$cog_{x,total} = \frac{(949.7 + 15) \cdot 47875 + 3 \cdot (780.7 + 15) \cdot 43750}{47875 + 3 \cdot 43750 + 7300 \cdot 15} \cdot$$

$$\frac{7300 \cdot 15^2 \cdot 0.5}{47875 + 3 \cdot 43750 + 7300 \cdot 15} = 388.6 \quad [mm]$$

9.14

$$I_{xx,total} = 14002264606 + (949.7 + 15 - 524.7)^2 * 47875$$

$$+3 * 67207186012 + 3 * (780.7 + 15 - 524.7)^2 * 43750$$

$$+ 2053125 + (524.7 + 15 * 0.5)^2 * 13130 * 15 = 82366331805 \, [mm^4]$$

9.15

Table 18. Parameters of horizontal directed elements.

Element	Area [mm^2]	I_{xx} [mm^4]	cog_x [mm]	Number in gate [-]
Top (a)	47875	14002264606	949.7	1
Middle & bottom (b)	43750	6720186012	780.7	3
Plate	95849000	2053125	524.7	1

Finally, the equivalent moment of inertia can be reformulated to find the equivalent thickness of a homogeneous isotropic plate that has the same stiffness in a similar direction, see Equation 9.16.

$$t_{equivalent,z} = (I_{zz} \cdot 12)^{1/3} = 0.797 \quad [mm]$$

9.16

J   Guideline for Model Setup

This Appendix will contain a guideline that shows the necessities and what needs to be assembled to make sure the model will always function. The guideline is composed of two parts; first the system to analyze an existing or designed structure; Secondly the setup required for the parametric model with the machine learning optimization scheme. Figure 138 shows a flow chart of the files that need to be accessed in order. The flow chart is built up from three sections, where the information goes from Matlab to SCIA and back while being assisted by files linking the two software. This guideline will briefly show what each part provides in order of the flow chart.
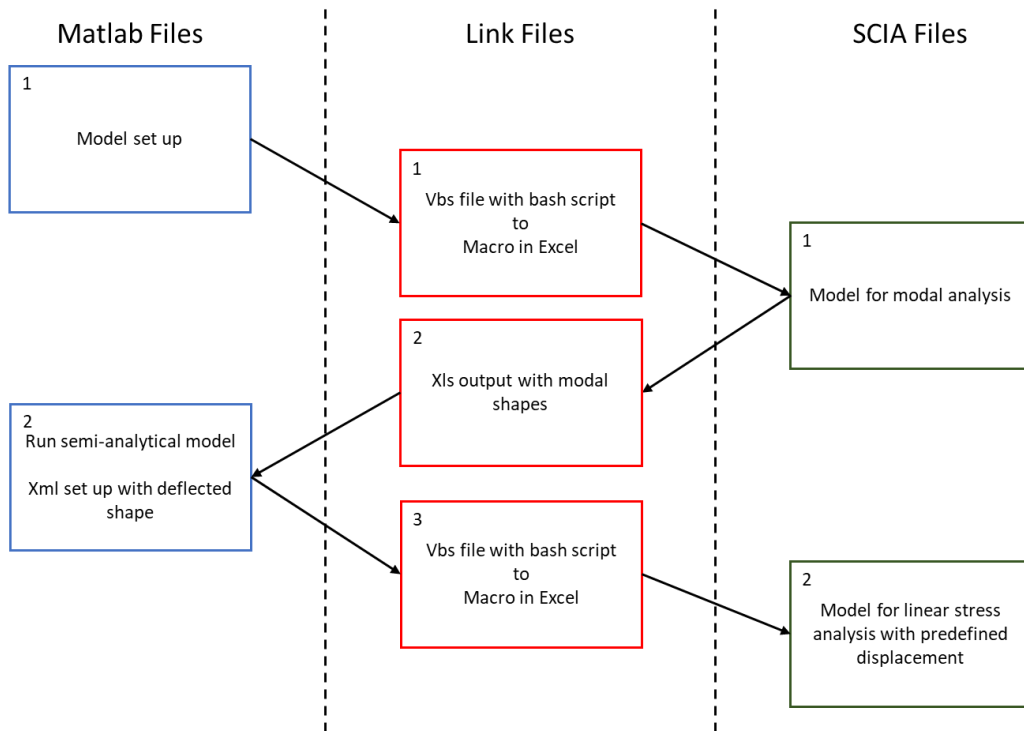
Figure 138. Model flow for the analysis of an existing structure.

Matlab (1)

This part requires the user to give information to set up the semi-analytical model These are things like the amount of fluid and structural modes or the grid size for the calculation. More importantly how much damping and if compressibility and surface waves are enabled. Then Matlab needs to access a bash script through the command prompt.

Link (1)

This link consists of two parts. First the bash script is accessed by Matlab, which can force a macro in Excel to execute its module. This module contains the link to SCIA, which can open the correct file and run a modal analysis without SCIA to open on the screen.

SCIA (1)

This file needs to be correctly saved before starting the entire model. In the last save the correct analysis needs to select, also the xml output needs to be filled with the eigenfrequencies and the deformed structure of every mode that the user wants to analyze (16 for the case of this thesis). Finally, the grid size of the mesh needs to select before saving and running the model as these settings cannot be accessed from the outside.

Link (2)

The module in Excel from Link (1) operates SCIA and when finished creates an output xls file containing the information left in the xml output last saved in the SCIA model. This should contain x-, y-, z-coordinates of the modal shapes and their corresponding eigenfrequencies.

Matlab (2)

Accessing the xls file with the data of the modal shapes and eigenfrequencies allows for the implementation of these modes into the semi-analytical model. This model as explained in the thesis calculates the dynamic response in the frequency domain of the structure coupled with the surrounding fluid by modal analysis. The output of this model is a deflected shape. This is the deflected shape with the maximum displacement in time, which is found after performing an inverse Fourier transform. This shape is then discretized to fit a predefined grid in order to calculate the stress. This discretized shape is translated to a xml file.

Link (3)

As in the first link, a bash script is accessed through the command prompt and will force a different module in the same Excel file. This module opens a slightly different SCIA model and also uses the recently created xml file as input for this model. The module will then force a linear analysis to calculate the stresses in the entire structure.

SCIA (2)

This model is basically the same as the first that was set up for modal analysis, except that this model is layered with a predefined grid equal to that created in Matlab of the deflected shape. This grid contains supports that allow for insertion of a predefined displacement. These predefined displacements are made parametric enabling the xml file to redefine these parameters. At last an updated version of the model will be produced to access the data that is produced by the analysis.

Matlab Files | Link Files | SCIA Files

1
Model set up

Xml set up for gate design

1
Vbs file with bash script
to
Macro in Excel

1
Model for modal analysis

2
Xls output with modal shapes

2
Run semi-analytical model

Xml set up with deflected shape

3
Vbs file with bash script
to
Macro in Excel

2
Model for linear stress analysis with predefined displacement

4
Xls output with stress values

3 Run post-analysis with stress output

Execute sorting and redefine the brains

Figure 139. Model flow for the analysis of the parametric model including the optimization scheme based on AI.

The parametric model operates pretty similar as can be seen in Figure 139. Only two extra parts are added to perform the post analysis automatically in Matlab and set up the system again for the next iteration. Also, the first section of the flow chart also requires a parametric model in SCIA as well as the stress model already did. This is needed to redesign the structure in every iteration and requires to setup an xml containing the information of that specific design.

It is possible for the user to implement different software, as long as each section, as shown in this guideline, is acquired. This also applies if the user wants to use the links for different functions.